

DSpace7 Instance

Salt-induced diffusiophoresis of a non-ionic micelle in water

Item Type	Text
Authors	Barrios, Eliandreina Cruz
Download date	2025-02-12 00:48:02
Link to Item	https://repository.tcu.edu/handle/116099117/56666

SALT-INDUCED DIFFUSIOPHORESIS
OF A NON-IONIC MICELLE IN WATER

By

ELIANDREINA CRUZ BARRIOS

Bachelor of Science, 2008
University of Carabobo
Valencia, Venezuela

Master of Science, 2014
Venezuelan Institute of Scientific Research
Altos de Pipe, Venezuela

Submitted to the Graduate Faculty of the
College of Science and Engineering
Texas Christian University
In partial fulfillment of the requirements
For the degree of

Doctor of Philosophy

December 2022

SALT-INDUCED DIFFUSIOPHORESIS OF A NON-IONIC MICELLE IN WATER

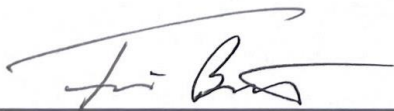
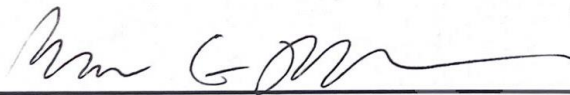
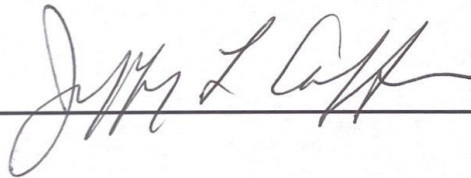
by

Eliandreina Cruz Barrios

Dissertation Approved



Major Professor



For the College of Science and Engineering

Author's Declaration

This is an original work, except where references have been made. No part of this work has been previously submitted as part of a requirement for an academic degree.

Part of this dissertation appeared in the following publications:

- (1) Cruz Barrios, E.; Annunziata, O., Determination of critical micelle concentration from the diffusion-driven dilution of micellar aqueous mixtures. *Langmuir* **2021**, *37* (8), 2855-2862.10.1021/acs.langmuir.1c00176.
- (2) Cruz Barrios, E.; Krause, T. C.; Annunziata, O., Salt-induced diffusiophoresis of a nonionic micelle: Roles of salting out and proximity to surfactant cloud point. *J. Mol. Liq.* **2022**, *359*, 10.1016/j.molliq.2022.119271.
- (3) Cruz Barrios, E.; Penino, K.V.; Annunziata, O. Diffusiophoresis of a Nonionic Micelle in Salt Gradients; Roles of Preferential Hydration and Salt-Induced Surfactant Aggregation. *Int. J. Mol. Sci.* **2022**, *23*, 13710. <https://doi.org/10.3390/ijms232213710>

ACKNOWLEDGEMENTS

I would like to acknowledge and to thank all the people that directly or indirectly contributed to my Ph.D. dissertation.

I would like to express my deepest gratitude to my research advisor, Dr. Onofrio Annunziata for his infinite patience and dedication to mentor me during this 5.5 years journey, always inspiring me to do better with kind and inspiring vocation for science and teaching.

I want to thank the members of my committee: Dr. Jeff Coffey, Dr. Benjamin Janesko, and Dr. Sergei Dzyuba for all their support, encouragement, and invaluable time they have given me during these past five years.

I also want to thank TCU for the financial support but more importantly for opening the door for me as an international student. To all the members of the Chemistry and Biochemistry Department for always being willing to help with kindness and respect.

To all my friends inside and outside of TCU for all the support and encouragement and for having each other's backs. Specially, I want to thank Dana, Maggy, David, Esther, Steven, Arlene, Julieta, Sinjo, Andrea, Leo, Marlius, and Karen.

Finally, I want to thank my family in Venezuela for always giving me words of encouragement and tell me how proud you are of me. A special thank you to my cousins Gigi and Rebeca for each Birthday, Christmas, and fun times we had together in this last 5 years and more to come.

TABLE OF CONTENT

Acknowledgments.....	ii
List of Figures.....	vii
List of Tables.....	xii
List of Symbols.....	xiii
CHAPTER 1: MOTIVATION.....	1
CHAPTER 2: SURFACTANTS.....	5
2.1 Micellization of Surfactants.....	5
2.2 Thermodynamics of Micellization.....	7
2.3 Critical Micelle Concentration.....	11
2.4 Diffusion-Driven Dilution of Micellar Aqueous Solutions.....	13
CHAPTER 3: MATERIALS AND METHODS.....	19
3.1 Materials.....	19
3.2 Solution Preparation.....	19
3.3 Density Measurements.....	20
3.4 Boundary Spreading Experiments.....	20
CHAPTER 4: RESULTS AND DISCUSSION.....	25
4.1 Boundary Spreading Characterization.....	25

4.2 Modified Pseudo-Phase Separation Model.....	26
4.3 Effect of Salt on Critical Micelle Concentration.....	30
CHAPTER 5: CONCLUSIONS.....	33
CHAPTER 6: THERMODYNAMIC THEORY BACKGROUND.....	35
6.1 Ternary of Particle(P)-Salt(S)-Water(W) Systems.....	35
6.2 Two-Domain Model.....	44
6.3 Spinodal Condition for Colloidal Solutions.....	47
CHAPTER 7: DIFFUSION THEORY IN BINARY SYSTEMS BACKGROUND.....	50
7.1 Brownian Motion.....	50
7.2 Reference Frames.....	54
CHAPTER 8: DIFFUSION AND DIFFUSIOPHORESIS IN TERNARY SYSTEMS BACKGROUND.....	57
8.1 Fick's First Law in Ternary Systems.....	57
8.2 Non-equilibrium Thermodynamics.....	59
8.3 Diffusiophoresis and Salt Osmotic Diffusion.....	61
8.3.1 Diffusiophoresis Coefficient, \hat{D}_{ps}	61
8.3.1 Osmotic diffusion Coefficient, \hat{D}_{sp}	64
8.4 Preferential Hydration Model for Diffusiophoresis.....	68

8.5 Spinodal Condition and Diffusion.....	72
CHAPTER 9: DIFFUSIOPHORESIS INTRODUCTION.....	75
CHAPTER 10: MATERIAL AND METHODS.....	81
10.1 Materials.....	81
10.2 Solution Preparation.....	81
10.3 Dynamic Light Scattering.....	82
10.4 Rayleigh Interferometry.....	82
10.5 Cloud Points Measurements.....	84
CHAPTER 11: RESULTS AND DISCUSSION.....	85
11.1 Isothermal Phase Diagram.....	85
11.2 Effect of Na ₂ SO ₄ Concentration on Micelle Diffusion Coefficients and Hydrodynamic Radius.....	87
11.3 Effect of MgSO ₄ Concentration on Micelle Diffusion Coefficients and Hydrodynamic Radius.....	89
11.4 Ternary Diffusion Coefficients.....	90
11.5 Theoretical Examination of Micelle Diffusiophoresis and Salt Osmotic Diffusion Coefficient for Micellar Aqueous Solutions.....	94
11.6 Effect of Na ₂ SO ₄ and MgSO ₄ on Micelle Diffusiophoresis and Salt Osmotic Diffusion Coefficient.....	99

11.6.1	Micelle Diffusiophoresis at Low Salt Concentration.....	101
11.6.2	Diffusiophoresis and Salt Osmotic Diffusion near Surfactant Cloud Point....	104
11.7	Effect of Salt-Induced Surfactant Aggregation in Micelle Diffusiophoresis.....	107
11.7.1	Aggregation Model.....	110
11.7.2	Effect of Aggregation on Particle Hydrodynamic Radius and Diffusiophoresis.....	113
11.7.3	Application of Aggregation Model to the Experimental Hydrodynamic Radius.....	118
11.8	Significance of Micelle Diffusiophoresis.....	120
CHAPTER 12: CONCLUSIONS.....		125
References.....		126
Appendix.....		147
Vita		
Abstract		

LIST OF FIGURES

Figure 1. Colloidal particle (yellow) in a salt concentration gradient (orange background). Black arrow indicates the migration of the particle due to diffusiophoresis from high to low salt concentration.	1
Figure 2. Example of PEGylated particle (left) and PEG-based non-ionic micelle (right).	2
Figure 3. Chemical structure of tyloxapol.	2
Figure 4. Surfactant unimer and classification by the hydrophilic group.	5
Figure 5. Most common surfactants aggregate structures.	6
Figure 6. Surfactant micellization equilibrium (mass-action model, see Section 2.2). Left: surfactant (tenside) unimer (T). Right: Spherical micelle (M).	6
Figure 7. Types of surfactant aggregates forming in solution.	7
Figure 8. Behavior of several physical properties as a function of surfactant concentration at constant temperature.	11
Figure 9. Diffusion-driven dilution of micellar aqueous solution. (A) Initial boundary, top (pure water) and bottom (micelle) solutions, at $t = 0$. (B) Boundary spreading, micelle dissociation by dilution. (C) Initial $C_p(x, t)$ profile. (D) Boundary spreading $C_p(x, t)$ profile. Inset: Sharp slope change due to micelle dissociation and diffusion enhancement.	13
Figure 10. Diffusion-based boundary spreading between (a) two solutions within a Tiselius cell. (b) Concentration profile evolution, $C_p(x, t)$, as boundary spreads. (c) Interferometry pattern measured by Gosting diffusimeter.	21
Figure 11. Scheme of Gosting diffusimeter operating in Rayleigh interferometric optical mode.	22

Figure 12. Sigmoidal concentration profiles, $C_P(Y)$, are characterizing boundary spreading between a surfactant-water solution and water at 25 °C for TX-100 (A), SDS (B), and Brij-30 (C). The bottom figures show the corresponding profiles of the concentration gradient, dC_P/dY . Vertical dashed lines locate Y^* , while the corresponding horizontal dashed lines locate C^* . Solid curves are fit through the experimental data, which are discussed further below..... 25

Figure 13. Left, theoretical concentration profile, $C_P(Y)$, extracted from eq. (2.19) based on the modified model (eq (4.1); solid curve) with $D_1 / D_M = 10$ and $C^* / C_{max} = 0.25$. For comparison, the corresponding concentration profile of the basic model (eq. (2.23); dashed curve) is included. The right figure shows the corresponding profiles of the concentration gradient, dC/dY . Vertical dashed lines locate Y^* , while the corresponding horizontal dashed line locates C^* / C_{max} 28

Figure 14. The logarithm of critical micelle concentration, $\ln C^*$, as a function of ion concentration, for TX-100 at 25 °C in aqueous NaCl (circles), Na₂SO₄ (squares), and NaSCN (diamonds). Solid curves are fitting through experimental data..... 31

Figure 15. Equilibrium dialysis setup with two compartments separated by a semipermeable membrane (dashed line). Colloidal particles (green spheres) are present in the left compartment only. (A) Initial salt concentration is equal in both compartments (uniform orange color). (B) The difference in particle concentration between the two compartments leads to salt osmotic diffusion from left to right (difference in color intensity between the two compartments). .. 65

Figure 16. Schematic of spherical colloidal particle surrounded by the remaining solution: local inner domain (I), local outer domain (II), and bulk domain (left). Salt partitioning in the local domain (I) and (II) and the bulk (right)..... 69

Figure 17. (A) Electrophoretic mechanism: positively charged particle in the presence of NaCl concentration gradient. (B) Preferential hydration mechanism: neutral particle in the presence of a salt concentration gradient. 76

Figure 18. Isothermal phase diagram of tyloxapol volume fraction (ϕ_P) as a function of (A) salt concentration and (B) osmolarity, showing binodal phase boundary for $MgSO_4$ and Na_2SO_4 Cases. (C) Phase-contrast microscope image showing formation of surfactant-rich spherical microdroplets. 86

Figure 19. (A) DLS diffusion coefficient, D_P , as a function of tyloxapol volume fraction, ϕ_P , at constant sodium sulfate concentration, $C_S/M = 0$ (\circ), 0.10 (Δ), 0.20 (\diamond), 0.30 (∇), 0.45 (\square), 0.60 (\times), 0.65 (+) at 25 °C. Solid lines are linear fits through the data. (B) Micelle hydrodynamic radius, R_P (\circ), and slope, K (\square), as a function of salt concentration. Curves are eye guides. 88

Figure 20. (A) DLS diffusion coefficient, D_P , as a function of tyloxapol volume fraction, ϕ_P , at constant magnesium sulfate concentration at 25 °C. Solid lines are linear fits through the data. (B) Micelle hydrodynamic radius, R_P (\circ), and slope, K (\square), as a function of salt concentration. Curves are eye guides. 89

Figure 21. The main-term diffusion coefficient, D_{PP} (\square), describing micelle diffusion due to its concentration gradient, and lower eigenvalue of the diffusion-coefficient matrix, D_P (\bullet), as a function of sodium sulfate concentration, C_S . A solid line is a linear fit through D_P data at $C_S = 0.30$ M and higher salt concentrations. 94

Figure 22. Micelle diffusio-phoresis coefficient, D_{PS} (\bullet), and salt osmotic diffusion coefficient, D_{SP} (\blacksquare), as a function of Na_2SO_4 concentration, C_S . Solid lines are linear fits through the data with zero intercept. 101

Figure 23. Micelle diffusiophoresis coefficient, D_{PS} (●, solid curve) as a function of sodium sulfate concentration, C_S . Values of D_{PS} (○, dashed curve) calculated using the same micelle mobility, $D_P^0(0)$, instead of $D_P(C_S)$ for all salt concentrations are included. Curves are fit through the experimental data..... 105

Figure 24. Salt osmotic diffusion, D_{SP} (■, solid curve) as a function of sodium sulfate concentration, C_S . For comparison, values of C_{SP} (□, dashed curve) were calculated using eq. (11.24) are included. Solid curves fit through the data..... 106

Figure 25. Micelle diffusiophoresis coefficient, D_{PS} (●), salt osmotic diffusion coefficient, D_{SP} (■), and preferential-interaction coefficient, C_{SP} (□) as a function of magnesium sulfate concentration, C_S . Curves associated with D_{MS} (solid curve), D_{SM} (solid line) and C_{SM} (dashed line) are fits through the data. 107

Figure 26. Spherical micelle (M) and worm-like aggregate (A)..... 108

Figure 27. Aqueous surfactant solution at a low salt concentration (left side) in contact with a solution at a high salt concentration (right side). The salt gradient is portrayed as a color contrast for simplicity. Both solutions share the same surfactant concentration and the aggregate (elongated particle) on the right side corresponds to the mass of three micelles. The number of micelles on the left side is higher than that on the right side due to the aggregate formation..... 109

Figure 28. Normalized hydrodynamic radius, R_P/R_P^0 , as a function of salt concentration, C_S , with R_P^0 being R_P at $C_S = 0$ (Na_2SO_4 , ●; MgSO_4 , ■). Curves are fit through the data based on Eqs. (11.57) and (11.58). Employed values of a are appended to each curve. 119

Figure 29. Reduced diffusiophoresis coefficients, D_{PS} , as a function of salt concentration, C_S , (Na_2SO_4 , solid curves; MgSO_4 , dashed curves). Employed values of a are appended to each curve..... 120

Figure 30. (A) The schematic diagram for examining particle diffusiophoresis in steady-state conditions. A tube of length l containing a micellar solution is connected to two salt reservoirs with salt concentrations $C_S=0$ and $C_S=C_S^{(\text{max})}=0.65$ M. The dashed line with a positive slope describes the salt concentration profile, $C_S= C_S^{(\text{max})}\cdot(x/l)$. Vertical dashed lines at the tube extremities denote two membranes not permeable to micelles. **(B)** Logarithmic diagram showing particle concentration profile (C_P/C_P^0 , solid curve) as a function of position (x/l) inside the tube calculated using the $w(C_S)$ function reported in the text. The dashed horizontal line corresponds to $w=0$ 122

LIST OF TABLES

Table 1. Values of C^* of surfactant-water solutions at 25 °C	30
Table 2. Values of C^* of Triton-X100-salt-water solutions at 25 °C.....	32
Table 3. Na ₂ SO ₄ ternary diffusion coefficients, D_{ij} , in the volume-fixed reference frame at 25 °C and tyloxapol molar concentration of $C_P=1.00$ mM.....	91
Table 4. Ternary Diffusion Coefficients, D_{ij} , in the volume-fixed reference frame at 25 °C for the tyloxapol-MgSO ₄ -water system and tyloxapol molar concentration of $C_P=1.00$ mM.	91
Table 5. Thermodynamic and transport parameters related to micelle diffusiophoresis and Na ₂ SO ₄	100
Table 6. Thermodynamic and transport parameters related to micelle diffusiophoresis and MgSO ₄	100
Table 7. Parameters extracted by applying the method least squares based on eq. (8.142).	119

LIST OF SYMBOLS

C^*	Critical Micelle Concentration
C_P^*	Critical surfactant concentration for aggregates
C_P^{0*}	Critical surfactant concentration for aggregates without salt
C^0	standard concentration
C_P	Total Concentration of Surfactant
C_1	Concentrations of surfactant unimers
C_2	Concentrations of surfactant dimers
C_M	Micelle concentration
C_S	Salt Concentration
C_S^*	Critical salt concentration
C_A	Aggregate concentration
C_{SP}	Thermodynamic coefficient
C_{max}	Maximum surfactant concentration
ϕ_P	Particle volume fraction
ν_S	Number of salt ions
γ_S	Salt thermodynamic factor
γ_P	Particle thermodynamic factor
m_s	Salt molality
m_p	Particle composition
m_s	Salt composition
m	Surfactant aggregation number
\tilde{m}	Apparent micelle aggregation number
β	Formation constant
K_d	Dissociation constant
K	Micelle-micelle interaction parameter

K^*	Partition coefficient
$K^{(I)}$	Inner local domain partitioning coefficient
$K^{(II)}$	Outer local domain partitioning coefficient
K'_S	Salting out constant
K_S	$(a-1)K'_S$
$C_p(x, t)$	Particle concentration profile
x	Position perpendicular to boundary
t	Time
k_B	Boltzmann constant
T	Temperature
p	Pressure
Π	Osmotic pressure
η	Viscosity
d	Density
G	Gibbs free energy
n_p	Moles of colloidal particle
n_s	Moles of salt
n'_S	Number of salt ions in the local domain
n^*_S	Number of salt ions in the bulk domain
$n^{(I)}_S$	Inner local domain number of salt ions
$n^{(II)}_S$	Outer local domain number of salt ions
n_w	Moles of Water
n'_w	Number of water molecules in the local domain
n^*_w	Number of water molecules in the bulk domain
$n^{(I)}_w$	Inner local domain number of water molecules
$n^{(II)}_w$	Outer local domain of water molecules
N_w	Water thermodynamic excess

$N_{\text{W}}^{(1)}$	Excess of water in inner local domain
$N_{\text{W}}^{(1)}$	Excess of water in outer local domain
$N_{\text{W}}^{(M)}$	Water excesses in the micellar state
$N_{\text{W}}^{(A)}$	Water excesses in the aggregate state
μ_{P}	Particle chemical potential
m_{P}^0	Particle chemical potential in the standard state
μ_{S}	Salt chemical potential
μ_{W}	Water chemical potential
μ_{SS}	Salt chemical potential change with salt concentration
μ_{PP}	Particle chemical potential change with particle concentration
μ_{SP}	Salt chemical potential change with particle concentration
μ_{PS}	Particle chemical potential change with salt concentration
V	Total volume
\bar{V}_{P}	Particle molar volume
\tilde{V}_{P}	Particle apparent molar volume
\bar{V}_{S}	Salt molar volume
\bar{V}_{W}	Water molar volume
f_{P}	Particle activity coefficient
f_{S}	Salt activity coefficient
R	Ideal gas constant
D_{P}^0	Particle tracer diffusion coefficient
D_{P}	Particle mutual diffusion coefficient
D_{S}	Salt mutual diffusion coefficient
D_{W}	Water mutual diffusion coefficient
D_1	Surfactant unimer mutual diffusion coefficient

D_M	Micelle diffusion mutual coefficient
D_A	Aggregate diffusion mutual coefficient
D_{PP}	Particle diffusion coefficient due to its own solute concentration gradient.
D_{SS}	Salt diffusion coefficient due to its own solute concentration gradient.
D_{PS}	Particle diffusion coefficient due to salt concentration gradient.
D_{SP}	Salt diffusion coefficient due to particle concentration gradient.
\hat{D}_{PS}	Diffusiophoresis coefficient
\hat{D}_{SP}	Salt osmotic diffusion coefficient t
\tilde{D}_P	Particle lower eigenvalue of the diffusion coefficient matrix
\tilde{D}_S	Salt lower eigenvalue of the diffusion coefficient matrix
L_{PP}	Particle Onsager transport coefficient due to its own solute concentration gradient.
L_{SS}	Salt Onsager transport coefficient due to its own solute concentration gradient.
L_{PS}	Particle Onsager transport coefficient due to salt concentration gradient.
L_{SP}	Salt Onsager transport coefficient due to particle concentration gradient.
X_A	Fraction of aggregates
$H(z)$	Heaviside step function
$\text{erf}(z)$	Error function
y	Reduced position
y^*	Reduced position at $C = C^*$
Y	Experimentally accessible position
y_c	value of y at $C = C_{\max}/2$
J	Molar flux
J_P	Particle molar flux
J_S	Salt molar flux
J_W	Water molar flux
J_A	Aggregate molar flux

J_A	Micelle molar flux
A	Area
\mathcal{J}	Fringes
j	Fringe shift
$\langle \bar{r} \rangle$	Mean Brownian displacement
f	Frictional drag coefficient
\bar{F}_d	Driving force
\bar{F}_f	Frictional force
\bar{v}_p	Particle drift velocity
\bar{v}_w	Water drift velocity
R_p	Particle hydrodynamic radius
R_M	Micelle radius
R_A	Aggregate radius
α	Particle to salt diffusion ratio
α_a	Aggregate-to-micelle mobility ratio
λ	Transport parameter
γ	Thermodynamic parameter
a	Aggregate-to-micelle aggregation number ratio
φ	Perrin shape factor

CHAPTER 1

1.1 Motivation

Diffusiophoresis is the isothermal migration of colloidal particles in aqueous media induced by cosolutes concentration gradients such as salts (see Figure 1).¹⁻⁷ This transport mechanism has attracted much attention since controlling the motion of colloidal particles in liquids is important for many applications including microfluidics,⁸⁻¹² separation and purification techniques,¹²⁻¹⁵ coating industry,^{16, 17} enhanced oil recovery,¹⁸⁻²¹ drug delivery,^{22, 23} and detergency.^{24, 25}

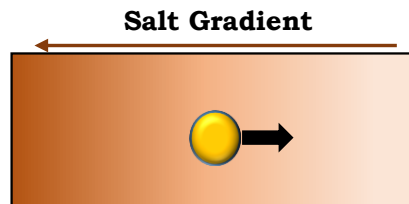


Figure 1. Colloidal particle (yellow) in a salt concentration gradient (orange background). Black arrow indicates the migration of the particle due to diffusiophoresis from high to low salt concentration.

Experimental studies regarding diffusiophoresis of charged particles are widely reported in recent literature but there is no experimental investigation on colloidal particles that are electrically neutral. An important class of water-soluble colloidal particles is represented by hydrophilic neutral particles whose interfacial properties are modified or governed by polyethylene glycol (PEG). PEG is a neutral water-soluble polymer that has been employed for coating the surface of inorganic nanoparticles,^{26, 27} proteins,²⁸ micelles,²⁹ and vesicles^{30, 31} (see Figure 2 *left*). Due to the low toxicity of this synthetic polymer, PEG-based nanoparticles are extensively used in industrial and pharmaceutical applications. Thus, it is important to determine and understand the mechanism of salt-induced diffusiophoresis for this

type of colloidal particle. We are particularly interested in the diffusiophoresis of non-ionic micelles formed by tyloxapol as a model PEG-based globular colloidal particle (see Figure 2 *right*) in the presence of gradients of salts with salting-out properties at room temperature.

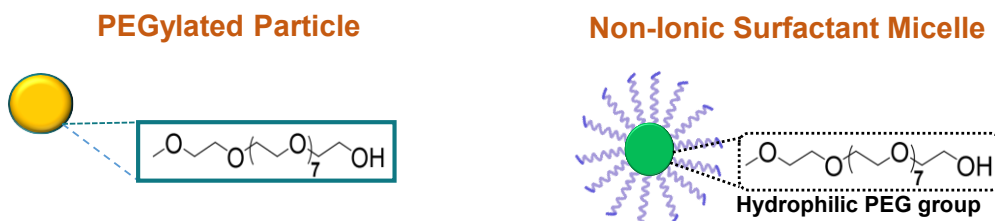


Figure 2. Example of PEGylated particle (left) and PEG-based non-ionic micelle (*right*).

Tyloxapol (see Figure 3) is a commercially available nonionic surfactant that was chosen in this investigation because it has the advantage of a very low critical micelle concentration ($C^* = 0.0358 \text{ g L}^{-1}$) and low polydispersity. Hence, it forms thermodynamically stable spherical micelles with a negligible amount of free surfactant in aqueous solutions.

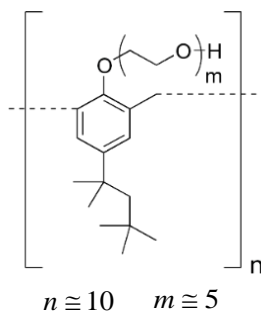


Figure 3. Chemical structure of tyloxapol.

In general, micelle diffusiophoresis is important because these colloidal particles can host nonpolar molecules. Hence, understanding micelle diffusiophoresis is also important for manipulating the motion of small guest molecules, relevant to detergency,²⁹ extraction,³² catalysis,³³ and applications as carriers for the delivery of therapeutic agents.³⁴ Furthermore, controlling the motion of micelles by salt-induced diffusiophoresis would be also valuable for

enhancing micelle insertion into dead-end pores, with applications in the extraction of hydrocarbons from porous rocks^{10, 21} relevant to enhanced oil recovery¹⁹ and soil remediation.³²

Sodium and magnesium sulfates were chosen as salts with salting-out properties.³⁵ In general, sulfate salts are known to significantly affect thermodynamic and transport properties of aqueous PEG solutions.⁶ Thus, we hypothesize that these cosolutes can also produce diffusiophoresis of PEG-based colloidal particles in water.

This dissertation is outlined in the following way:

In Chapter 2 we provide an introduction on surfactants and their aqueous solutions. Chapters 3 to 5 focus on our experimental investigation on micelle thermodynamic stability and the effect of salts on the thermodynamic stability of micelles. It is well-known that micellization occurs above a well-defined surfactant concentration known as critical micelle concentration, (cmc or C^*). However, the value of cmc may depend on cosolute concentration and type. In our case, it is important to assess how salts affect the cmc of non-ionic surfactants. Hence, we introduce a novel method for cmc determination that was successfully used to determine the effect of salts on surfactant cmc. In general, we also need to determine the range of experimental conditions in which micelles are thermodynamically stable and diffusiophoresis measurements can be performed. Thus, for completeness, it is important to note that salts, at high concentrations, may also affect thermodynamic stability of aqueous surfactant solutions leading to phase separation (cloud point). Our cloud points experimental results at 25 °C will be given in Chapter 11.

Chapters 6 to 8 provide the theoretical background on isothermal diffusion in multicomponent liquid systems based on non-equilibrium thermodynamics, diffusiophoresis, and their relationship to thermodynamic properties. We also introduce the concept of salt osmotic diffusion and how this is important to explain the diffusiophoresis results, based on the preferential hydration of PEG. Related equations will be used to describe and theoretically examine the experimental results reported in Chapter 11.

Chapters 9 to 12 focus on the experimental investigation of diffusiophoresis of tyloxapol micelles in the presence of sodium and magnesium sulfate at 25 °C. These experimental results are theoretically examined using non-equilibrium thermodynamics and a preferential-hydration model. Additionally, since sulfate salts were also found to enhance surfactant self-assembly in water, the role of salt-induced aggregation on micelle diffusiophoresis was also theoretically examined using a two-state aggregation model. Finally, a mass-transfer model was employed to evaluate micelle diffusiophoresis in the presence of steady-state salt concentration gradient.

CHAPTER 2

SURFACTANTS

2.1 Micellization of Surfactants

Surfactants or tensides, are amphiphilic organic molecules with a hydrophobic chain covalently linked to a hydrophilic group. The chemical nature of the hydrophilic group is commonly used to classify surfactants as ionic, non-ionic, or amphoteric (see Figure 4).³⁶ Surfactants are widely used in applications that include drug solubilization,³⁷ drug delivery,³⁸ enhanced oil recovery,^{39, 40} detergency,⁴¹ catalysis,⁴² soil remediation,⁴³ and protein crystallization and purification.⁴⁴

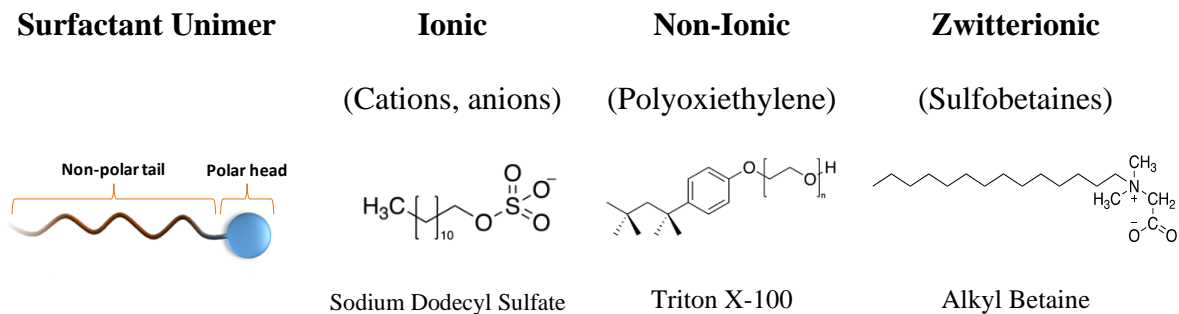


Figure 4. Surfactant unimer and classification by the hydrophilic group.

In an aqueous solution, and above a specific concentration known as critical micelle concentration (cmc or C^*), surfactants unimers form aggregates. These aggregates are considered self-assembled colloids and are subdivided into several subgroups such as micelles, vesicles, and bilayer membranes (see Figure 5). Each subgroup plays an important role in many

aspects of colloid and surface science, both as model probes that help us to understand the basic principles of molecular interactions and in the practical applications of those principles.⁴⁵

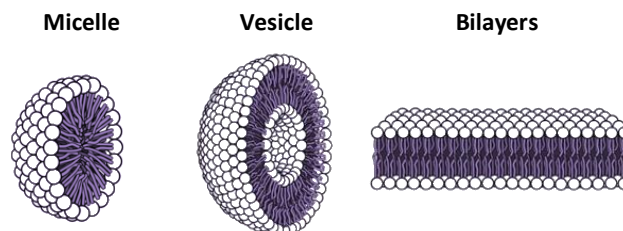


Figure 5. Most common surfactants aggregate structures.⁴⁵

In this work, we are particularly interested in *micelles* in aqueous solutions. Micelles are in a dynamic equilibrium with the surfactant unimers in the bulk solution. The average number of unimers within a micelle is known as the *aggregation number*. Micellization in water is a consequence of *the hydrophobic effect*.⁴⁶ This produces globular nanoaggregates with the nonpolar hydrophobic chains forming the core of the micelle and the hydrophilic groups positioned at the micelle-water interface, thereby optimizing micelle interaction with its surrounding aqueous fluid (see Figure 6).

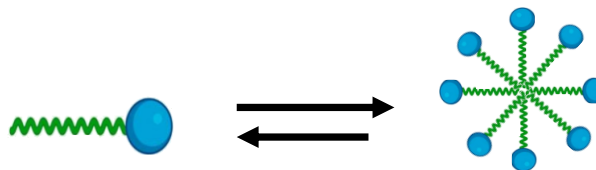


Figure 6. Surfactant micellization equilibrium (mass-action model, see Section 2.2). Left: surfactant (tenside) unimer (T). Right: Spherical micelle (M).

In concentrated micellar solutions, micelle-micelle interactions lead to structures with higher aggregation numbers. Correspondingly, the geometric shape of surfactant aggregates changes from spherical to rod-like (worm-like) to lamellar (see Figure 7). The thermodynamic stability of structures with higher aggregation numbers also depends on temperature and solution ionic strength.^{47, 48}

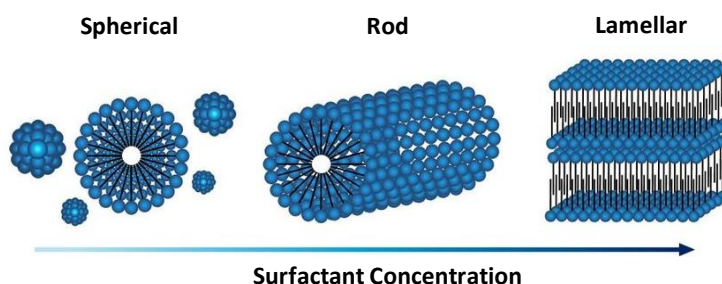


Figure 7. Types of surfactant aggregates forming in solution.⁴⁸

2.2 Thermodynamics of Micellization

Micelle formation is typically described by two primary models that allow us to understand the energetics of the process of self-association or micellization. The first model is *the mass-action model* (see Figure 6), in which the micelles (M) and free surfactant (T, for tenside) are considered to be in chemical equilibrium ($m T \rightleftharpoons M$), where m is the aggregation number. The second model is the *phase separation model*, in which micelles are considered to constitute a new phase (pseudo-phase) formed in the mixture at and above the cmc (C^*). Note that cmc is a saturation concentration for the surfactant unimers and essentially represents their “solubility”.^{36, 45, 49} The phase separation model and cmc can be deduced from the mass-action model thermodynamics by considering chemical equilibrium between free unimers and

micelles. To make connection between the two models, we start by considering the simpler case for dimer formation ($m = 2$). Here, we can write:

$$\beta_2 = \frac{1}{K_d} = \frac{C_2}{(C_1)^2} \quad (2.1)$$

where C_2 and C_1 indicate the equilibrium molar concentrations of dimers and unimers, respectively, and β_2 is the dimer equilibrium formation constant and K_d is the corresponding dissociation constant with the units of concentration. We then generalize eq. (2.1) for arbitrary m :

$$\beta_m = \frac{1}{K_d^{m-1}} = \frac{C_M}{(C_1)^m} \quad (2.2)$$

where C_M is the micelle concentration and β_m is the micelle formation constant. We now show that K_d in eq. (2.2) becomes the micelle critical concentration when $m \gg 1$. This limit is relevant to micellization because m is typically large.

The total concentration of surfactant, C_p , is linked to micelle and free surfactant concentration by the mass balance:

$$C_p = C_1 + mC_M \quad (2.3)$$

If we use eq. (2.2) to substitute C_M in eq. (2.3), we can write:

$$C_p = C_1 + m\beta(C_1)^m = C_1 + m\frac{(C_1)^m}{K_d^{m-1}} \quad (2.4)$$

If we then take the first derivative of eq. (2.4) with respect to C_1 , we obtain:

$$\frac{dC_p}{dC_1} = 1 + m^2 \left(\frac{C_1}{K_d} \right)^{m-1} \quad (2.5)$$

Finally, we take the reciprocal of eq. (2.5), to write:

$$\frac{dC_1}{dC_p} = \frac{1}{1 + m^2 \left(\frac{C_1}{K_d} \right)^{m-1}} \quad (2.6)$$

Equation (2.6) is now examined in the case of $m \gg 1$. If $C_1 < K_d$, $m^2 (C_1 / K)^{m-1} \ll 1$ in the denominator. This leads to:

$$\frac{dC_1}{dC_p} = 1 \quad (2.7)$$

Integration of eq. (2.7) starting from $C_p = 0$ yields:

$$C_1 = C \quad \text{when } C_p < K_d \quad (2.8)$$

This means that all the surfactant is in the unimer form when $C_p < K_d$.

We then consider the case of $C_p > K_d$. Here, we have: $m^2 (C_1 / K_d)^{m-1} \gg 1$ in eq. (2.6). This means that:

$$\frac{dC_1}{dC_p} = 0 \quad (2.9)$$

Integration of eq. (2.9) starting from $C_p = K_d$ yields:

$$C_1 = K_d \quad \text{when } C_p > K_d \quad (2.10)$$

From eqs. (2.11) (2.10), we can appreciate that K_d is a saturation concentration, i.e., the surfactant cmc. The phase-separation model will be further discussed in section 2.3.

For the case of ionic surfactant, we have to consider the more complex equilibrium. For example, in the case of negatively charged unimers (T^-) with monovalent inorganic cations (C^+) we have: $mT^- + qC^+ \rightleftharpoons (T_mC_q)^{(m-q)-}$. Since each surfactant head is negatively charged, micellization occurs along with partial counterion adsorption, to reduce head-head electrostatic repulsion. Typically, the number of counterions adsorbed on micelle is smaller than micelle aggregation number. This implies that micelle net charge remains negative. Although the mass-action model for this case is more complex than the one previously shown for neutral surfactant, a critical micelle concentration can be deduced also in this case. However, it is important to note that the cmc of ionic surfactants is predicted to strongly decrease with salt concentration due to the common-ion effect^{36, 45}. On the other hand, the effect of salt concentration on the cmc value of non-ionic surfactants is not well understood and may strongly depend on salt type.

2.3 Critical Micelle Concentration

As previously mentioned, the minimal surfactant concentration above which micelles form is known as the cmc, here denoted as C^* . The C^* value of a surfactant plays a crucial role in characterizing and optimizing the thermodynamic stability of micelles and solubilization of drugs, substrates, or petroleum-related compounds. Thus, the experimental determination of C^* values has always been a primary goal of surfactant characterization.^{45, 47} The presence of additives such as salts typically causes a decrease in the C^* value of ionic surfactants. Historically, C^* values have been determined from the plot of a solution's physical property (surface tension, absorbance, fluorescence, turbidity, colligative properties, equivalent conductivity, self-diffusion, nuclear-magnetic, and electron paramagnetic resonance),^{29, 50-58} as a function of surfactant concentration.⁵⁹ The resulting curve normally exhibits a sharp change of slope when micelles start to form. Figure 8 illustrates several physical properties such as osmotic pressure, light scattering, surface tension, conductivity, and self-diffusion are plotted as a function of surfactant concentration.

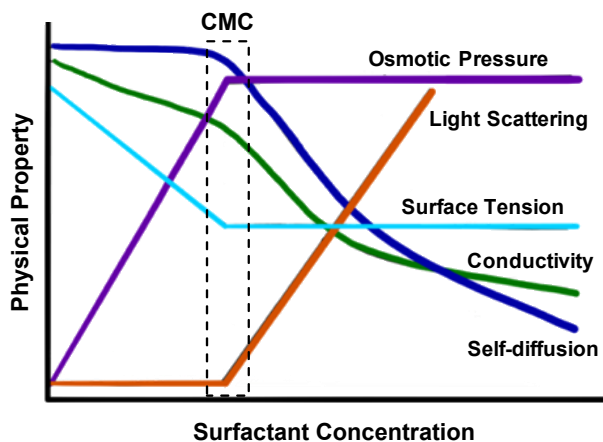


Figure 8. General behavior of several physical properties as a function of surfactant concentration (ionic/non-ionic) at constant temperature.⁶⁰

At low surfactant concentrations, most surfactant properties are similar to those of common solutes such as inorganic salts or neutral osmolytes in water. However, all surfactant properties shown in Figure 8 exhibits an abrupt change at a particular concentration that is consistent with a “phase transition”; i.e., the formation of micelles. The surfactant concentration at which a sudden change in a measured property is observed is taken as the value of C^* . These techniques usually require multiple-sample preparation (at different concentration) and analysis; some are restricted to ionic surfactants (conductivity) or involve the use of probes and/or lacked the precision needed to accurately determine the effect of cosolute concentration on C^* . Due to the limitations of individual methods and the urgency of surfactant characterizations, there is a continuous demand for the development of new methods for rapid and precise C^* determination.⁶¹⁻⁶⁷

In our case, we are interested in sulfate salts for the diffusiophoresis experiments. Thus, we want to determine how sulfate salts affect the critical micelle concentration of non-ionic surfactants with PEG functional groups. This presented an opportunity for us to develop a novel methodology that allows not only to determine C^* but also to precisely determine C^* as a function of salt concentration and surfactant type (ionic or non-ionic).

In the sections below, we demonstrate that the *diffusion-driven dilution of micelles* into solvent inside a vertical channel can be used to observe disaggregation at a well-defined vertical position.⁶⁸ Specifically, we show that the diffusion-based spreading of the boundary between a micellar aqueous solution and pure water yields a one-dimensional spatial profile of surfactant concentration that can be then used to identify the value of the C^* . This approach is

precise, noninvasive, applicable to both ionic and nonionic surfactants, and yields C^* values from single experiments without the need for multiple-sample preparation.

2.4 Diffusion-Driven Dilution of Micellar Aqueous Solution

In this section, our basic theoretical model, demonstrating why diffusion-based boundary spreading can be used to determine C^* values, is outlined. Specifically, the one-dimensional concentration profile, $C_p(x, t)$, produced by the isothermal diffusion-based spreading of the boundary between a micellar aqueous solution of concentration $C_p = C_{\max}$ (with $C_{\max} > C^*$) and water ($C_p = 0$) is theoretically examined, with x and t being the position perpendicular to boundary and time, respectively (see Figure 9).

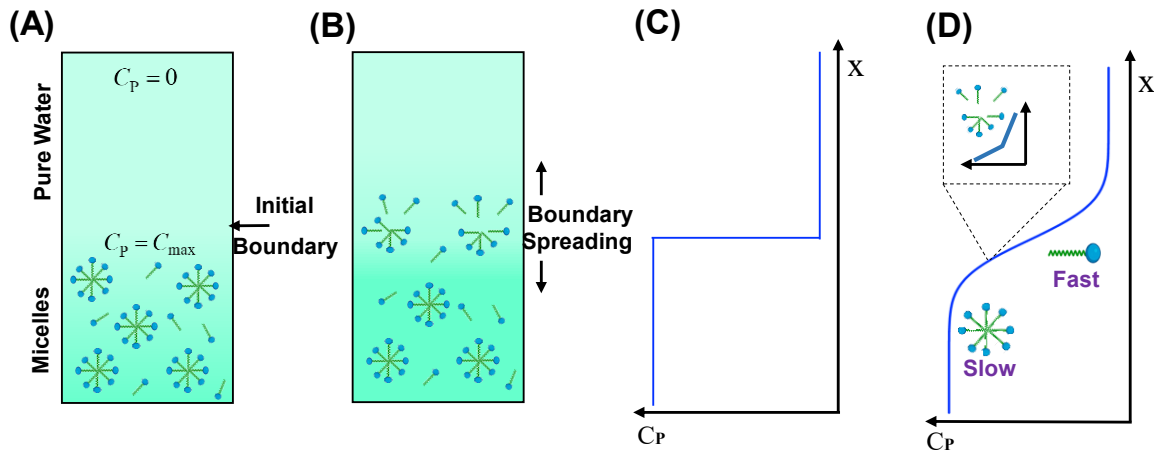


Figure 9. Diffusion-driven dilution of micellar aqueous solution. (A) Initial boundary, top (pure water) and bottom (micelle) solutions, at $t = 0$. (B) Boundary spreading, micelle dissociation by dilution. (C) Initial $C_p(x, t)$ profile. (D) Boundary spreading $C_p(x, t)$ profile. Inset: Sharp slope change due to micelle dissociation and diffusion enhancement.

To derive the theoretical expression of $C_p(x,t)$, we apply the pseudo-phase separation model (see Section 2.2) to a non-ionic surfactant. Micelle dissociation is expected to be sufficiently fast that can be assumed to instantaneously occur⁶⁹ as surfactant concentration becomes lower than C^* due to dilution.

According to Fick's first law of diffusion (see Chapter 7, Section 7.1, for more diffusion details), the mutual-diffusion coefficient, D_p , for a surfactant-water mixture, is given by:^{69, 70}

$$D_p = \left(\frac{dC_1}{dC_p} \right) D_1 + \left(\frac{dC_M}{dC_p} \right) D_M \quad (2.11)$$

where D_1 and D_M are the free surfactant (unimer) and micelle diffusion coefficients, respectively. We shall assume that these two parameters are constant and identifiable with the corresponding tracer-diffusion coefficients (See chapter 7, Section 7.1) and with D_M significantly smaller than D_1 due to the relatively large hydrodynamic radius of micelles compared to free surfactant unimers.⁷¹ Correspondingly, C_1 and C_M are the surfactant concentrations in the unimer and micellar states, with $C_p = C_1 + C_M$ being the total surfactant concentration. According to eq. (2.11), D_p is a weighted average of D_1 and D_M , with the derivatives, dC_1/dC_p and dC_M/dC_p , being the corresponding weights. These total derivatives originate from the concentration gradients of the individual species (free surfactant and micelle).

According to the pseudo-phase separation model,⁷² we have $C_M = 0$ and $C_1 = C_p$ for $C_p < C^*$, and $C_1 = C^*$ for $C_p > C^*$. Hence, eq. (2.11) can be rewritten in the following way:

$$D_p = D_1 H(C^* - C) + D_M H(C - C^*) \quad (2.12)$$

where $H(z)$ is the Heaviside step function with $H(z) = 0$ and $H(z) = 1$ when $z < 0$ and $z > 0$, respectively. Based on this description, the mutual diffusion coefficient of a surfactant-water system exhibits a jump discontinuity point at the critical micelle concentration.^{69, 70, 73} This behavior is distinct from that of the self-diffusion coefficient, $D_p = (C_1/C_p)D_1 + (C_M/C_p)D_M$,^{50, 56, 73, 74} which remains continuous at $C_p = C^*$ because it is a weighted average based on species concentrations instead of their derivatives as shown in eq. (2.11).

The concentration profiles, $C_p(x,t)$, are extracted from Fick's second law.⁷³ According to eq. (2.12) this can be written in the following way:

$$\frac{\partial C_p}{\partial t} = D_1 \frac{\partial^2 C_p}{\partial x^2} \quad (C_p < C^*) \quad (2.13)$$

$$\frac{\partial C_p}{\partial t} = D_M \frac{\partial^2 C_p}{\partial x^2} \quad (C_p > C^*) \quad (2.14)$$

The general solution of eqs. (2.13) and (2.14) is given by:⁷⁵

$$C_p = A + B \operatorname{erf}(D_1^{-1/2} y) \quad (C_p < C^*) \quad (2.15)$$

$$C_p = A' + B' \operatorname{erf}(D_M^{-1/2} y) \quad (C_p > C^*) \quad (2.16)$$

where $y \equiv (1/2)xt^{1/2}$ is the reduced position, $\operatorname{erf}(z) \equiv (2\pi^{-1/2}) \cdot \int_0^z e^{-s^2} ds$ is the error function, and A, B, A' , and B' are constants to be determined.

If we set $C_p = 0$ and $C_p = C_{\max}$ at $y = -\infty$ and $y = +\infty$, respectively (free-boundary condition^{75, 76}), we deduce that $A - B = 0$ and $A' + B' = C_{\max}$. Thus, eqs. (2.15) and (2.16) become:

$$C_p = A [1 + \operatorname{erf}(D_1^{-1/2}y)] \quad (C_p < C^*) \quad (2.17)$$

$$C_p = A' + (C_{\max} - A')\operatorname{erf}(D_M^{-1/2}y) \quad (C_p > C^*) \quad (2.18)$$

To identify A and A' , we observe that $C_p = C^*$ corresponds to a unique reduced position, y^* , attainable from both eq. (2.17) and eq. (2.18), with $y \leq y^*$ and $y \geq y^*$ corresponding to $C_p \leq C^*$ and $C_p \geq C^*$, respectively. Thus, by applying the continuity condition of $C_p = C^*$ at $y = y^*$ to eqs. (2.17) and (2.18) we obtain:

$$C_p = \left[\frac{1 + \operatorname{erf}(D_1^{-1/2}y)}{1 + \operatorname{erf}(D_1^{-1/2}y^*)} C^* \right] H(y^* - y) + \left[C_{\max} - \frac{1 - \operatorname{erf}(D_M^{-1/2}y)}{1 - \operatorname{erf}(D_M^{-1/2}y^*)} (C_{\max} - C^*) \right] H(y - y^*) \quad (2.19)$$

Note that the behavior of $C_p(y)$ described by eq. (2.19) is equivalent to that predicted for the diffusion of a solute through two different media interfaced at y^* .⁷⁵ However, the position, y^* , is typically known in this mass transfer problem, contrary to our case.

After choosing values of C^* , D_M , and D_1 , eq. (2.19) can be used to generate theoretical profiles of surfactant concentration, $C_p(y)$, provided that y^* is also known. The value of y^* can be linked to that of C^* by imposing that diffusion flux (see chapter 7, section 7.1), J , is also a continuous function at $y = y^*$ due to mass conservation:

$$J \Big|_{y \rightarrow y^{*-}} = J \Big|_{y \rightarrow y^{*+}} \quad (2.20)$$

To obtain the explicit form for eq. (2.20), the two limiting expressions of the concentration gradient, dC_P/dx at $y \rightarrow y^{*-}$ and $y \rightarrow y^{*+}$ can be deduced from eq. (2.19):

$$\left. \frac{dC_P}{dx} \right|_{y \rightarrow y^{*-}} = (\pi t)^{-1/2} \frac{D_1^{-1/2} e^{-y^{*2}/D_1}}{1 + \operatorname{erf}(D_1^{-1/2} y^*)} C^* \quad (2.21)$$

$$\left. \frac{dC_P}{dx} \right|_{y \rightarrow y^{*+}} = (\pi t)^{-1/2} \frac{D_M^{-1/2} e^{-y^{*2}/D_M}}{1 - \operatorname{erf}(D_M^{-1/2} y^*)} (C_{\max} - C^*) \quad (2.22)$$

After inserting eq. (2.21) and (2.22) into Fick's first law, $J = -D_P \cdot dC_P/dx$,⁷⁷ with $D_P = D_1$ for $y = y^{*-}$ and $D_P = D_M$ for $y = y^{*+}$, eq. (2.20) yields the following relation between C^* and y^* :

$$\frac{C^*}{C_{\max} - C^*} = \left(\frac{D_M}{D_1} \right)^{1/2} \frac{1 + \operatorname{erf}(D_1^{-1/2} y^*)}{1 - \operatorname{erf}(D_M^{-1/2} y^*)} e^{-\left(\frac{1}{D_M} - \frac{1}{D_1} \right) y^{*2}} \quad (2.23)$$

It is important to observe that values of y cannot be experimentally identified before C^* determination. Indeed, the reference position of $y = 0$ varies with respect to that fixed by an external reference frame (see Chapter 7. Section 7.2), depending on the value of C^*/C_{\max} . It is therefore convenient to introduce the experimentally accessible position, Y , with the reference value of $Y = 0$ always corresponding to the profile midpoint at $C = C_{\max}/2$. Correspondingly, we replace y with $Y + y_c$ in (2.19), with y_c being the value of y at $C = C_{\max}/2$. The value of y_c can be linked to that of y^* after substituting $C = C_{\max}/2$ in eq (2.19). If experiments are designed such that $C_{\max}/2 > C^*$, we have:

$$\operatorname{erf}(D_M^{-1/2} y_c) = 1 - \frac{1 - \operatorname{erf}(D_M^{-1/2} y^*)}{2(1 - C^*/C_{\max})} \quad (2.24)$$

In summary, eq. (2.19) shows the link between the surfactant concentration profile caused by diffusion-based boundary spreading and C^* . While $C_P(y)$ is a continuous function, this model predicts that its first derivative, dC_P/dy , displays a discontinuity point at $y = y^*$ due to the sharp change in diffusion coefficient, see eq. (2.12), at this location. In chapter 4, result section 4.2, we will show a modification of the model to fit our experimental data.

CHAPTER 3

MATERIALS AND METHODS

3.1 Materials

We determine C^* for three well-known surfactants in water at 25 °C. These surfactants are Triton X-100 (TX-100), as an example of a nonionic surfactant, sodium dodecyl sulfate (SDS), as an example of an ionic surfactant, and poly(oxyethylene) (4)-Lauryl Ether (Brij-30) to examine method sensitivity as this nonionic surfactant has a significantly low C^* value. TX-100 (647 g·mol⁻¹) and Brij-30 (362.55 g·mol⁻¹) were obtained from Sigma-Aldrich and SDS (288.37 g·mol⁻¹) was obtained from Merk. We also characterized the dependence of C^* on salt type and concentration for the case of TX-100. The salts are sodium chloride (NaCl; 58.44 g·mol⁻¹), sodium sulfate (Na₂SO₄; 142.04 g·mol⁻¹), and sodium thiocyanate (NaSCN; 81.07 g·mol⁻¹), all obtained from Merck. Sodium thiocyanate was heated in an oven at 100 °C for 7 hours and kept in a desiccator. The other materials were used as received without further purification. Deionized water was passed through a four-stage Millipore filter system to provide high-purity water (0.06μS) for all the experiments.

3.2 Solution Preparation

In the case of Na₂SO₄, a binary salt-water stock solution was prepared due to salt hygroscopicity. Its composition was determined from density measurements and the known density-composition relation:⁷⁸

$$d_{\text{Na}_2\text{SO}_4} = 0.997045 + 0.129483(m_s/m^0) - 0.0086616(m_s/m^0)^{1.5} - 0.0061207(m_s/m^0)^2 + 0.0007909(m_s/m^0)^{2.5} \quad (3.1)$$

where m_s is salt molality and $m^0 \equiv 1$ mol/kg. All other salts and surfactant solutions were prepared by weight using a Mettler-Toledo AT400 analytical balance. Molar concentrations were obtained from the density of solutions and reported molecular weights.

3.3 Density Measurements

All density measurements were made with a Mettler-Paar DMA40 density meter, thermostated with water from a large, well-regulated ($\pm 0.001^\circ\text{C}$), water bath. The densitometer has a vibrating tube with the temperature controlled by a thermostat attached to a water bath that is $25.00 \pm 0.01^\circ\text{C}$. The solution density, d , is related to the period of vibration of the tube, T_v , by the following:

$$d = A + BT_v^2 \quad (3.2)$$

where A , B are two instrumental constants. The determination of these constants is based on the period of two reference systems: air ($d_{\text{air}} = 0.00115$ g cm⁻³) and water ($d_{\text{water}} = 0.997045$ g cm⁻³). An accurate value of the density of air was estimated by a state equation that shows dependence on the pressure, temperature (25.00°C), and humidity.

3.4 Boundary Spreading Experiments.

All diffusion-based boundary spreading experiments were made with the high-precision Gosting diffusimeter operated in its Rayleigh interferometric optical mode.^{76, 79-81} A boundary-spreading experiment begins with the preparation of a sharp boundary (using a peristaltic pump) between a surfactant-water solution (bottom solution) and water (top solution) inside a vertical channel of a Tiselius cell (Figure 10a). For experiments with TX-100 in the presence of salts, a surfactant-salt-water solution (bottom solution) is interfaced with

a salt-water solution (top solution) at the same salt concentration. Except for the Brij-30 case, all surfactant aqueous solutions exhibit higher density than the corresponding surfactant-free solutions, and they are therefore located at the bottom of the vertical channel to prevent convection.

As diffusion occurs, boundary broadening occurs (Figure 10b). Experiments are completed before the boundary spreads throughout the diffusion channel so that the compositions at the two-channel extremities remain the same within the experimental error and the free-boundary condition applies.

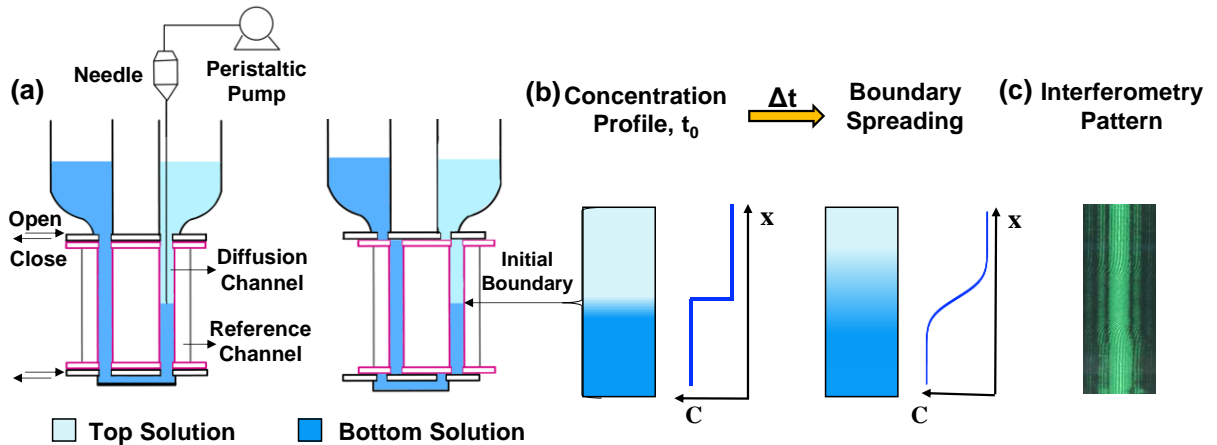


Figure 10. Diffusion-based boundary spreading between (a) two solutions within a Tiselius cell. (b) Concentration profile evolution, $C_P(x,t)$, as boundary spreads. (c) Interferometry pattern measured by Gosting diffusimeter.

The light source used for generating the Rayleigh interference pattern is a He-Ne Uniphase laser with wavelength $\lambda = 543.5$ nm. A cell holder is located inside a water bath. The temperature of the bath was regulated (± 0.001 °C) at 25.00 °C. The cell holder has the function to support a Tiselius cell, where diffusion occurs, and a mask, which consists of a double window. Here, the laser beam is split into two parts: one going through the diffusion channel

of the Tiselius cell and one passing through the water bath (reference channel). A pair of two-cylinder lenses focus the diffusion channel onto the detector, where the Rayleigh interference pattern is observed and recorded (Figure 11).

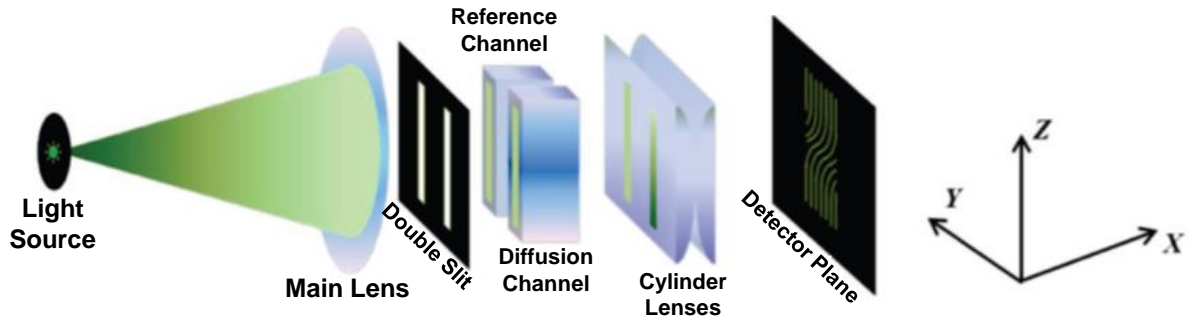


Figure 11. Scheme of Gosting diffusimeter operating in Rayleigh interferometric optical mode.

If a homogeneous liquid (solution or water) occupies the entire diffusion channel, then a set of vertical parallel Rayleigh fringes will be generated. For liquid mixtures with a vertically nonuniform concentration, Rayleigh fringes shift horizontally as the refractive index inside the diffusion channel changes with vertical height. This gives direct information about the refractive index versus vertical position and leads to the determination of the surfactant concentration profile, as discussed below.

Data from the Rayleigh interference patterns were collected with a linear charge-coupled device (CCD) array (6000 pixels, $10\ \mu\text{m} \times 10\ \mu\text{m}$ pixels), mounted vertically on a precision stage. For a given experiment, at least 10 interference patterns were collected at different times. For a given interference pattern, vertical positions along the recorded pattern were converted into the actual positions inside the diffusion channel, X , using the known magnification factor of 1.7108. Vertical positions were then converted into the corresponding reduced positions, $Y \equiv X \cdot (2t)^{-1/2}$, where t is the time at which the position was recorded after

the experiment start. The stage with this vertical array was stepped horizontally through the two-dimensional interference pattern to collect the data necessary to characterize a surfactant concentration profile.

Data acquisition was controlled via computer, which also performed the subsequent data reduction. If one starts from a fringe location corresponding to the surfactant-free solution ($C_P = 0$) inside the diffusion channel and vertically moves toward the surfactant solution ($C_P = C_{\max}$) through the pattern, the horizontal shift of the fringe can be determined until becomes as large as the distance between two adjacent fringes. At this vertical position, one fringe is crossed. As the location of the initial surfactant solution is finally reached ($C_P = C_{\max}$), a total of, \mathcal{J} , fringes will be crossed. Note that the total number of fringes, \mathcal{J} , is not an integer in general because it is directly proportional to the difference in refractive index between the surfactant solution and water. At a given reduced position, Y , a recorded fringe shift, j , is given by the sum of the number of fringes crossed and the fractional shift of a fringe. The vertical position associated with $j = \mathcal{J}/2$ is set to correspond to $Y = 0$.

To extract the corresponding surfactant concentration profile, $C_P(Y)$, we set $C_P/C_{\max} = j / \mathcal{J}$ at any given Y . In other words, we assume that the solution refractive index is a linear function of surfactant concentration. This is an approximation since the refractive-index contribution of a free surfactant molecule is slightly different from that of a micellar surfactant molecule.⁷³ Both approximations are not expected to affect the determination of C^* within the method experimental error. An individual interference pattern obtained during a boundary-spreading experiment can be separately analyzed for the determination of C^* . Thus, the analysis of multiple interference patterns associated with a single experiment was used to extract the average and standard deviation of all C^* values extracted.

CHAPTER 4

RESULTS AND DISCUSSION

4.1 Boundary Spreading Characterization

Representative concentration profiles, $C_P(Y)$, characterizing boundary spreading between micellar aqueous solutions and water are illustrated in Figure 12 A-C for TX-100, SDS, and Brij-30, respectively. The concentration gradients, dC_P/dY , were numerically deduced from the $C_P(Y)$ curves. These are shown under the corresponding concentration profiles.

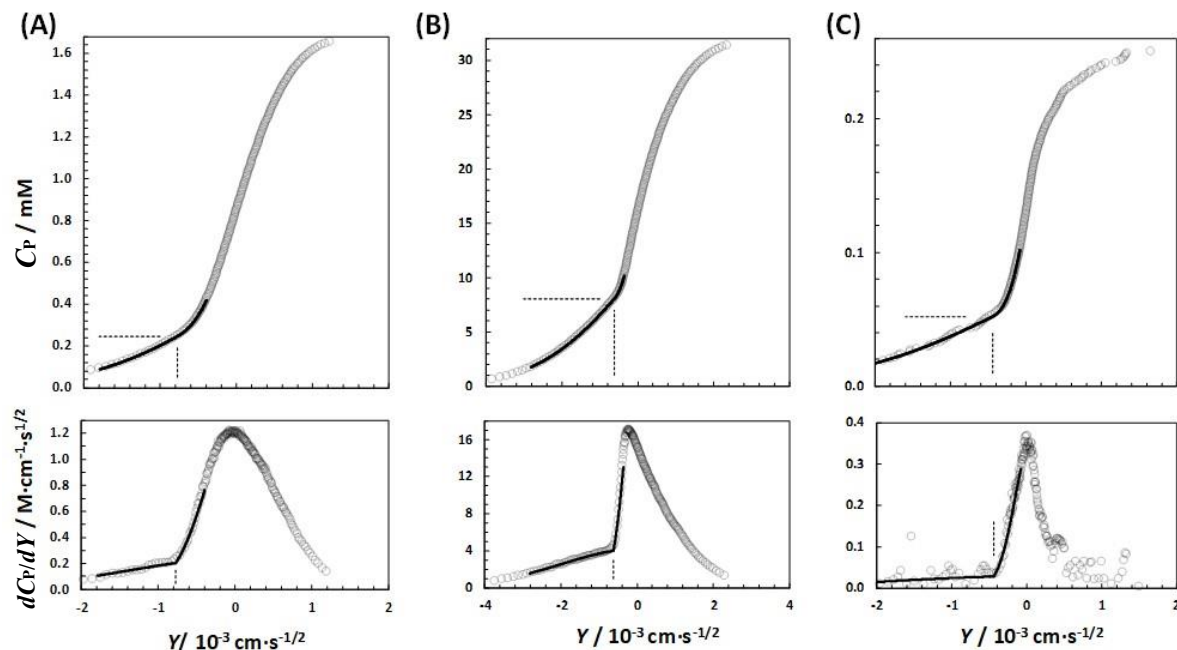


Figure 12. Sigmoidal concentration profiles, $C_P(Y)$, are characterizing boundary spreading between a surfactant-water solution and water at 25 °C for TX-100 (A), SDS (B), and Brij-30 (C). The bottom figures show the corresponding profiles of the concentration gradient, dC_P/dY . Vertical dashed lines locate Y^* , while the corresponding horizontal dashed lines locate C^* . Solid curves are fit through the experimental data, which are discussed further below.

In the absence of micelle dissociation, the $C_P(Y)$ sigmoidal curves are expected to be described by $C_P = (C_{\max}/2) \cdot [1 + \text{erf}(D_M^{-1/2}Y)]$.⁷⁵ Correspondingly, first derivatives should be described by a centrosymmetric Gaussian function: $dC_P/dY = C_{\max} \cdot (\pi D_M)^{-1/2} \cdot \exp(-Y^2/D_M)$. However, our experimental data of $C_P(Y)$ (see Figure 12, top) show a significant deviation from this behavior due to dilution-induced micelle dissociation. This deviation becomes especially noticeable when inspecting the corresponding dC_P/dY profiles (see Figure 12, bottom). Here, we can observe an abrupt change in slope at a well-defined value of $Y = Y^*$. This is then used to identify the value of C^* for the surfactant in the corresponding $C(Y)$ curve (see dashed lines in Figure 12). Since experiments were designed such that $C^* < C_{\max}/2$, Y^* is located on the left side of the maximum of dC_P/dY . Note that a sharp slope change occurs between Y^* and the location of the maximum at $Y \approx 0$. Although the direct inspection of our experimental data is expected to give critical micelle concentrations by graphic interpolation, it is convenient to identify a mathematical expression that yields the value of C^* by applying the method of least squares to experimental data. This is described in the following section.

4.2 Modified Pseudo-Phase Separation Model

The basic theoretical model discussed in Chapter 2, Section 2.4, represents the starting point of this analysis. However, dC_P/dY is predicted to exhibit a discontinuity point at $Y = Y^*$ according to the pseudo-phase separation model (see Chapter 2, Section 2.4), in disagreement with the experimental behavior in Figure 12 A-C. This deviation, which makes the direct application of eqs. (2.19), (2.23), (2.24), in Section 2.4, to experimental data not practicable, is mainly related to a shortcoming of the pseudo-phase separation model. Indeed, it is expected that mass-action-law models⁸² more realistically describe the behavior of the diffusion coefficient as a function of surfactant concentration around $Y = Y^*$. According to mass-action-

law models, the diffusion coefficient $D_P(C_P)$ in eq. (2.11) will exhibit an inflection point around $C = C^*$.^{69-71, 83} Correspondingly, the gradient, dC_P/dY , is expected to remain a continuous function at $Y = Y^*$. However, the implementation of these models significantly increases mathematical complexity, making them also impracticable for our data analysis. Furthermore, even with a hypothetically exact thermodynamic description of micellization, the corresponding model for $D_P(C_P)$ would remain approximate due to the assumption that D_1 and D_M are constants, independent of concentration.⁷³ Finally, in the case of ionic surfactants, the presence of the counterion further increases model complexity due to the common-ion effect, electrostatic dragging effects, counterion partial binding to micelles, and electrostatic and electrophoretic interactions.^{73, 84} Since we are specifically interested in the determination of C^* , it is practically convenient to retain the pseudo-phase separation model for non-ionic surfactants and introduce corrections that would make this model suitable for examining experimental data for both non-ionic and ionic surfactants.

As a first modification to the pseudo-phase separation model, we impose that dC_P/dY is a continuous function at $Y = Y^*$. This is achieved by assuming that D_P is a continuous function at $C = C^*$ as expected from the chemical-equilibrium model. If we then set D_P to be the same at $y \rightarrow y^{*-}$ and $y \rightarrow y^{*+}$, eq. (2.20) (see Section 2.4) becomes a continuity condition for the concentration gradient: $dC_P/dy|_{y \rightarrow y^{*-}} = dC_P/dy|_{y \rightarrow y^{*+}}$, consistent with the experimental behavior. Correspondingly, eq. (2.23) must be replaced by:

$$\frac{C^*}{C_{\max} - C^*} = \left(\frac{D_M}{D_1} \right)^{-1/2} \frac{1 + \operatorname{erf}(D_1^{-1/2} y^*)}{1 - \operatorname{erf}(D_M^{-1/2} y^*)} e^{-\left(\frac{1}{D_M} - \frac{1}{D_1} \right) y^{*2}} \quad (4.1)$$

In Figure 13 we show theoretical concentration profiles calculated from eq (2.19) with $C^*/C_{\max} = 0.25$ and $D_1 / D_M = 10$. For comparison, we have applied both eq. (2.23) (dashed

curves) and eq. (4.1) (solid curves). We can see that $C_P(Y)$ for the modified pseudo-phase separation model smoothly changes around $Y = Y^*$. Correspondingly, dC_P/dY remains a continuous function at $Y = Y^*$. Note that the slope of dC_P/dY retains its discontinuity at $Y = Y^*$ as we can appreciate from the more rapid increase of dC_P/dY after $Y = Y^*$.

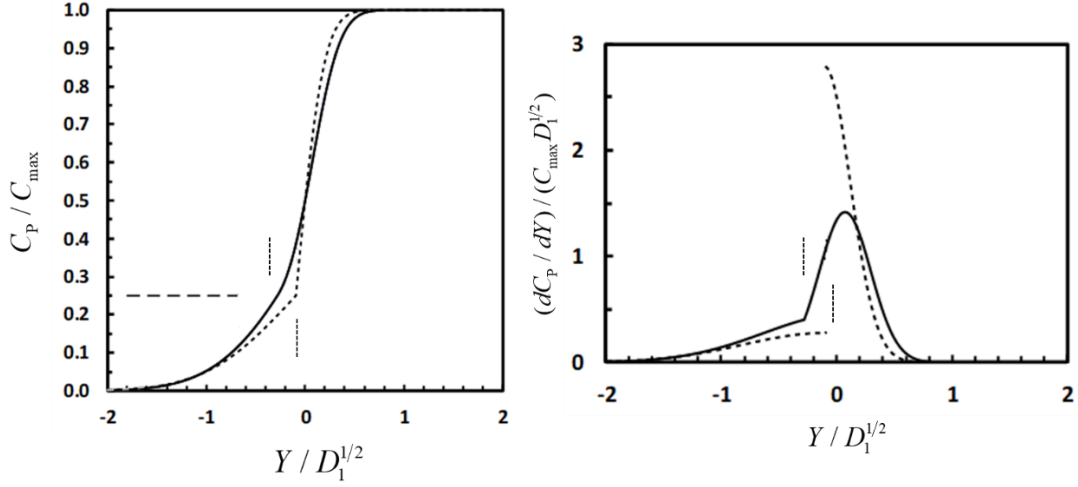


Figure 13. Left, theoretical concentration profile, $C_P(Y)$, extracted from eq. (2.19) based on the modified model (eq (4.1); solid curve) with $D_1 / D_M = 10$ and $C^* / C_{\max} = 0.25$. For comparison, the corresponding concentration profile of the basic model (eq. (2.23); dashed curve) is included. The right figure shows the corresponding profiles of the concentration gradient, dC/dY . Vertical dashed lines locate Y^* , while the corresponding horizontal dashed line locates C^* / C_{\max} .

Furthermore, we can see that an inflection point in the behavior of dC_P/dY occurs at $Y > Y^*$ followed by a maximum, in qualitative agreement with the experimental behavior in Figure 12A-C. On the other hand, the dC_P/dY curve generated from the basic pseudo-phase separation model exhibits a marked discontinuity at $Y = Y^*$ with dC_P/dY sharply increasing. Moreover, the slope of dC_P/dY (d^2C_P/dY^2) even switches signs from positive to negative as Y increases. Due to this discontinuity point, the behavior of dC_P/dY lacks the inflection and maximum points that emerged in the curve generated from the modified model.

The proposed modification alone is not sufficient for a satisfactory application of the method of least squares to our data as it fails to correctly describe the magnitude and location of the experimental maximum of dC_P/dY . This failure is also caused by a concentration dependence of D_M , a problem that becomes especially important for ionic surfactants such as SDS. In this case, the counterion dragging effect on micelle diffusion, which is ignored in our model, makes micelle diffusion significantly increase with surfactant concentration.^{73, 84} To overcome this issue, a second modification is introduced in the model by revisiting eq. (2.24), which links y_c ($Y = 0$) to y^* ($Y = Y^*$). We specifically generalize eq. (2.24) into:

$$\operatorname{erf}(D_M^{-1/2} y_c) = 1 - \frac{1 - \operatorname{erf}(D_M^{-1/2} y^*)}{2\alpha(1 - C^*/C_{\max})} \quad (4.2)$$

Where we have introduced a new fitting parameter, α (with $\alpha = 1$ in eq. (2.24)). Replacing eq. (2.24) with eq (4.2) makes $C_P(Y)$ theoretical curves no longer satisfy the condition of $C = C_{\max}/2$ at $Y = 0$ in general. Thus, we chose to apply the method of least squares to experimental values of $C_P(Y)$ on the left side of the maximum of dC_P/dY , ending around dC_P/dY inflection point as shown by the solid curves in Figure 13A-C. On the other hand, the lowest experimental value of $C_P(Y)$ to be examined was chosen to correspond to $\approx 5\%$ of C_{\max} , to reduce errors associated with experimental noise. Furthermore, this lower limit significantly reduces deviations of experimental data from the theoretical behavior of $C_P(Y)$ in the case of ionic surfactants, for which a strong concentration dependence of D_1 at very low surfactant concentrations is known⁷³ to occur. Despite these two chosen boundaries, the number of experimental data points to be analyzed around the critical micelle concentration remains large. Extracted values of C^* for the three investigated surfactants are reported in Table 1. These are

in excellent agreement with the corresponding literature values ⁸⁵⁻⁸⁹ within the experimental error.

Table 1. Values of C^* of surfactant-water solutions at 25 °C

Surfactant	C_{\max}/mM	C^*/mM
SDS	32.00	8.03 ± 0.06^a
Brij-30	0.2551	0.051 ± 0.002
TX-100	1.689	0.236 ± 0.008

^a Values of C^* are averages of values extracted from different interference patterns. Corresponding errors are 2×standard deviations.

4.3 Effect of Salt on Critical Micelle Concentration

As mentioned in chapter 1, we are interested in studying diffusiophoresis of tyloxapol micelles. Hence, we were looking to determine the effect of salts on tyloxapol cmc. However, the very low cmc of this surfactant (an order of magnitude lower than our method detection limit) did not allow us to detect the cmc for this surfactant from the concentration profiles. Nonetheless, because tyloxapol (see Figure 3) is an oligomer of triton X-100 (see Figure 7) we decided to study the effect of salt on TX-100 cmc. This characterization is relevant to tyloxapol because of similarities in surfactant chemical structures (PEG groups).

The precision of C^* data. ($\approx 3\%$ for TX-100) is sufficiently high that the effect of salt concentration and type on C^* could be successfully characterized in the case of this nonionic surfactant. We have specifically considered Na_2SO_4 , as representative sulfate salt that will be used for the diffusiophoresis studies. Additionally, for completeness, we considered NaCl , and NaSCN due to their relevance to the Hofmeister series.^{83, 90, 91} In this series, anions such

as SO_4^{2-} display a great salting-out strength favoring the precipitation of water-soluble macromolecules such as proteins and PEG, whereas Cl^- is regarded as a mild anion located approximately at the midpoint of the Hofmeister series, separating salting-out from salting-in anions such as SCN^- . This ranking was also observed in the case of polyethylene glycol (PEG) in water,^{5, 92} which represents the hydrophilic group of TX-100. However, PEG hydrophilic groups are not expected to undergo major environment changes upon micelle formation. Thus, salt effects should be mainly caused by ion interactions with hydrocarbon groups. Based on this argument, micelle disaggregation shares more similarities with protein unfolding. Here, anions such as SO_4^{2-} hinder protein unfolding and stabilize its native folded state while the SCN^- anion should favor unfolding.⁷¹ For micelles, a salt-induced decrease $\ln C^*$ corresponds to an increase in micelle thermodynamic stability.⁹⁰

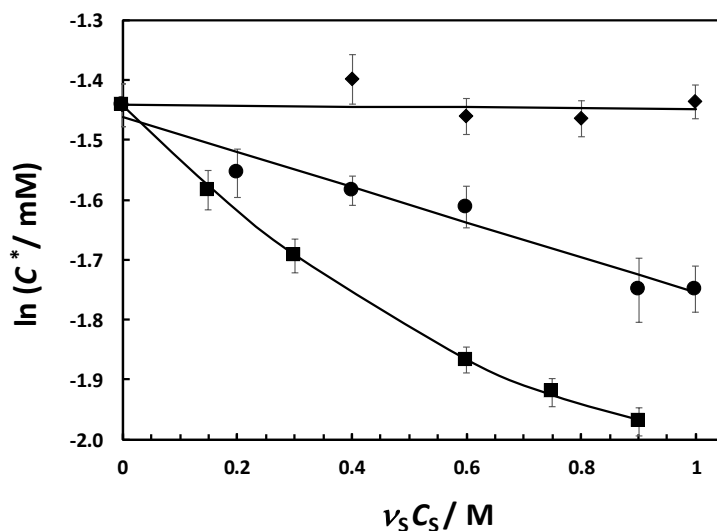


Figure 14. The logarithm of critical micelle concentration, $\ln C^*$, as a function of ion concentration, for TX-100 at 25 °C in aqueous NaCl (circles), Na_2SO_4 (squares), and NaSCN (diamonds). Solid curves are fitting through experimental data.

Our experimental results of $\ln C^*$ are plotted in Figure 14 as a function of salt (S) osmolarity, $\nu_s C_s$, where ν_s is the number of ions per formula unit and C_s is salt molar concentration. In the Na_2SO_4 and NaCl cases, $\ln C^*$ decreases as ion concentration increase with the salting-out effect induced by Na_2SO_4 being about three times larger than that induced by NaCl . On the other hand, the effect of NaSCN on $\ln C^*$ was found to be negligible within the experimental error. The determined effect of anion type on C^* , which follows the Hofmeister series, is in good agreement with the literature.⁹⁰ Extracted values of C^* for each salt are reported in Table 2.

Table 2. Values of C^* of Triton-X100-salt-water solutions at 25 °C.

Salt	C_{\max}/mM	C^*/mM
NaCl, 0.10 M	1.716	0.211±0.009
NaCl, 0.20 M	1.708	0.205±0.005
NaCl, 0.30 M	1.705	0.199±0.007
NaCl, 0.45 M	1.537	0.174±0.009
Na_2SO_4 , 0.05 M	1.681	0.205±0.007
Na_2SO_4 , 0.10 M	1.687	0.184±0.005
Na_2SO_4 , 0.20 M	1.670	0.154±0.003
Na_2SO_4 , 0.25 M	1.702	0.146±0.003
Na_2SO_4 , 0.30 M	1.640	0.139±0.003
NaSCN , 0.20 M	1.690	0.247±0.010
NaSCN , 0.30 M	1.694	0.232±0.007
NaSCN , 0.40 M	1.700	0.231±0.005
NaSCN , 0.50 M	1.711	0.238±0.005

CHAPTER 5

CONCLUSIONS

Experimental one-dimensional concentration profiles, $C_P(Y)$, characterizing the spreading of the boundary between micellar aqueous solutions and water were successfully determined and analyzed for the determination of critical micelle concentrations, C^* , in three surfactant cases (TX-100, SDS, and Brij-30). Position of C^* can be identified by visual inspection of the corresponding concentration-gradient profiles, dC/dY (see Figure 12A-C). In the TX-100 case, $C_P(Y)$ was also characterized in the presence of a uniform salt concentration of Na_2SO_4 , NaCl , and NaSCN .

To precisely determine C^* , a theoretical expression of $C_P(Y)$ was developed by considering the pseudo-phase separation model for non-ionic surfactants as a starting point. Modifications were then incorporated into the theoretical expression of $C_P(Y)$ allowing for limitations of the pseudo-phase separation model. This keeps mathematical complexity still adequate for applications to experimental data analysis of both non-ionic and ionic surfactants using the method of least squares. Due to model shortcomings, C^* values are expected to be method dependent. Nevertheless, they were found to fall within the range of C^* data reported in the literature. Within the framework of our method, the precision of the determined values of C^* was found to be $\approx 3\%$ and $\approx 0.01 \text{ g}\cdot\text{L}^{-1}$ represents the lowest value of C^* that can be detected by Rayleigh interferometry based on Brij-30 results.

While Rayleigh interferometry was employed for the characterization of $C_P(Y)$ in our experiments, concentration profiles can be in principle also extracted using other techniques such as absorption spectroscopy. This work provides the foundation of diffusion-based

methods for the determination of C^* . These are non-invasive, require single-sample preparation, and apply to both non-ionic and ionic surfactants.

Finally, the cmc of tyloxapol could not be detected from the concentration profiles due to its cmc been too low ($0.003 \text{ g}\cdot\text{L}^{-1}$). Nonetheless, tyloxapol is an oligomer of TX-100 and we can assume that Na_2SO_4 also reduces the cmc of tyloxapol. This allows us to neglect the amount of free surfactant present in solution for the diffusiophoresis studies.

Future directions for this method are to characterize the cmc of mixed surfactant micelles. Mixed micelles allow to enhance the properties of the micellar system by combining more than one surfactant, potentially broadening their applications.

CHAPTER 6

THERMODYNAMIC THEORY BACKGORUND

6.1 Ternary Colloidal Particle(P)-Salt(S)-Water(W) System

The thermodynamic behavior of solutions plays an important role in the interpretation of diffusion and diffusiophoresis. Since micelles are colloidal particles, we review the thermodynamic theory of colloidal particles in water in the presence of salt in this chapter. We shall use the terms P, S and W to denote colloidal particles, salt and water (solvent), respectively. It is also important to note that colloidal particles are electrically neutral and large compared to salt ions and water.

Ternary systems can be described by four thermodynamic variables: pressure (p), temperature (T), and two composition variables such as molar concentrations of particles and salt, C_P and C_S . In our case, p and T are constant so they will be omitted to shorten notation. We will focus on the case in which concentration of colloidal particles is low (diluted suspensions of colloidal particles with volume fractions less than 1%), while there is no limitation on salt concentration.

To describe the thermodynamics of ternary systems, we start with Gibbs free energy. The Gibbs free energy (G) of a ternary solution consisting of n_P moles of colloidal particle, n_S moles of salt, and n_W moles of water can be expressed as:⁹³

$$G(n_P, n_S, n_W) = n_P \mu_P + n_S \mu_S + n_W \mu_W \quad (6.1)$$

The corresponding chemical potentials (μ_j with $j=P,S,W$) then are:

$$\mu_P \equiv \left(\frac{\partial G}{\partial n_P} \right)_{n_S, n_W} \quad (6.2)$$

$$\mu_S \equiv \left(\frac{\partial G}{\partial n_S} \right)_{n_P, n_W} \quad (6.3)$$

$$\mu_W \equiv \left(\frac{\partial G}{\partial n_W} \right)_{n_P, n_S} \quad (6.4)$$

The Gibbs-Duhem relation shows how changes in chemical potentials are related to each other:

$$n_P d\mu_P + n_S d\mu_S + n_W d\mu_W = 0 \quad (6.5)$$

Since the chemical potential of a component in the mixture cannot change independently from the chemical potential of the other components, we need only two chemical potentials to describe ternary systems. In our case, we choose particle and salt chemical potential. We can express the system chemical potentials for the particle, μ_P , and for the salt, μ_S , as a function of particle concentration, C_P , and salt concentration C_S :

$$\mu_P(C_P, C_S) = \mu_P^0 + RT [\ln C_P + \ln f_P(C_P, C_S)] \quad (6.6)$$

$$\mu_S(C_P, C_S) = \mu_S^0 + \nu_S RT [\ln C_S + \ln f_S(C_P, C_S)] \quad (6.7)$$

where μ_p^0 and m_s^0 are the standard chemical potentials, f_p and f_s are the activity coefficients for the particles and the salt, respectively, R is the ideal gas constant and n_s correspond to the number of ions from the salt. In our case, $n_s = 3$ for Na_2SO_4 and $\nu_s = 2$ for MgSO_4 .

Activity coefficients satisfy the ideal-dilute conditions:

$$\lim_{C_p \rightarrow 0, C_s \rightarrow 0} f_p(C_p, C_s) = 1 \quad (6.8)$$

$$\lim_{C_p \rightarrow 0, C_s \rightarrow 0} f_s(C_p, C_s) = 1 \quad (6.9)$$

In the context of diffusion (see chapter 7, section 7.1), thermodynamic driving forces are linked to the first derivatives of chemical potentials. We therefore deduce expressions of first derivatives from (6.6) and (6.7):

$$\mu_{pp} \equiv \left(\frac{\partial \mu_p}{\partial C_p} \right)_{C_s} = \frac{RT}{C_p} \left[1 + \left(\frac{\partial \ln f_p}{\partial \ln C_p} \right)_{C_s} \right] \quad (6.10)$$

$$\mu_{ps} \equiv \left(\frac{\partial \mu_p}{\partial C_s} \right)_{C_p} = \frac{RT}{C_s} \left(\frac{\partial \ln f_p}{\partial \ln C_s} \right)_{C_p} \quad (6.11)$$

$$\mu_{sp} \equiv \left(\frac{\partial \mu_s}{\partial C_p} \right)_{C_s} = \frac{\nu_s RT}{C_p} \left(\frac{\partial \ln f_s}{\partial \ln C_p} \right)_{C_s} \quad (6.12)$$

$$\mu_{ss} \equiv \left(\frac{\partial \mu_s}{\partial C_s} \right)_{C_p} = \frac{\nu_s RT}{C_s} \left[1 + \left(\frac{\partial \ln f_s}{\partial \ln C_s} \right)_{C_p} \right] \quad (6.13)$$

It is important to note that μ_{sp} (see eq. (6.12)) and μ_{ps} (see eq. (6.11)) are mathematically linked to each other. To show this, it is convenient to introduce two new composition variables:

$$m_p \equiv n_p / n_w \quad (6.14)$$

$$m_s \equiv n_s / n_w \quad (6.15)$$

We then take the cross-derivative, $(\partial\mu_p/\partial m_s)_{m_p}$ of the particle chemical potential (eq. (6.3)):

$$\left(\frac{\partial\mu_p}{\partial m_s}\right)_{m_p} = \left[\frac{\partial}{\partial m_s} \left(\frac{\partial G}{\partial n_p} \right)_{n_s, n_w} \right]_{m_p} \quad (6.16)$$

And substitute n_p with $m_p n_w$ (see eq. (6.14)) in eq. (6.16) to obtain:

$$\left(\frac{\partial\mu_p}{\partial m_s}\right)_{m_p} = \frac{1}{n_w} \left[\frac{\partial}{\partial m_s} \left(\frac{\partial G}{\partial m_p} \right)_{m_s, n_w} \right]_{m_p} \quad (6.17)$$

Following the same approach for the other cross-derivative, $(\partial\mu_s/\partial m_p)_{m_s}$, (see eq. (6.3) and substituting $n_s = m_s n_w$ (see eq. (6.15)), we obtain:

$$\left(\frac{\partial\mu_s}{\partial m_p}\right)_{m_s} = \frac{1}{n_w} \left[\frac{\partial}{\partial m_p} \left(\frac{\partial G}{\partial m_s} \right)_{m_p, n_w} \right]_{m_s} \quad (6.18)$$

The expressions in the square brackets in eqs. (6.17) and (6.18) are two mixed second-order partial derivatives of G that are equal to each other. This implies that

$$\left(\frac{\partial\mu_p}{\partial m_s}\right)_{m_p} = \left(\frac{\partial\mu_s}{\partial m_p}\right)_{m_s} \quad (6.19)$$

Equation (6.19) is used to relate μ_{sp} (see eq. (6.12)) to μ_{ps} (see eq. (6.11)) in the following way. We first write the total differentials for both chemical potentials:

$$d\mu_P = \left(\frac{\partial \mu_P}{\partial C_P} \right)_{C_S} dC_P + \left(\frac{\partial \mu_P}{\partial C_S} \right)_{C_P} dC_S = \mu_{PP} dC_P + \mu_{PS} dC_S \quad (6.20)$$

$$d\mu_S = \left(\frac{\partial \mu_S}{\partial C_P} \right)_{C_S} dC_P + \left(\frac{\partial \mu_S}{\partial C_S} \right)_{C_P} dC_S = \mu_{SP} dC_P + \mu_{SS} dC_S \quad (6.21)$$

We then take four partial derivatives of μ_P and μ_S with respect to both m_P and m_S :

$$\left(\frac{\partial \mu_P}{\partial m_P} \right)_{m_S} = \mu_{PP} \left(\frac{\partial C_P}{\partial m_P} \right)_{m_S} + \mu_{PS} \left(\frac{\partial C_S}{\partial m_P} \right)_{m_S} \quad (6.22)$$

$$\left(\frac{\partial \mu_P}{\partial m_S} \right)_{m_P} = \mu_{PP} \left(\frac{\partial C_P}{\partial m_S} \right)_{m_P} + \mu_{PS} \left(\frac{\partial C_S}{\partial m_S} \right)_{m_P} \quad (6.23)$$

$$\left(\frac{\partial \mu_S}{\partial m_P} \right)_{m_S} = \mu_{SP} \left(\frac{\partial C_P}{\partial m_P} \right)_{m_S} + \mu_{SS} \left(\frac{\partial C_S}{\partial m_P} \right)_{m_S} \quad (6.24)$$

$$\left(\frac{\partial \mu_S}{\partial m_S} \right)_{m_P} = \mu_{SP} \left(\frac{\partial C_P}{\partial m_S} \right)_{m_P} + \mu_{SS} \left(\frac{\partial C_S}{\partial m_S} \right)_{m_P} \quad (6.25)$$

At this stage, we need to find an expression for each $\partial C_i / \partial m_j$ ($m_k, k \neq j$) in eqs. (6.22) to (6.25). This requires us to examine how the volume, V , of a ternary system depends on composition. We therefore write:

$$V(n_P, n_S, n_W) = n_P \bar{V}_P + n_S \bar{V}_S + n_W \bar{V}_W \quad (6.26)$$

where,

$$\bar{V}_P \equiv \left(\frac{\partial V}{\partial n_P} \right)_{n_S, n_W} \quad (6.27)$$

$$\bar{V}_S \equiv \left(\frac{\partial V}{\partial n_S} \right)_{n_P, n_W} \quad (6.28)$$

$$\bar{V}_W \equiv \left(\frac{\partial V}{\partial n_W} \right)_{n_P, n_S} \quad (6.29)$$

are the partial molar volumes of the three system components. Thus, molar concentrations can be written as follows:

$$C_P = \frac{n_P}{V} = \frac{n_P}{n_P \bar{V}_P + n_S \bar{V}_S + n_W \bar{V}_W} = \frac{m_P}{m_P \bar{V}_P + m_S \bar{V}_S + \bar{V}_W} \quad (6.30)$$

$$C_S = \frac{n_S}{V} = \frac{n_S}{n_P \bar{V}_P + n_S \bar{V}_S + n_W \bar{V}_W} = \frac{m_S}{m_P \bar{V}_P + m_S \bar{V}_S + \bar{V}_W} \quad (6.31)$$

We use these expressions of concentration (eqs. (6.30) and (6.31)) to take partial derivatives with respect to m_P and m_S . Keeping in mind Gibbs-Duhem equation:

$n_P d\bar{V}_P + n_S d\bar{V}_S + n_W d\bar{V}_W = 0$ or equivalently, $m_P d\bar{V}_M + m_S d\bar{V}_S + d\bar{V}_W = 0$. We obtain:

$$\left(\frac{\partial C_P}{\partial m_P} \right)_{m_S} = \frac{1}{m_P \bar{V}_P + m_S \bar{V}_S + \bar{V}_W} - \frac{\bar{V}_P m_P}{(m_P \bar{V}_P + m_S \bar{V}_S + \bar{V}_W)^2} = \frac{n_W}{V} (1 - \bar{V}_P C_P) \quad (6.32)$$

$$\left(\frac{\partial C_P}{\partial m_S} \right)_{m_P} = - \frac{\bar{V}_S m_P}{(m_P \bar{V}_P + m_S \bar{V}_S + \bar{V}_W)^2} = - \frac{n_W}{V} \bar{V}_S C_P \quad (6.33)$$

$$\left(\frac{\partial C_S}{\partial m_P}\right)_{m_S} = -\frac{\bar{V}_P m_S}{(m_P \bar{V}_P + m_S \bar{V}_S + \bar{V}_W)^2} = -\frac{n_W}{V} \bar{V}_P C_S \quad (6.34)$$

$$\left(\frac{\partial C_S}{\partial m_S}\right)_{m_P} = \frac{1}{m_P \bar{V}_P + m_S \bar{V}_S + \bar{V}_W} - \frac{\bar{V}_S m_S}{(m_P \bar{V}_P + m_S \bar{V}_S + \bar{V}_W)^2} = \frac{n_W}{V} (1 - \bar{V}_S C_S) \quad (6.35)$$

Substituting eqs. (6.32) to (6.35) into eqs. (6.22) to (6.25) allows us to write:

$$\left(\frac{\partial \mu_P}{\partial m_P}\right)_{m_S} = \frac{n_W}{V} \left[(1 - \bar{V}_P C_P) \mu_{PP} - \bar{V}_S C_P \mu_{PS} \right] \quad (6.36)$$

$$\left(\frac{\partial \mu_P}{\partial m_S}\right)_{m_P} = \frac{n_W}{V} \left[(1 - \bar{V}_S C_S) \mu_{PS} - \bar{V}_S C_P \mu_{PP} \right] \quad (6.37)$$

$$\left(\frac{\partial \mu_S}{\partial m_P}\right)_{m_S} = \frac{n_W}{V} \left[(1 - \bar{V}_P C_P) \mu_{SP} - \bar{V}_P C_S \mu_{SS} \right] \quad (6.38)$$

$$\left(\frac{\partial \mu_S}{\partial m_S}\right)_{m_P} = \frac{n_W}{V} \left[(1 - \bar{V}_S C_S) \mu_{SS} - \bar{V}_S C_P \mu_{SP} \right] \quad (6.39)$$

Finally, substitution of eq. (6.37) and (6.38) in eq. (6.19), which related μ_{PS} with μ_{SP} , yields:

$$(1 - \bar{V}_S C_S) \mu_{PS} - \bar{V}_S C_P \mu_{PP} = (1 - \bar{V}_P C_P) \mu_{SP} - \bar{V}_P C_S \mu_{SS} \quad (6.40)$$

Equation (6.40) can be rearranged in the following way:

$$(1 - \bar{V}_P C_P) \frac{\mu_{SP}}{\mu_{SS}} = (1 - \bar{V}_S C_S) \frac{\mu_{PS}}{\mu_{SS}} + \bar{V}_P C_S - \bar{V}_S C_P \frac{\mu_{PP}}{\mu_{SS}} \quad (6.41)$$

Interestingly, the ratio $\mu_{\text{SP}} / \mu_{\text{SS}}$ in eq. (6.41) is a salt partitioning coefficient. Indeed, we can write:

$$\frac{\mu_{\text{SP}}}{\mu_{\text{SS}}} = \left(\frac{\partial \mu_{\text{S}}}{\partial C_{\text{P}}} \right)_{C_{\text{S}}} \left(\frac{\partial C_{\text{S}}}{\partial \mu_{\text{S}}} \right)_{C_{\text{P}}} = - \left(\frac{\partial \mu_{\text{S}}}{\partial C_{\text{S}}} \right)_{C_{\text{P}}} \left(\frac{\partial C_{\text{S}}}{\partial C_{\text{P}}} \right)_{\mu_{\text{S}}} \left(\frac{\partial C_{\text{S}}}{\partial \mu_{\text{S}}} \right)_{C_{\text{P}}} = - \left(\frac{\partial C_{\text{S}}}{\partial C_{\text{P}}} \right)_{\mu_{\text{S}}} \quad (6.42)$$

In the limit of $C_{\text{P}} \rightarrow 0$, eqs. (6.10) and (6.13) reduce to:

$$\frac{\mu_{\text{PP}}}{RT} \equiv \frac{1}{RT} \left(\frac{\partial \mu_{\text{P}}}{\partial C_{\text{P}}} \right)_{C_{\text{S}}} = \frac{1}{C_{\text{P}}} \left[1 + C_{\text{P}} \left(\frac{\partial \ln f_{\text{P}}}{\partial C_{\text{P}}} \right)_{C_{\text{S}}} \right] = \frac{1}{C_{\text{P}}} \quad (6.43)$$

$$\frac{\mu_{\text{SS}}}{RT} \equiv \frac{1}{RT} \left(\frac{\partial \mu_{\text{S}}}{\partial C_{\text{S}}} \right)_{C_{\text{P}}} = \frac{\nu_{\text{S}}}{C_{\text{S}}} \left[1 + C_{\text{S}} \left(\frac{\partial \ln f_{\text{S}}}{\partial C_{\text{S}}} \right)_{C_{\text{P}}} \right] = \frac{\nu_{\text{S}} y_{\text{S}}}{C_{\text{S}}} \quad (6.44)$$

where $y_{\text{S}}(C_{\text{S}}) \equiv \lim_{C_{\text{P}} \rightarrow 0} \left[1 + (\partial \ln f_{\text{S}} / \partial \ln C_{\text{S}})_{C_{\text{P}}} \right]$ is a salt non-ideality thermodynamic factor with $\lim_{C_{\text{S}} \rightarrow 0} y_{\text{S}}(C_{\text{S}}) = 1$. For many salts, $y_{\text{S}}(C_{\text{S}})$ can be calculated from available thermodynamic data on binary salt-water systems.

Furthermore, in the limit of $C_{\text{P}} \rightarrow 0$, eq. (6.41) becomes:

$$\lim_{C_{\text{P}} \rightarrow 0} \frac{\mu_{\text{SP}}}{\mu_{\text{SS}}} = (1 - \bar{V}_{\text{S}} C_{\text{S}}) \lim_{C_{\text{P}} \rightarrow 0} \frac{\mu_{\text{PS}}}{\mu_{\text{SS}}} + \left(\bar{V}_{\text{P}} - \frac{\bar{V}_{\text{S}}}{\nu_{\text{S}} y_{\text{S}}} \right) C_{\text{S}} \quad (6.45)$$

To shorten notation, it is convenient to introduce the following quantities:

$$C_{\text{SP}} \equiv \lim_{C_{\text{P}} \rightarrow 0} \frac{\mu_{\text{SP}}}{\mu_{\text{SS}}} = - \lim_{C_{\text{P}} \rightarrow 0} \left(\frac{\partial C_{\text{S}}}{\partial C_{\text{P}}} \right)_{\mu_{\text{S}}} \quad (6.46)$$

$$\gamma \equiv \lim_{C_{\text{P}} \rightarrow 0} \frac{\mu_{\text{PS}}}{\mu_{\text{SS}}} \quad (6.47)$$

$$\tilde{V}_P \equiv \bar{V}_P - (\bar{V}_S / \nu_S y_S) \quad (6.48)$$

where C_{SP} characterized equilibrium salt distribution, γ is a thermodynamic parameter that will be further discussed below and in section 6.2 and $\tilde{V}_P \cong \bar{V}_P$ is a good approximation for colloidal particles because $\bar{V}_P \gg \bar{V}_S$. This allows us to rewrite eq. (6.45) in the following compact form:

$$C_{SP} = (1 - \bar{V}_S C_S) \gamma + \tilde{V}_P C_S \quad (6.49)$$

Equation (6.49) is an expression that allows us to describe equilibrium salt distribution as the summation of two components that are essentially related to the particle partial molar volume and the thermodynamic parameter, γ .

In the remaining part of this section, we show that also γ is a salt partition coefficient. If we introduce salt partitioning by employing m_P and m_S instead of C_P and C_S , we can use thermodynamic relations to show that:

$$\left(\frac{\partial m_S}{\partial m_P} \right)_{\mu_S} = - \frac{(\partial \mu_S / m_P)_{m_S}}{(\partial \mu_S / m_S)_{m_P}} = - \frac{(\partial \mu_P / m_S)_{m_P}}{(\partial \mu_S / m_S)_{m_P}} = - \frac{(1 - \bar{V}_S C_S) \mu_{PS} - \bar{V}_S C_P \mu_{PP}}{(1 - \bar{V}_S C_S) \mu_{SS} - \bar{V}_S C_P \mu_{SP}} \quad (6.50)$$

In the limit of $C_P \rightarrow 0$, Eq (6.50) can be rearranged in the following way:

$$\gamma = - \lim_{C_P \rightarrow 0} \left(\frac{\partial m_S}{\partial m_P} \right)_{\mu_S} + y_S \frac{\bar{V}_S C_S}{1 - \bar{V}_S C_S} \quad (6.51)$$

The second term on the right side of eq. (6.51) is approximately equal to $\bar{V}_S C_S$ while the first term is of the order of $\bar{V}_P C_S$. Thus, the second term is relatively small because the molar volume

of small inorganic salts is small compared to that of colloidal particles. This implies that we can approximately write:

$$\gamma \cong -\lim_{c_p \rightarrow 0} \left(\frac{\partial m_s}{\partial m_p} \right)_{\mu_s} \quad (6.52)$$

In section 6.2, we will explain how to interpret values of γ by introducing a two-domain model for particle-salt thermodynamic interactions.

6.2 Two-Domain Model

Within the sophistication of this model, the volumetric contribution of salt is ignored. Thus, the approximation in eq. (6.52) is removed and we directly write:⁹⁴

$$\gamma = -\lim_{c_p \rightarrow 0} \left(\frac{\partial m_s}{\partial m_p} \right)_{\mu_s} \quad (6.53)$$

In the two-domain model, a local domain, represented by the salt-water layer surrounding a globular colloidal particle, is in chemical equilibrium with a bulk domain, representing the salt-water remaining solution. Since the colloidal particle interacts with the salt ions and water molecules in their vicinity, the salt concentration in the local domain is different from that of the unperturbed bulk domain. If the salt concentration in the local domain is higher than in the bulk domain, then the number of salt ions is in excess compared to the bulk-domain composition. On the other hand, salt depletion implies that the number of salt ions are lesser compared to the bulk-domain composition.

The composition of the *local domain* is linked to the composition of the bulk domain by introducing a partitioning coefficient (K^*):

$$K^* = \frac{n'_S / n'_W}{C_S / C_W} \quad (6.54)$$

where n'_S is the number of salt ions divided by ν_S and n'_W is the number of water molecules in the local domain. In eq. (6.54), C_S and C_W are the salt and water concentrations in the bulk domain. If $K^* > 1$, salt preferentially interacts with the colloidal particle (preferential salt binding), while, if $K^* < 1$, water preferentially interacts with the colloidal particle (preferential hydration). The special case where $K^* = 0$ means that salt is fully depleted from particle surface.

We want to express eq. (6.53) as a function of K^* . To achieve our goal, we consider the total number of moles of particles, salt and water in the ternary system: n_P , n_S and n_W , and denote as n_S^* and n_W^* the corresponding number of moles in the binary salt-water bulk domain with:

$$\frac{C_S}{C_W} = \frac{n_S^*}{n_W^*} \quad (6.55)$$

In the limit of $C_P \rightarrow 0$, we can write:

$$\lim_{C_P \rightarrow 0} \left[\frac{\left(\frac{n_S}{n_W} - \frac{n_S^*}{n_W^*} \right)}{\left(\frac{n_P}{n_W} \right)} \right] = \lim_{C_P \rightarrow 0} \left[\frac{\partial(n_S / n_W)}{\partial(n_P / n_W)} \right]_{\mu_S} = \lim_{C_P \rightarrow 0} \left(\frac{\partial m_S}{\partial m_P} \right)_{\mu_S} = \gamma \quad (6.56)$$

We use eq. (6.56) to determine the expression of γ in the following way. We first write the following mass balances:

$$n_S = n_S^* + n_P n'_S \quad (6.57)$$

$$n_W = n_W^* + n_P n'_W \quad (6.58)$$

Substituing eq. (6.57) and (6.58) into eq. (6.56):

$$\begin{aligned} \lim_{C_P \rightarrow 0} \left[\frac{\partial(n_S / n_W)}{\partial(n_P / n_W)} \right]_{\mu_S} &= \lim_{C_P \rightarrow 0} \left(\frac{n_S^* + n'_S n_P}{n_W^* + n'_W n_P} - \frac{n_S^*}{n_W^*} \right) \frac{n_W^* + n'_W n_P}{n_P} = \\ &= \lim_{C_P \rightarrow 0} \left(\frac{n_S^* + n'_S n_P}{n_P} - \frac{n_W^* + n'_W n_P}{n_M} \frac{n_S^*}{n_W^*} \right) = \\ &= \lim_{C_P \rightarrow 0} \left(\frac{n_S^*}{n_P} + n'_S - \frac{n_W^*}{n_P} \frac{n_S^*}{n_W^*} - n'_W \frac{n_S^*}{n_W^*} \right) = \\ &= n'_S - n'_W \frac{n_S^*}{n_W^*} = n'_W (K^* - 1) \frac{C_S}{C_W} \end{aligned} \quad (6.59)$$

We finally obtain:

$$\gamma = - n'_W (K^* - 1) \frac{C_S}{C_W} \quad (6.60)$$

Since n'_W and K^* cannot be separately determined, it is convenient to introduce the *water thermodynamic excess* as $N_W \equiv n'_W (1 - K^*)$ and write:

$$\gamma = N_W \frac{C_S}{C_W} \quad (6.61)$$

The parameter N_W describes the number of water molecules in excess near a colloidal particle compared to bulk.^{95, 96} If salt is fully depleted in the local domain ($K^* = 0$), then $N_W = n'_W$ becomes the number of water molecules in the local domain. If the local domain has the same composition as the bulk domain (no preferential interaction, $K^* = 1$), then $N_W = 0$. Finally, if salt preferentially binds to the colloidal particle ($K^* > 1$), then $N_W < 0$ means that

there is a depletion of water molecules near the colloidal particle. The ratio C_s / C_w in the limit where $C_p \rightarrow 0$ is: $(\bar{V}_w C_s) / (1 - \bar{V}_s C_s)$. If we ignore the volumetric contribution of salt, we can write $1 - \bar{V}_s C_s \cong 1$ and $C_w \cong 1 / \bar{V}_w$. This leads to:

$$\gamma = N_w \bar{V}_w C_s \quad (6.62)$$

showing that γ is approximately directly proportional to C_s . Similarly, we can deduce from eq. (6.49), see Section 6.2, that $C_{sp} \approx \gamma + \bar{V}_p C_s = (\bar{V}_p + N_w \bar{V}_w) C_s$ is also approximately directly proportional to C_s . These two thermodynamic parameters can be experimentally obtained from multicomponent-diffusion measurements at different salt concentrations. In Chapter 8, we link this thermodynamic relations γ and C_{sp} shown in this chapter to diffusiophoresis and multicomponent diffusion in general.

6.3 Spinodal Condition for Colloidal Solutions

The thermodynamic stability of surfactant aqueous solution decreases in the presence of salts with salting-out properties. This ultimately leads to phase separation (cloud point) even in dilute solution of colloidal particles. Thus, it is important to examine the thermodynamic properties of a Particle(P)-Salt(S)-Water(W) system in the context of liquid-liquid phase separation (LLPS). In the isothermal phase diagram, LLPS is described by the binodal curve: $C_p(C_s)$, which separates the one-phase domain (low C_s) from the two-phase domain (high C_s). As we further increase salt concentration within the two-phase domain, phase separation from metastable (nucleation driven) becomes unstable (spinodal decomposition). The boundary separating metastability and instability domains is known as spinodal boundary.^{97, 98}

Compared to binodal boundary, the spinodal boundary is more straightforwardly connected to chemical-potential derivatives and diffusion.

According to thermodynamics, the determinant of the 2×2 matrix of chemical-potential derivatives, $\mu_{ij} \equiv (\partial \mu_i / \partial C_j)_{C_k, k \neq j}$ (with $i, j = P, S$ and $k \neq j$), must be zero on the spinodal curve.

$$\begin{vmatrix} \mu_{PP} & \mu_{PS} \\ \mu_{SP} & \mu_{SS} \end{vmatrix} = 0 \quad (6.63)$$

For colloidal particles, one may equivalently examine thermodynamic behavior using osmotic compressibility instead of chemical-potential derivatives. The expression of osmotic compressibility is:

$$\left(\frac{\partial C_P}{\partial \Pi} \right)_{\mu_S} = \frac{y_P}{RT} \quad (6.64)$$

where Π is the osmotic pressure due to colloidal particles (not salt) and y_P is a non-ideality thermodynamic factor, with $y_P = 1$ in the limit of $C_P \rightarrow 0$ at any salt chemical potential, μ_S .

We will now show that $y_P = 0$ on the spinodal curve. If we use the Gibbs-Duhem equation,

$-d\Pi + C_P d\mu_P + C_S d\mu_S = 0$, we obtain:

$$y_P = \frac{C_P}{RT} \left(\frac{\partial \mu_P}{\partial C_P} \right)_{\mu_S} = \frac{\phi_P}{RT} \left(\frac{\partial \mu_P}{\partial \phi_P} \right)_{\mu_S} \quad (6.65)$$

where $\phi_P = \bar{V}_P C_P$ is particle volume fraction. The chemical-potential derivative $(\partial \mu_P / \partial C_P)_{\mu_S}$

can be rewritten as:

$$\left(\frac{\partial \mu_P}{\partial C_P} \right)_{\mu_S} = \mu_{PP} + \mu_{PS} \left(\frac{\partial C_S}{\partial C_P} \right)_{\mu_S} = \mu_{PP} - \mu_{PS} \frac{\mu_{SP}}{\mu_{SS}} = \frac{1}{\mu_{SS}} \begin{vmatrix} \mu_{PP} & \mu_{PS} \\ \mu_{SP} & \mu_{SS} \end{vmatrix} \quad (6.66)$$

If we replace eq. (6.66) in eq. (6.65), we obtain:

$$\begin{vmatrix} \mu_{PP} & \mu_{PS} \\ \mu_{SP} & \mu_{SS} \end{vmatrix} = \mu_{SS} \frac{RT}{C_P} y_P \quad (6.67)$$

For a dilute solution of colloidal particles $\mu_{SS} \approx RT v_s y_s / C_s$ (see (6.13)) is different from zero.

This implies that eq. (6.63) is equivalent to $y_p = 0$. In chapter 8 section 8.5, we will relate the spinodal condition to particle diffusion.

CHAPTER 7

DIFFUSION IN BINARY SYSTEMS BACKGROUND

7.1 Brownian Motion

The simplest case of diffusion in liquids is represented by diffusion of one colloidal particle through a solvent treated as a continuum. In the absence of external forces, the velocity of a colloidal particle is continually changing direction, as a result of random collisions with solvent molecules.⁹⁹ Consequently, the colloidal particle pursues a complicated and irregular zig-zag path, described by the random trajectory specified by position, $\vec{r}(t)$, where t is time. When the particles are large enough compared to solvent molecules, this random motion is referred to as *Brownian motion*, after the botanist who first observed this phenomenon with pollen grains suspended in water.¹⁰⁰

The mean Brownian displacement, $\langle |\vec{r}|^2 \rangle$, of a particle from its original position after a time t allows us to introduce the Brownian mobility or tracer diffusion coefficient of a particle from a microscopic point of view. Specifically, the tracer diffusion coefficient of a colloidal particle, D_p^0 ($\text{m}^2 \cdot \text{s}^{-1}$), may be defined as $D_p^0 \equiv (1/6) \lim_{t \rightarrow \infty} (\langle |\vec{r}|^2 \rangle / t)$.

From a macroscopic point of view, diffusion describes the tendency for particles to migrate from a region of high concentration to a region of lower concentration and this is a direct result of particle Brownian motion. Diffusion is one of the transport phenomena that describes the net motion of colloidal particles under the influence of a macroscopic force, which we denoted here as the driving force, \vec{F}_d . In vacuum, a particle subjected to a force will accelerate, while a frictional force \vec{F}_f , will oppose the driving force in the presence of

surrounding media. In this case, a transport process such as diffusion can be thought to occur in a quasi-stationary regime in which the thermodynamic driving force equals the opposing frictional force. Since the frictional force is directly proportional to the particle drift speed, \bar{v}_p , we can write:

$$\vec{F}_f = f \bar{v}_p \quad (7.1)$$

where f ($\text{kg} \cdot \text{s}^{-1}$) is a proportionality constant called the frictional coefficient.

The mechanical equilibrium condition, $\vec{F}_d = \vec{F}_f$, implies that an ensemble of colloidal particles will move at a constant overall speed, known as drift velocity. From eq. (7.1), the drift velocity is:

$$\bar{v}_p = \frac{\vec{F}_d}{f} \quad (7.2)$$

According to Stokes' law for a rigid spherical particle (large compared to solvent molecules), the frictional coefficient is related to the particle hydrodynamic radius and the viscosity of the surrounding medium by:

$$f = 6\pi\eta R_p \quad (7.3)$$

where η is the fluid viscosity (e.g., viscosity of binary salt-water solution in the case of micelles), treated as a continuum, and R_p is the Stokes hydrodynamic radius of the particle. In general, eq. (7.3) is employed also for non-spherical particles. In this case, there are well-established models to convert Stokes radii extracted from eq. (7.3) into actual particle dimensions.

The macroscopic driving force of diffusion is the gradient of colloidal-particle chemical potential: $\bar{F}_d = \nabla\mu_p$, where $\nabla \equiv (\partial/\partial x + \partial/\partial y + \partial/\partial z)$ and μ_p is the particle chemical potential. In the limiting case of ideal-dilute solutions, we can neglect solute particle-particle interactions and write:

$$m_p = m_p^0 + k_b T \ln(C_p/C^0) \quad (7.4)$$

where C_p is the particle concentration, m_p^0 is the chemical potential in the standard state, k_b is the Boltzmann constant and C^0 is the standard concentration (e.g., 1 M). We can differentiate eq. (7.4) at constant temperature and pressure and obtain:

$$\bar{F}_d = (-\nabla\mu_p) = -k_b T \frac{\nabla C_p}{C_p} \quad (7.5)$$

After substituting eq (7.5) into eq (7.2), we write:

$$\bar{v}_p = -\frac{k_b T}{f} \frac{\nabla C_p}{C_p} \quad (7.6)$$

It can be shown that $D_p^0 \equiv (1/6) \lim_{t \rightarrow \infty} (\langle |\bar{r}|^2 \rangle / t)$ leads to $D_p^0 = k_b T / f$ (Einstein's equation). This implies that:

$$\bar{v}_p = -D_p^0 \frac{\nabla C_p}{C_p} \quad (7.7)$$

Diffusion is often described by employing particle molar flux, $J_p = A^{-1} (dn_p/dt)$ ($\text{mol} \cdot \text{m}^{-2} \text{s}^{-1}$), where A is the cross-section through which particles are diffusing (e.g., in m^2).

After multiplying this expression by dx/dx , we can relate flux to drift velocity, \bar{v}_p , and molar concentration, C_p by:

$$J_p = \frac{1}{A} \frac{dn_p}{dx} \bar{v}_p = C_p \bar{v}_p \quad (7.8)$$

From eqs. (7.6)-(7.8) we can deduce *Fick's first law* as $J_p = -D_p^0 \nabla C_p$. Here, the flux of a solute is parallel and directly proportional to its concentration gradient. Although Fick's first law was deduced for colloidal particles at infinite dilution, this law is known to be valid also at finite concentration of colloidal particles and, in general for binary solute-solvent mixtures, independent of solute particle size. We therefore write:

$$J_p = -D_p \nabla C_p \quad (7.9)$$

Equation (7.9) also applies to binary *salt-water* mixtures (the subscript P is replaced by S in this case; e.g., D_s instead of D_p). Note that D_p is often referred as *mutual* diffusion coefficient. Here, the term “mutual” emphasizes that D_p not only describes solute diffusion in a given direction but also solvent diffusion in the opposite direction. This will be further examined in the following section.

While eq. (7.9) (Fick's first law) is generally valid, $D_p^0 = k_b T / f$ (Einstein's equation) with $f = 6\pi\eta R_p$ (Stokes' law) can be used only for relatively large colloidal particles (e.g., micelles, vesicles, proteins and inorganic nanoparticles) at low concentration. In this case, we can write:

$$D_p^0 = \frac{k_b T}{6\pi\eta R_p} \quad (7.10)$$

Equation (7.10) is important because it allows us to obtain particle size from diffusion coefficients provided that viscosity of particle surrounding medium is known. It also qualitatively shows that the diffusion coefficient of a particle is expected to be significantly smaller than that of a cosolute with relatively low molecular weight. In our case, the diffusion coefficient of micelles is significantly smaller than that of inorganic salts.

7.2 Reference Frames

The drift velocity of solute particles can be defined only if a given reference frame is introduced. Hence, the flux, J_p , must be described with respect to a reference frame. This implies that diffusion coefficient in eq (7.9) also depends on the choice of reference frame. Since different reference frames lead to different values of diffusion coefficients, it is convenient to use reference frames that may be readily connected to experiments and theory. Hence, the volume-fixed (subscript V) and solvent-fixed (subscript W) reference frames are typically introduced.^{77, 101}

In the *volume-fixed reference frame*, it is assumed that the fluxes of the components are defined with respect to center of volume of the system. For a binary system, this corresponds to the condition:

$$\bar{V}_W(J_W)_V + \bar{V}_P(J_P)_V = 0 \quad (7.11)$$

The volume-fixed reference frame diffusion coefficients are experimentally determined because the center of system volume corresponds to the fixed center of the cell in which diffusion occurs. It is important to note that this correspondence is based on the (excellent) approximation that the total volume of the system does not change during diffusion.

We will now show that the solvent diffusion coefficient is equal to that of solute in the volume-fixed reference frame. If we insert the flux expression given by eq. (7.9) in eq. (7.11), we can write:

$$\bar{V}_W(D_W)_V \nabla C_W + \bar{V}_P(D_P)_V \nabla C_P = 0 \quad (7.12)$$

To relate C_W with C_P we know that:

$$\bar{V}_W C_W + \bar{V}_P C_P = 1 \quad (7.13)$$

Since $C_W d\bar{V}_W + C_P d\bar{V}_P = 0$, from Gibbs-Duhem equation, eq. (7.13) gives: $\bar{V}_W \nabla C_W = -\bar{V}_P \nabla C_P$

. Thus eq. (7.12) finally yields:

$$(D_W)_V = (D_P)_V \quad (7.14)$$

Equation (7.14) implies that displacement of solute particle must be compensated by an equivalent displacement of solvent molecules: i.e., mutual diffusion.

In the *solvent-fixed frame*, the average drift velocity of *solvent* molecules is set to be zero. Thus, the flux of the solvent is zero: $(J_W)_W = 0$. The solvent-fixed reference-frame diffusion coefficients are more directly related to thermodynamics driving forces. Hence, it is convenient to relate the solvent-fixed reference frame with the experimentally accessible volume-fixed reference frame as shown below.

The velocity of the solute in the solvent-fixed frame is related to the velocities of the solvent and the particle in the volume-fixed frame by:

$$(\vec{v}_P)_W = (\vec{v}_P)_V - (\vec{v}_W)_V \quad (7.15)$$

If we multiply eq. (7.15) by C_P , we obtain:

$$C_p(\vec{v}_p)_w = C_p(\vec{v}_p)_v - C_p(\vec{v}_w)_v \quad (7.16)$$

Based on eq (7.8), eq (7.16) can be rewritten in the following way:

$$(J_p)_w = (J_p)_v - \frac{C_p}{C_w}(J_w)_v \quad (7.17)$$

Using eqs. (7.9), (7.13), and (7.16) we obtain:

$$(D_p)_w \nabla C_p = (D_p)_v \left(\nabla C_p - \frac{C_p}{C_w} \nabla C_w \right) = \frac{(D_p)_v}{1 - C_p V_p} \nabla C_p \quad (7.18)$$

We, therefore, conclude that:

$$(D_p)_w = \frac{(D_p)_v}{1 - C_p V_p} \quad (7.19)$$

From eq. (7.19), we can see that in the limit of ideal-diluted solution $(D_p)_w = (D_p)_v = D_p^0$. In general, we have: $(D_p)_w \geq (D_p)_v$ because diffusion of solute particles in the solvent-fixed frame is measured with respect solvent diffusion occurring in the *opposite* direction. In the following chapter we are going to extend the diffusion theory to the case of ternary systems which will then allow us to introduce diffusiophoresis.

CHAPTER 8

DIFFUSION AND DIFFUSIOPHORESIS IN TERNARY SYSTEMS BACKGROUND

8.1 Diffusion and Fick's First Law in Ternary Systems

Fick's first law can be extended to ternary systems as follows:

$$-J_p = D_{pp}\nabla C_p + D_{ps}\nabla C_s \quad (8.1)$$

$$-J_s = D_{sp}\nabla C_p + D_{ss}\nabla C_s \quad (8.2)$$

where C_p and C_s are molar concentrations, and J_p and J_s are molar fluxes of the colloidal particle and salt, respectively. The four D_{ij} (with $i,j = P, S$) are the ternary diffusion coefficients. To specify volume-fixed or solvent-fixed reference frames, we shall append the subscripts V or W , respectively, as shown in the previous section.

The diffusion coefficients, D_{pp} and D_{ss} , describe the flux of colloidal particles and salt, due to their own concentration gradients. These two coefficients are expected to be closely related to the corresponding binary diffusion coefficients, D_p and D_s , associated with the binary colloid-water and salt-water systems, respectively. In the limit of $C_p \rightarrow 0$, we have: $D_{pp} \rightarrow D_p^0(C_s)$ and $(D_{sp})_W \rightarrow D_s(C_s)$. The coefficients, D_{ps} and D_{sp} , are denoted as cross-diffusion coefficients, with D_{ps} describing the flux of colloidal particle due to the concentration gradient of the salt, and D_{sp} describing the flux of salt due to the concentration gradient of the colloidal particle. In the limit of $C_p \rightarrow 0$, $D_{sp} = 0$ because $J_s = 0$.

For ternary systems, the solvent-fixed diffusion coefficients are related to the corresponding volume-fixed diffusion coefficients as in the case of binary systems. For D_{PP} , we start with a velocity equation similar to eq. (7.16):

$$(\bar{v}_P)_W = (\bar{v}_P)_V - (\bar{v}_W)_V \quad (8.3)$$

If we multiply eq (8.3) by C_P , we obtain:

$$C_P(\bar{v}_P)_W = C_P(\bar{v}_P)_V - C_P(\bar{v}_W)_V \quad (8.4)$$

Equation (8.4) can be then rewritten as:

$$(J_P)_W = (J_P)_V - \frac{C_P}{C_W}(J_W)_V \quad (8.5)$$

Substituting $(J_W)_V$ by $-(J_W)_V(\bar{V}_P/\bar{V}_W) - (J_S)_V(\bar{V}_S/\bar{V}_W)$, $(J_P)_W$ by eq (8.5), and $(J_P)_V$ by $(D_{PP})_V \nabla C_P + (D_{PS})_V \nabla C_S$ in eq (8.5) and solving for $(D_{PP})_W$ we obtain:

$$(D_{PP})_W = (D_{PP})_V + \frac{C_P}{C_W \bar{V}_W} [\bar{V}_W (D_{PP})_V + \bar{V}_S (D_{SP})_V] \quad (8.6)$$

Since $C_W \bar{V}_W = 1 - C_S \bar{V}_S - C_P \bar{V}_P$, we can finally write:

$$(D_{PP})_W = (D_{PP})_V + [C_P / (1 - C_P \bar{V}_P - C_S \bar{V}_S)] [\bar{V}_P (D_{PP})_V + \bar{V}_S (D_{SP})_V] \quad (8.7)$$

Following a procedure similar to that shown for deriving (8.7), we can obtain the following other three relations:

$$(D_{PS})_W = (D_{PS})_V + [C_P / (1 - C_P \bar{V}_P - C_S \bar{V}_S)] [\bar{V}_P (D_{PS})_V + \bar{V}_S (D_{SS})_V] \quad (8.8)$$

$$(D_{SP})_W = (D_{SP})_V + [C_S / (1 - C_P \bar{V}_P - C_S \bar{V}_S)] [\bar{V}_P (D_{PP})_V + \bar{V}_S (D_{SP})_V] \quad (8.9)$$

$$(D_{SS})_W = (D_{SS})_V + [C_S / (1 - C_P \bar{V}_P - C_S \bar{V}_S)] [\bar{V}_P (D_{PS})_V + \bar{V}_S (D_{SS})_V] \quad (8.10)$$

In our case, the solvent-fixed diffusion coefficients, which are more directly connected to chemical-potential derivatives, are calculated from experimentally accessible volume-fixed diffusion coefficients using (eqs (8.7)-(8.10)). The connection between solvent-fixed diffusion coefficients and chemical-potential derivatives will be examined the following section. To alleviate notation, the subscript W will be omitted.

8.2 Non-Equilibrium Thermodynamics

In general, non-equilibrium thermodynamics provides the theoretical basis for understanding diffusion transport of multicomponent systems.¹⁰² Here, we will see that ternary diffusion coefficients (in the solvent-fixed reference frame) are linear combinations of fundamental thermodynamic (chemical-potential derivatives) and transport (Onsager transport coefficients) parameters.^{77, 103} For binary colloid-water or salt-water systems, we can write:

$$-(J_P)_W = L_{PP} \nabla \mu_P \quad (8.11)$$

$$-(J_S)_W = L_{SS} \nabla \mu_S \quad (8.12)$$

where the L_{PP} and L_{SS} terms are fundamental transport parameters known as Onsager transport coefficients (in the solvent-fixed reference frame).^{104, 105} Note that eqs. (8.11) and (8.12) are consistent with Fick's first Law with the difference that the driving force for diffusion, the chemical potential gradient, is explicitly employed. Combining eq. (8.6) and eqs. (8.11)-(8.12), we obtain:

$$(D_P)_W = L_{PP}\mu_{PP} \quad (8.13)$$

$$(D_S)_W = L_{SS}\mu_{SS} \quad (8.14)$$

Equations (8.11)-(8.12) can be extended to ternary systems in the following way:

$$-(J_P)_W = L_{PP}\nabla\mu_P + L_{PS}\nabla\mu_S \quad (8.15)$$

$$-(J_S)_W = L_{SP}\nabla\mu_P + L_{SS}\nabla\mu_S \quad (8.16)$$

where the four L_{ij} (with $i, j = P, S$) terms represent the Onsager transports coefficients for ternary systems. It is important to note that $L_{PS} = L_{SP}$; this is known as the Onsager reciprocal relation (ORR) or, equivalently, as the third law of non-equilibrium thermodynamics. If we combine eqs (8.13)-(8.14) with eqs (8.15)-(8.16), we obtain:

$$(D_{PP})_W = L_{PP}\mu_{PP} + L_{PS}\mu_{SP} \quad (8.17)$$

$$(D_{PS})_W = L_{PP}\mu_{PS} + L_{PS}\mu_{SS} \quad (8.18)$$

$$(D_{SP})_W = L_{SP}\mu_{PP} + L_{SS}\mu_{SP} \quad (8.19)$$

$$(D_{SS})_W = L_{SP}\mu_{PS} + L_{SS}\mu_{SS} \quad (8.20)$$

These equations show that our four diffusion coefficients are linear combinations of chemical-potential derivatives. In the next section, we are going to describe how the cross-diffusion coefficients, $(D_{PS})_W$, is related to diffusiophoresis coefficient of a colloidal particle. The other cross-diffusion coefficient, $(D_{SP})_W$, is related to another phenomenon known as salt osmotic diffusion. Salt osmotic diffusion will be introduced in subsection 8.3.2.

8.3 Diffusiophoresis and Salt Osmotic Diffusion

In this section, we examine particle diffusiophoresis and salt osmotic diffusion by employing the formalism of non-equilibrium thermodynamics.

8.3.1 Diffusiophoresis coefficient, \hat{D}_{PS} .

For a diluted solution, the particle drift velocity (in the solvent-fixed frame) is given by the following linear law: ^{5, 106, 107}

$$\bar{v}_p = -D_p^0 \left(\nabla \ln C_p + \hat{D}_{PS} \frac{\nabla \mu_s}{RT} \right) \quad (8.21)$$

The term $\nabla \ln C_p$ describes the Brownian restoring entropic force acting against diffusiophoresis. The reduced diffusiophoresis coefficient, \hat{D}_{PS} , which characterizes the relative magnitude of diffusiophoresis compared to particle Brownian mobility (D_p^0), is a proportionality constant linking the thermodynamic driving force of diffusiophoresis, $\nabla \mu_s$, with resulting drift velocity, \bar{v}_p . Note that $\nabla \mu_s / RT = v_{sy} / C_s$ (see eq. (6.44)).^{6, 108} This description of diffusiophoresis is analogous to that of electrophoresis or sedimentation where an external electrical- or gravitational- potential gradient drives the motion of a colloidal particle due to its electric charge or mass.

We are now going to show how \hat{D}_{PS} is directly related to the thermodynamic parameter, g , introduced in the thermodynamic section 6.1, by using eq. (8.15). In this equation, there are two chemical-potential gradients, one for the salt and another one for the colloidal particle. We need to deduce the mathematical relation that allows us to substitute $\nabla \mu_p$ in eq. (8.15) with

$\nabla \ln C_p$. To achieve our goal, we differentiate $\nabla \mu_p(C_p, \mu_s)$ as shown below:

$$\nabla \mu_p(C_p, \mu_s) = \left(\frac{\partial \mu_p}{\partial C_p} \right)_{\mu_s} \nabla C_p + \left(\frac{\partial \mu_p}{\partial \mu_s} \right)_{C_p} \nabla \mu_s = \mu_{pp} \nabla C_p + \left(\frac{\partial \mu_p}{\partial \mu_s} \right)_{C_p} \nabla \mu_s \quad (8.22)$$

The term $(\partial \mu_p / \partial \mu_s)_{C_p}$ in eq (8.22) can be expressed as:

$$\left(\frac{\partial \mu_p}{\partial \mu_s} \right)_{C_p} = \frac{(\partial \mu_p / \partial C_s)_{C_p}}{(\partial \mu_s / \partial C_s)_{C_p}} = \frac{\mu_{pp}}{\mu_{ss}} \quad (8.23)$$

where $\mu_{ij} \equiv (\partial \mu_i / \partial C_j)_{C_i}$. In the limit where $C_p \rightarrow 0$, $\mu_{ps} = RT / C_p$ and $\gamma = \mu_{ps} / \mu_{ss}$ (see thermodynamic section 6.1). We can then consider this limits to rewrite eq (8.22) in the following way:

$$\nabla \mu_p = RT \nabla \ln C_p + \gamma \nabla \mu_s \quad (8.24)$$

After taking L_{pp} as a common factor in eq. (8.15), and considering that the particle drift velocity is $\vec{v}_p = J_p / C_p$, we obtain:

$$\vec{v}_p = -\frac{L_{pp}}{C_p} \left(\nabla \mu_p + \frac{L_{ps}}{L_{pp}} \nabla \mu_s \right) \quad (8.25)$$

Note that $\lim_{C_p \rightarrow 0} (L_{pp} / C_p) = D_p^0 / RT$ in eq. (8.25). If we then substitute eq. (8.24) into eq. (8.25) and define: $\lambda = -\lim_{C_p \rightarrow 0} (L_{ps} / L_{pp})$, we obtain:

$$\vec{v}_p = -D_p^0 \left(\nabla \ln C_p + (\gamma - \lambda) \frac{\nabla \mu_s}{RT} \right) \quad (8.26)$$

Comparison of eq. (8.21) with eq. (8.26) allows us to realize that:

$$\hat{D}_{ps} = \gamma - \lambda \quad (8.27)$$

Equation (8.27) shows that the diffusiophoresis coefficient is a difference between a thermodynamic parameter (γ) and transport parameter (λ).

We will now describe how we obtain the diffusiophoresis coefficient, \hat{D}_{PS} , from experimental multicomponent diffusion coefficients. If we take eq. (8.18) for the cross-diffusion coefficient D_{PS} and divided it by $L_{PP}\mu_{SS}$ we have:

$$\lim_{C_p \rightarrow 0} \frac{(D_{PS})_W}{L_{PP}\mu_{SS}} = \frac{\mu_{PS}}{\mu_{SS}} + \frac{L_{PS}}{L_{PP}} = \gamma - \lambda \quad (8.28)$$

From eq. (8.28) we can see how the diffusiophoresis coefficient, \hat{D}_{PS} , is directly related to the experimentally obtained cross-diffusion coefficient D_{PS} . Furthermore, in the limit of $C_p \rightarrow 0$, we have:

$$L_{PP}\mu_{SS} = \frac{C_p D_p^0}{RT} \frac{RT}{C_s} y_s v_s \quad (8.29)$$

Thus, the diffusiophoresis coefficient can be expressed as:

$$\hat{D}_{PS} \equiv \lim_{C_p \rightarrow 0} \frac{(D_{PS})_W}{C_p} \cdot \frac{C_s}{v_s y_s D_p^0} \quad (8.30)$$

where D_p^0 is the previously mentioned Brownian diffusion coefficient of the colloidal particle (tracer diffusion coefficient), in an aqueous solution at infinite dilution. The term y_s is a thermodynamic factor of the binary salt-water system (see eq. (6.44)). Both D_p^0 and y_s are a function of salt concentration, C_s , at a constant temperature. Values $y_s(C_s)$ are available through the literature. Values $D_p^0(C_s)$ can be obtained using dynamic light scattering (DLS, see chapter 11, section 11.2).^{109, 110}

The D_{PS} value, in eq (8.30), corresponds to the solvent-fixed reference frame. Because we experimentally measure $(D_{PS})_V$ (see Chapter 7 Section 7.2) , it is possible to calculate $(D_{PS})_W$ in the solvent-fixed frame diffusion coefficient through the following relation (see also eq. (7.19)):

$$\frac{(D_{PS})_W}{C_P} = \left(\frac{(D_{PS})_V}{C_P} + \frac{\bar{V}_S (D_{SS})_V}{(1 - C_S \bar{V}_S)} \right) = \left(\frac{(D_{PS})_V}{C_P} + \bar{V}_S (D_S)_W \right) \quad (8.31)$$

We can rewrite eq (8.30) as:

$$\hat{D}_{PS} = \left(\frac{1}{D_P^0} \lim_{C_P \rightarrow 0} \frac{(D_{PS})_V}{C_P} + \frac{\bar{V}_S}{\alpha} \right) \cdot \frac{C_S}{v_S y_S} \quad (8.32)$$

where the \bar{V}_S/α term represents a small positive correction accounting for the change from volume-fixed to the solvent-fixed reference frame, with \bar{V}_S being the salt partial molar volume, $\alpha \equiv D_P^0 / D_S$ is a particle-to-salt diffusion ratio.

8.3.2 Osmotic Diffusion Coefficient, \hat{D}_{SF} .

In this section, we are going to introduce another cross-diffusion phenomenon which is more directly related to particle-salt thermodynamic interactions. To introduce this coefficient, we begin by considering an *equilibrium dialysis system*. In equilibrium dialysis (see Figure 15), we have a ternary particle-salt-water solution inside a first compartment (left) in chemical equilibrium with a salt reservoir in a second compartment (right). The compartments are separated by a membrane permeable to salt and water only. If the salt concentration is initially the same on both sides (Figure 15A), the existing concentration gradient of colloidal particles at the interface will introduce a corresponding gradient of salt

chemical potential. This, in turn, induces salt diffusion (*salt osmotic diffusion*) between the two compartments until the chemical potential of salt is the same in both compartments (Figure 15B).

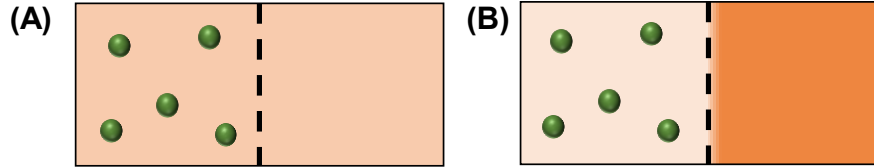


Figure 15. Equilibrium dialysis setup with two compartments separated by a semipermeable membrane (dashed line). Colloidal particles (green spheres) are present in the left compartment only. (A) Initial salt concentration is equal in both compartments (uniform orange color). (B) The difference in particle concentration between the two compartments leads to salt osmotic diffusion from left to right (difference in color intensity between the two compartments).

At equilibrium, the net flux of salt is zero, $(J_s)_w = 0$, and by applying this to eq. (8.16), we can write:

$$\lim_{C_p \rightarrow 0} \frac{(D_{SP})_w}{(D_{SS})_w} = C_{SP} \quad (8.33)$$

where $C_{SP} \equiv -\lim_{C_p \rightarrow 0} (\partial C_s / \partial C_p)_{\mu_s}$, is a thermodynamic coefficient⁹³ characterizing equilibrium salt distribution along a static particle concentration gradient (see Section 6.1, eq. (6.49)). The subscript m_s describes that salt chemical potential is the same in both compartments. The negative sign in the definition of C_{SP} ensures that this parameter assumes positive values in salting-out conditions. According to eq. (8.33), salt osmotic diffusion provides information on the thermodynamic component of particle diffusiophoresis.^{4, 6, 107}

It is important to note that diffusion can occur in the absence of membranes. Nonetheless, diffusion of relatively large colloidal particles is sufficiently slow in comparison

with that of salt ions that we can expect eq. (8.33) to remain approximately valid even in the absence of membrane. Hence, the salt component virtually reaches equilibrium ($\nabla m_s = 0$) in the presence of an infinitely slower dissipating colloidal particle concentration gradient. It is, therefore, convenient to introduce the salt osmotic diffusion coefficient, \hat{D}_{SP} as:

$$\hat{D}_{SP} \equiv \lim_{C_p \rightarrow 0} \frac{(D_{SP})_W}{(D_{SS})_W} \approx C_{SP} \quad (8.34)$$

We can see in eq. (8.34) how \hat{D}_{SP} is directly related to the cross-diffusion coefficient, D_{SP} . This coefficient is approximately equal to a thermodynamic partitioning coefficient and describes how salt spatially distributes along a slowly dissipating colloidal particle gradient.

Non-equilibrium thermodynamics can be used to rigorously link \hat{D}_{SP} to C_{SP} without neglecting mobility of colloidal particles. If we take eq. (8.19) and divide it by $L_{SS}m_{SS}$, we obtain:

$$\frac{(D_{SP})_W}{L_{SS}\mu_{SS}} = \frac{\mu_{SP}}{\mu_{SS}} + \frac{L_{SM}}{L_{SS}} \frac{\mu_{PP}}{\mu_{SS}} \quad (8.35)$$

Multiplying the second term in eq. (8.35) by L_{PP}/L_{PP} we have:

$$\frac{(D_{SP})_W}{L_{SS}\mu_{SS}} = \frac{\mu_{SP}}{\mu_{SS}} + \frac{L_{SP}}{L_{PP}} \frac{L_{PP}}{L_{SS}} \frac{\mu_{PP}}{\mu_{SS}} \quad (8.36)$$

In the limit of $C_p \rightarrow 0$, we know that $L_{SS}\mu_{SS} = (D_{SS})_W = D_S$ (see eq. (8.14)). Thus,

$(D_{SP})_W / L_{SS}\mu_{SS} = (D_{SP})_W / (D_{SS})_W = \hat{D}_{SP}$. Hence, the left-hand side term in eq. (8.36)

corresponds to \hat{D}_{SP} . The μ_{SP} / μ_{SS} term on the right-hand side represents the partition

coefficient described in the thermodynamic section 6.1 by eq. (7.45). Furthermore, since

$L_{PP}\mu_{PP} / L_{SS}\mu_{SS} = D_P^0 / D_S = \alpha$ and $L_{SP} / L_{PP} = -\lambda$ (defined in section 8.3.1), we can rewrite eq. (8.36) in the following way:

$$\hat{D}_{SP} = C_{SP} - \alpha \lambda = (1 - \bar{V}_S C_S) \gamma + \tilde{V}_P C_S - \alpha \lambda \quad (8.37)$$

where $\tilde{V}_P \equiv \bar{V}_P - (\nu_{sys})^{-1} \bar{V}_S$ (see section 6.1) is experimentally accessible from density measurements. As previously mentioned, $\tilde{V}_P = \bar{V}_P$ is an excellent approximation because the salt molar volume is significantly smaller than \bar{V}_P . In eq. (8.37), the term, α / γ , is small compared to C_{SP} , consistent with eq. (8.34).

According to eqs. (8.27) and (8.37), measurements of \hat{D}_{SP} and \hat{D}_{PS} as a function of salt concentration allow us to extract the thermodynamic parameter $g(C_S)$ and the transport parameter $\gamma(C_S)$. Since \hat{D}_{SP} becomes a thermodynamic quantity in the hypothetical limit in which the micelle-to-salt diffusion ratio, α , is zero, the determination of $\hat{D}_{SP}(C_S)$ (salt osmotic diffusion) is a prerequisite for understanding the thermodynamic component of particle diffusiophoresis $\hat{D}_{PS}(C_S)$.

As in the diffusiophoresis case, it is possible to calculate $(D_{SP})_w / (D_{SS})_w$ from the experimentally measured volume-fixed frame diffusion coefficient (see eq. (7.19)), through the following relation:

$$\lim_{C_P \rightarrow 0} \frac{(D_{SP})_w}{(D_{SS})_w} = \lim_{C_P \rightarrow 0} \frac{(D_{SP})_V}{(D_{SS})_V} + \frac{C_S \bar{V}_P}{1 - C_S \bar{V}_S} \alpha \quad (8.38)$$

In this way, eq (8.34) becomes:

$$\hat{D}_{\text{SP}} = \lim_{C_p \rightarrow 0} \frac{(D_{\text{SP}})_V}{(D_{\text{SS}})_V} + \frac{C_s \bar{V}_p}{1 - C_s \bar{V}_s} \alpha \quad (8.39)$$

In the next section, we revisit the preferential hydration model in order to obtain an expression for the λ/γ , which is important for understanding particle diffusiophoresis.

8.4 Preferential Hydration Model for Diffusiophoresis

In this section, we revisit the preferential hydration model in order to provide a physical interpretation for the transport parameter, λ . As a starting point, we consider the equilibrium two-domain model, described in the thermodynamic section 6.2, and modify it in order to consider diffusiophoretic transport. In the presence of diffusiophoresis, a slip surface boundary surrounding the particle becomes operational. As shown in Figure 16, it is expected that the local domain of the particle extends beyond its slip surface because only strongly interacting (larger than thermal energy) salt and solvent molecules can be dragged towards the surface. We, therefore, split the local domain into an inner local domain (I) enclosed by the slip surface, and an outer local domain (II), characterizing the fraction of the local domain beyond the slip surface.^{93, 94}

The composition of the inner (I) and outer (II) local domains are linked to the composition of the bulk domain by formally introducing partitioning coefficients, $K^{(\text{I})}$ and $K^{(\text{II})}$, with:

$$K^{(\text{I})} = \frac{n_s^{(\text{I})}/n_w^{(\text{I})}}{C_s/C_w} \quad (8.40)$$

$$K^{(II)} = \frac{n_S^{(II)} / n_W^{(II)}}{C_S / C_W} \quad (8.41)$$

where $n_S^{(I)}$, $n_W^{(I)}$, $n_S^{(II)}$, and $n_W^{(II)}$ are the salt and water number molecules in domains I and II, respectively.

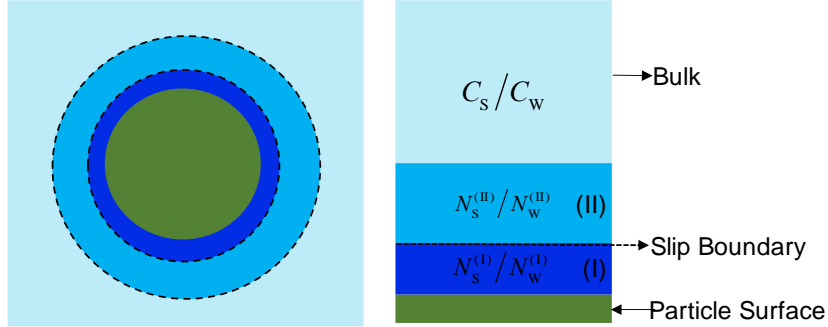


Figure 16. Schematic of spherical colloidal particle surrounded by the remaining solution: local inner domain (I), local outer domain (II), and bulk domain (left). Salt partitioning in the local domain (I) and (II) and the bulk (right).

In general, it is expected that interactions between cosolute and particle are relatively weak in the outer local domain. In other words, we have $K^{(I)} < K^{(II)}$ because salt partitioning is expected to be more pronounced in the inner domain than in the outer domain. Water accumulation in the local domain (preferential hydration) corresponds to $K^{(I)} < K^{(II)} < 1$, with $K^{(I)} = K^{(II)} = 1$ in the absence of salt partitioning, and $K^{(I)} = K^{(II)} = 0$ if salt is completely excluded from the local domain. Starting from ¹⁰⁷:

$$n_S^{\hat{c}} = n_S^{(I)} + n_S^{(II)} \quad (8.42)$$

$$n_W^{\hat{c}} = n_W^{(I)} + n_W^{(II)} \quad (8.43)$$

we can deduce that:

$$\begin{aligned}
\gamma &= \lim_{C_p \rightarrow 0} \left(\frac{n_S^* + (n_S^{(I)} + n_S^{(II)})n_P}{n_W^* + (n_W^{(I)} + n_W^{(II)})n_P} - \frac{n_S^*}{n_W^*} \right) \frac{n_W^* + (n_W^{(I)} + n_W^{(II)})n_P}{n_P} \\
&= \lim_{C_p \rightarrow 0} \left(n_S^{(I)} + n_S^{(II)} \right) - \left(n_W^{(I)} + n_W^{(II)} \right) \frac{n_S^*}{n_W^*} = \lim_{C_p \rightarrow 0} \left(n_S^{(I)} + n_S^{(II)} \right) - \left(n_W^{(I)} + n_W^{(II)} \right) \frac{C_S}{C_W} \\
&= \lim_{C_p \rightarrow 0} \left(n_W^{(I)} K^{(I)} + n_W^{(II)} K^{(II)} \right) \frac{C_S}{C_W} - \left(n_W^{(I)} + n_W^{(II)} \right) \frac{C_S}{C_W} = \left[n_W^{(I)} (1 - K^{(I)}) + n_W^{(II)} (1 - K^{(II)}) \right] \frac{C_S}{C_W}
\end{aligned}$$

and finally write:

$$g = n_W^{(I)} (1 - K^{(I)}) \left[1 + \frac{n_W^{(II)} (1 - K^{(II)})}{n_W^{(I)} (1 - K^{(I)})} \right] \frac{C_S}{C_W} \quad (8.44)$$

Equation (8.44) is a generalization of eq. (6.62) from section 6.1. Note that the sign of g is the same as that of $1 - K^{(I)}$ because the ratio $(1 - K^{(II)}) / (1 - K^{(I)})$ is expected to be positive. For example If $K^{(I)} > 1$ them also $K^{(II)} > 1$ and vice-versa. To derive the corresponding expression of \bar{v}_p , we rewrite eq (8.25) in terms of the particle chemical potential gradient, and the transport coefficient as follows:

$$\bar{v}_p = -D_p^0 \left(\frac{\nabla \mu_p}{RT} - \lambda \frac{\nabla \mu_S}{RT} \right) \quad (8.45)$$

We now remark that the diffusing particle is the complex species $\{P\} \equiv P(W)n_W^{(I)}(S)n_S^{(I)}$, which includes the salt and solvent molecules within the slip surface (inner local domain). This will have an impact on the sign and physical meaning of \bar{v}_p . In this model, we assume that the drift velocity is directly related to the chemical potential of $\{P\}$ and that its dependence on the gradient of salt chemical potential comes entirely from the chemical potential of $\{P\}$. We therefore write:

$$\bar{v}_P = -D_P^0 \frac{\nabla \mu_{\{P\}}}{RT} \quad (8.46)$$

where $\nabla \mu_{\{P\}} = \nabla \mu_P + n_W^{(I)} \nabla \mu_W + n_S^{(I)} \nabla \mu_S$. The Gibbs-Durham equation can be then used to write: $C_W \nabla \mu_W = -C_P \nabla \mu_P - C_S \nabla \mu_S$, which yields: $\nabla \mu_{\{P\}} = \nabla \mu_P + (n_S^{(I)} - n_W^{(I)} C_S / C_W) \nabla \mu_S$ when $C_P \rightarrow 0$. According to eq. (8.40), $n_S^{(I)} - n_W^{(I)} C_S / C_W$ is $-n_W^{(I)} (1 - K^{(I)}) C_S / C_W$. Thus, eq (8.46) can be rewritten in the following way:

$$\bar{v}_P = -D_P \left(\frac{\nabla \mu_P}{RT} - n_W^{(I)} (1 - K^{(I)}) \frac{C_S}{C_W} \frac{\nabla \mu_S}{RT} \right) \quad (8.47)$$

Comparison of eq (8.47) with eq (8.45) allows us to finally write:

$$l = n_W^{(I)} (1 - K^{(I)}) \frac{C_S}{C_W} \quad (8.48)$$

According to eq. (8.48), l is positive in the presence of preferential hydration ($K^{(I)} < 1$). In summary, eqs. (8.44) and (8.48) provide mathematical expressions for g and l . If we then take the ratio between eq (8.48) and (8.44), we have:

$$\frac{l}{g} = \left[1 + \frac{n_W^{(II)} (1 - K^{(II)})}{n_W^{(I)} (1 - K^{(I)})} \right]^{-1} = \left[1 + \frac{N_W^{(II)}}{N_W^{(I)}} \right]^{-1} \quad (8.49)$$

Equation (8.49) shows that l/g is related to the ratio between the water excesses in the inner $N_W^{(I)} = n_W^{(I)} (1 - K^{(I)})$ and outer $N_W^{(II)} = n_W^{(II)} (1 - K^{(II)})$ local domains. While a water excess may be significantly depending on the nature of both salt and colloidal particle, we expect this ratio exhibits a relatively weak dependence on solute chemical nature.

Finally, we can more simply express \hat{D}_{PS} and \hat{D}_{SP} as a function of the total excess water molecules N_{w} , described in the thermodynamic section. Considering that $N_{\text{w}} \approx N_{\text{w}}^{(1)} + N_{\text{w}}^{(II)}$ and $\bar{V}_{\text{w}} = 1/C_{\text{w}}$, where \bar{V}_{w} is the molar volume of water, eqs (8.44) and (8.48) become:

$$g = (N_{\text{w}}^{(1)} + N_{\text{w}}^{(II)}) \frac{C_{\text{s}}}{C_{\text{w}}} = N_{\text{w}} \bar{V}_{\text{w}} C_{\text{s}} \quad (8.50)$$

$$l = N_{\text{w}}^{(1)} \frac{C_{\text{s}}}{C_{\text{w}}} = N_{\text{w}}^{(1)} \bar{V}_{\text{w}} C_{\text{s}} \quad (8.51)$$

$$\frac{\lambda}{\gamma} = \frac{N_{\text{w}}^{(1)}}{N_{\text{w}}} \quad (8.52)$$

Substitution of eqs. (8.50) and (8.51) into eqs. (8.27) and (8.37), allow us to also obtain:

$$\hat{D}_{\text{PS}} = (N_{\text{w}} - N_{\text{w}}^{(1)}) \bar{V}_{\text{w}} C_{\text{s}} \quad (8.53)$$

$$\hat{D}_{\text{SP}} = \left(\frac{\bar{V}_{\text{p}}}{\bar{V}_{\text{w}}} + N_{\text{w}} - \alpha N_{\text{w}}^{(1)} \right) \bar{V}_{\text{w}} C_{\text{s}} \quad (8.54)$$

From eqs. (8.53) and (8.54) we can better appreciate how $\hat{D}_{\text{PS}}(C_{\text{s}})$ and $\hat{D}_{\text{SP}}(C_{\text{s}})$ are related to the excess of water molecules in the inner and outer domains surrounding the colloidal particle (see Figure 16).

8.5 Spinodal Condition and Diffusion

In section 6.3, we examined the thermodynamic behavior of a ternary system on the spinodal curve. We are now going to connect multicomponent diffusion with thermodynamics of spinodal condition.^{97, 111} The 2×2 matrix of multicomponent diffusion coefficients in the

solvent-fixed reference frame, $(D_{ij})_w$, is the product of the symmetric 2×2 matrix of Onsager transport coefficients, L_{ij} , and the 2×2 matrix of chemical-potential derivatives, μ_{ij} :

$$\begin{bmatrix} (D_{PP})_w & (D_{PS})_w \\ (D_{SP})_w & (D_{SS})_w \end{bmatrix} = \begin{bmatrix} L_{PP} & L_{PS} \\ L_{SP} & L_{SS} \end{bmatrix} \begin{bmatrix} \mu_{PP} & \mu_{PS} \\ \mu_{SP} & \mu_{SS} \end{bmatrix} \quad (8.55)$$

The same relation can extend to matrix determinants:

$$\begin{vmatrix} (D_{PP})_w & (D_{PS})_w \\ (D_{SP})_w & (D_{SS})_w \end{vmatrix} = \begin{vmatrix} L_{PP} & L_{PS} \\ L_{SP} & L_{SS} \end{vmatrix} \begin{vmatrix} \mu_{PP} & \mu_{PS} \\ \mu_{SP} & \mu_{SS} \end{vmatrix} \quad (8.56)$$

Since the determinant of the Onsager transport coefficients is not infinitely large, (see eq. (6.63), section 6.3), we deduce that:

$$\begin{vmatrix} (D_{PP})_w & (D_{PS})_w \\ (D_{SP})_w & (D_{SS})_w \end{vmatrix} = 0 \quad (8.57)$$

We can convert the solvent-fixed diffusion coefficients, $(D_{ij})_w$, into the corresponding volume-fixed diffusion coefficients, D_{ij} , (see section 7.2) by using:

$$\det(D) \equiv \begin{bmatrix} (D_{PP})_v & (D_{PS})_v \\ (D_{SP})_v & (D_{SS})_v \end{bmatrix} = \begin{bmatrix} 1 - C_P \bar{V}_P & -C_P \bar{V}_S \\ -C_S \bar{V}_P & 1 - C_S \bar{V}_S \end{bmatrix} \begin{bmatrix} (D_{PP})_w & (D_{PS})_w \\ (D_{SP})_w & (D_{SS})_w \end{bmatrix} \quad (8.58)$$

This implies that:

$$\det(D) = (1 - C_P \bar{V}_P - C_S \bar{V}_S) \begin{vmatrix} (D_{PP})_w & (D_{PS})_w \\ (D_{SP})_w & (D_{SS})_w \end{vmatrix} \quad (8.59)$$

If eq. (8.57) holds, then:

$$\det(D) = \tilde{D}_P \tilde{D}_S = 0 \quad (8.60)$$

where \tilde{D}_p and \tilde{D}_s are the lower and higher eigenvalues of the diffusion-coefficient matrix (in the volume-fixed reference frame). If $(D_{SS})_V > (D_{PP})_V$ and $(D_{PS})_V(D_{SP})_V > 0$, we have:

$$\tilde{D}_p = \frac{(D_{PP})_V + (D_{SS})_V}{2} - \frac{(D_{SS})_V - (D_{PP})_V}{2} \sqrt{1 + \frac{4(D_{PS})_V(D_{SP})_V}{[(D_{SS})_V - (D_{PP})_V]^2}} \quad (8.61)$$

$$\tilde{D}_s = \frac{(D_{PP})_V + (D_{SS})_V}{2} + \frac{(D_{SS})_V - (D_{PP})_V}{2} \sqrt{1 + \frac{4(D_{PS})_V(D_{SP})_V}{[(D_{SS})_V - (D_{PP})_V]^2}} \quad (8.62)$$

Equation (8.60) leads to:

$$\tilde{D}_p = 0 \quad (8.63)$$

$$\tilde{D}_s = (D_{SS})_V + (D_{PP})_V \quad (8.64)$$

Finally, we can also verify that $(D_{SS})_V > (D_{PP})_V$ and $(D_{PS})_V(D_{SP})_V > 0$ imply that $(D_{PP})_V - \tilde{D}_p > 0$. After subtracting eq. (8.61) to $(D_{PP})_V$, we obtain:

$$(D_{PP})_V - \tilde{D}_p = \frac{(D_{SS})_V - (D_{PP})_V}{2} \left(\sqrt{1 + \frac{4(D_{PS})_V(D_{SP})_V}{[(D_{SS})_V - (D_{PP})_V]^2}} - 1 \right) \quad (8.65)$$

In eq.(8.65), we can appreciate that the factor in parenthesis is positive because $(D_{PS})_V(D_{SP})_V > 0$ and $(D_{PP})_V = \tilde{D}_p$ when $(D_{PS})_V(D_{SP})_V = 0$. In Chapter 11 Section 11.4, we will compare the calculated \tilde{D}_p with the experimentally obtained $(D_{PP})_V$.

CHAPTER 9

DIFFUSIOPHORESIS INTRODUCTION

The phenomenon of *diffusiophoresis* has its origins from the work of Derjaguin on a related phenomenon known as *capillary osmosis*. This work theoretically demonstrated that within the diffuse section of an adsorption layer at a solution-solid interface, a phenomenon arises that is similar to that observed in capillary electrophoresis, but with the distinction that these phenomena did *not* depend on the gradient of an external electric potential, but upon the gradient of the *chemical potential* of a solute such as a salt.¹¹² Specifically, a solution is observed to flow inside a capillary not only by imposing an electric potential difference between the two capillary extremities but also by establishing a solute concentration gradient without external electric field. Similarly, a colloidal particle in water not only can migrate in the presence of gradient of electrical potential (electrophoresis) but also in the presence of a gradient of chemical potential of a solute such as a salt (diffusiophoresis). Since the discovery of diffusiophoresis by Derjaguin in 1947, it is not until 50 years later that diffusiophoresis started to gain more relevance in the scientific community with 80% of the research regarding diffusiophoresis being done in the last 20 years, and over 40% of that research been consolidated in the last 5-7 years. The current advances in microfluidic devices have especially contributed to experimentally observing how diffusiophoresis can be used to address a wide variety of real-life problems. A detailed literature review of diffusiophoresis studies in microfluidics is shown in ref 11.

Depending on the surface properties of a colloidal particle (electrically charged or neutral) and the chemical nature of the cosolute (electrolyte or non-electrolyte),

diffusiophoresis in water can be caused by two mechanisms: *electrophoretic* and *preferential hydration*.^{5, 107, 113} In the presence of electrolytes, the electrophoretic mechanism is the dominant cause of diffusiophoresis of *charged* particles at *low* salt concentration. In this case, particle transport is caused by an internal electric field emerging from the difference in mobility between salt counter-ion and co-ion (Figure 17A). On the other hand, the preferential hydration mechanism occurs for both charged and neutral colloidal particles at relatively high concentration of cosolute (electrolyte or non-electrolyte). In this case, particle transport from high to low cosolute concentration is caused by repulsive particle-cosolute interactions in water. Clearly, diffusiophoresis relates to particle hydrophilicity. It is important to remark that preferential hydration mechanism is virtually the sole mechanism responsible for diffusiophoresis of neutral hydrophilic particles (Figure 17B).

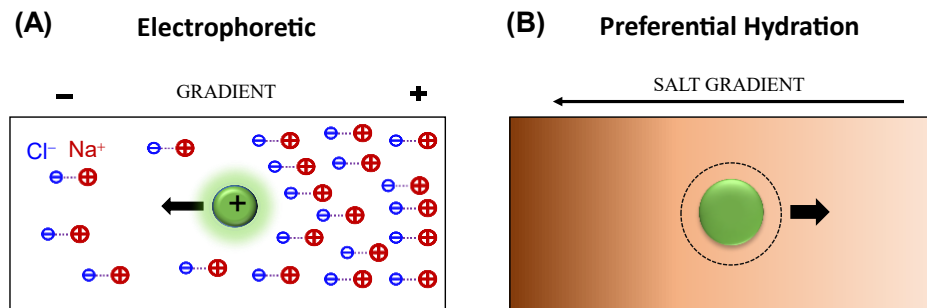


Figure 17. (A) Electrophoretic mechanism: positively charged particle in the presence of NaCl concentration gradient. (B) Preferential hydration mechanism: neutral particle in the presence of a salt concentration gradient.

All diffusiophoresis studies found in the literature reported by other research groups focus on charge particles and no experimental report mentions about non-charged particles.^{4, 5, 7, 13, 114-116} Recent studies regarding diffusiophoresis included applications on conducting droplets for drug delivery,¹¹⁷⁻¹²⁰ transport in and out of dead-end pore geometries for enhanced

oil recovery,^{121, 122} continuous particle separation,^{123, 124} particle self-organization,¹²⁵ maintaining bacteria-free surfaces,¹¹ stratification of drying films,^{126, 127} and self-propelling in active colloids.¹²⁸⁻¹³⁰

As mentioned in Chapter 1, we are interested in the diffusiophoresis of PEG-based nanoparticles (tyloxapol micelles). Previous studies from our research group on free PEG chains represent an important reference point for understanding the diffusiophoresis of our PEG-based neutral colloidal particles. A recent study from our research group has shown that diffusiophoresis of free PEG chains¹³¹ can be induced in the presence of salting-out salts such as sodium sulfate (Na_2SO_4) and also sodium chloride (NaCl),⁶ or osmolytes like Trimethylamine N-oxide (TMAO).¹⁰⁷ In these cases, diffusiophoresis is related to PEG preferential hydration and follows the Hofmeister series, analog to what is observed in the case proteins.^{92, 132}

As discussed in Chapter 8, preferential hydration represents the excess of water molecules near a colloidal particle relative to bulk water concentration. It quantifies macromolecule-cosolute repulsive interactions (salting-out strength), which are ultimately responsible also for aggregation and phase separation. In other words, PEG diffusiophoresis from high to low cosolute concentration is driven by the higher affinity of this macromolecule for water compared to cosolutes, in salting-out conditions.

In Chapter 8 of this dissertation, we have shown that diffusiophoresis can be described in the context of multicomponent diffusion.^{106, 133-135} For example, the transport properties of a ternary PEG-salt-water mixture are characterized by a 2×2 diffusion-coefficient matrix, in which one of the two cross-term diffusion coefficients relates to PEG diffusiophoresis (\hat{D}_{PS})

while the other cross-term characterizes salt diffusion (\hat{D}_{SP}) induced by PEG concentration gradients.⁶ This second transport mechanism, denoted as salt osmotic diffusion, is closely related to PEG-salt thermodynamic interactions and plays a central role in discerning the thermodynamic (γ) and transport (λ) components of salt-induced particle diffusiophoresis.

Diffusiophoresis studies of neutral and globular PEG-based colloidal particles have not been reported. A well-known example of this type of material is represented by the non-ionic micelles formed by polyoxyethylene surfactants, which are regularly employed in the household, chemical, and pharmaceutical industries.¹³⁶ We are therefore interested in determining salt-induced diffusiophoresis of these PEG-based micelles and how it compares to diffusiophoresis of free PEG chains.

An important property of polyoxyethylene surfactants (and PEG) in water is the existence of a lower cosolute temperature (cloud point) in the surfactant-water phase diagram.^{111, 137, 138} The temperature dependence of the self-aggregation of nonionic surfactants is especially important since the head group interaction is essentially totally hydrogen bonding in nature. If a dilute solution of nonionic surfactants is heated, then above a critical temperature (or salt concentration) strong light scattering is observed, and the solution becomes cloudy. This temperature, at which cloudiness occurs, is designated as the *cloud point*, about which the surfactant aqueous solution phase separates. This separation is caused by an increase in micelle-micelle attractive interactions with temperature, and results in the formation of microdroplets (coacervates) at high surfactant concentration. Correspondingly, the mixture becomes visibly turbid⁴⁵. Although this phase transition is typically observed at high temperatures, cloud-point temperature decreases as the concentration of salting-out salts increases.^{139, 140} Hence, it can be observed at room temperature in the presence of a sufficient

amount of salt. Since salt-induced diffusiophoresis requires salting-out conditions, it is also important to examine this transport mechanism in the proximity of the cloud point.

In this investigation, the tyloxapol micelle was chosen as a model PEG-based colloidal particle. Tyloxapol is a nonionic surfactant mostly used in marketed ophthalmic products and as a mucolytic agent for treating pulmonary diseases. It has also been investigated as a nano-carrier for ophthalmic and anti-tubercular drug delivery.¹⁴⁰⁻¹⁴² Tyloxapol is essentially an oligomer of octoxynol 9 (Triton X-100). Its micelles are spherical colloidal particles with a diameter of 7 nm, and their size and shape do not change significantly for concentrations as high as 10% by weight according to cryo-transmission electron microscopy.¹⁴² Moreover, tyloxapol has a critical micellar concentration of $0.0385 \text{ g}\cdot\text{L}^{-1}$ in water at $25 \text{ }^\circ\text{C}$.¹⁴² This value is much lower than that of Triton X-100 and is expected to further decrease in the presence of salts.⁶⁸ This allows us to neglect the presence of free surfactants within our experimental domain. Finally, the cloud point of aqueous tyloxapol (0.5-5% w/w) is $93\text{-}94 \text{ }^\circ\text{C}$ but occurs at room temperature in the presence of a sufficient amount of salting-out salts.¹⁴⁰ In summary, tyloxapol micelles represent a good model for neutral PEG-based globular nanoparticles that are stable in water due to a very low critical micelle concentration value.

Previous work has established that unimer-micelle dynamic equilibration is fast enough to maintain chemical equilibrium along a diffusion path.^{143, 144} This implies that solute fluxes in the presence of their concentration gradients are successfully described by Fick's diffusion laws because the condition of local chemical equilibrium can be applied.^{73, 145, 146}

In the following sections, we experimentally determine the 2×2 diffusion-coefficient matrix for the ternaries tyloxapol- Na_2SO_4 -water and tyloxapol- MgSO_4 -water systems at $25 \text{ }^\circ\text{C}$ at several salt concentrations. These data will allow us to characterize salt-induced

diffusiophoresis of tyloxapol micelles in the presence of two common sulfate salts, known to be strong salting-out agents,⁹² as shown in the Hofmeister series.¹⁴⁷ Our experimental data were described using the preferential-hydration model discussed in Chapter 8. Interestingly, at high salt concentrations, micelle size was found to significantly increase with salt concentration. Since salt-induced aggregation may potentially affect micelle diffusiophoresis, we also developed a model that accounts for the observed increase in micelle size and evaluated contribution of salt-induced aggregation to diffusiophoresis of micelles.

CHAPTER 10

MATERIALS AND METHODS

10.1 Materials

Tyloxapol (BioXtra; 4.5 kg mol/l), sodium sulfate (Research Products International Corp, Na₂SO₄; 142.04 g/mol, purity 99.0%), magnesium sulfate (MgSO₄; 120.40 g/mol, purity 99.0%), and polyethylene glycol (PEG; 20 kg/mol) were purchased from Millipore-Sigma, Fisher Scientific, and Sigma-Aldrich respectively. These materials were used as received without further purification. Deionized water was passed through a four-stage Millipore filter system to provide high-purity water (0.06 μS) for all the experiments.

10.2 Solution Preparation

Binary salt-water stocks solution (Na₂SO₄-water and MgSO₄-water) were prepared due to salt hygroscopicity. Their composition was determined from density measurements and the known density-composition relations (see eq (3.1) for Na₂SO₄):¹⁴⁸

$$d_{\text{MgSO}_4} = 0.997045 + 0.122482(m_s/m^0) - 0.0062708(m_s/m^0)^{1.5} - 0.00342034(m_s/m^0)^2 \quad (10.1)$$

where m_s is salt molality and m^0 is 1 mol/kg.

Tyloxapol-water stock solutions were prepared by weight using a Mettler-Toledo AT400 analytical balance. Slow stirring was used until complete dissolution (3h). Ternary tyloxapol-Na₂SO₄-water, and tyloxapol-MgSO₄-water solutions were prepared by adding precise masses of the respective tyloxapol solution and salt stock solution to flasks and then diluted with pure water to reach the final target concentrations. To determine molar concentrations, solution densities were measured with a Mettler-Paar DMA40 density meter,

thermostated with a well-regulated (± 0.001 °C) water bath. Buoyancy corrections were also applied to weights (see Chapter 3, Section 3.3 for density measurement details).

10.3 Dynamic Light Scattering

Dynamic light scattering (DLS) is a technique that is used to determine the diffusion coefficient of colloidal particles in solution. Diffusion coefficients are obtained by measuring the temporal fluctuations of solution scattered intensity. DLS experiments were performed on a light-scattering apparatus at 25.0 ± 0.1 °C built using the following main components: He-Ne laser (35 mW, 632.8 nm, Coherent Radiation), manual goniometer and thermostat (Photocor Instruments), multi-tau correlator, APD detector and software (PD4042, Precision Detectors).

All solutions were filtered through a 0.02 mm filter (Anotop 10, Whatman) to remove dust and placed in a test tube. All measurements were performed at a scattering angle of 90° . The scattering vector, $q = (4\pi n/\lambda)\sin(q/2)$, was calculated using the laser wavelength of $\lambda = 632.8$ nm and the refractive index of water, $n = 1.3314$. To take into account the effect of salts on the refractive index, small corrections were calculated based on previously reported¹⁴⁸ refractive-index increments. The scattered-intensity correlation functions were analyzed using a regularization algorithm (Precision Deconvolve 32, Precision Detectors).⁶ All scattered-intensity distributions were found to be monomodal and the corresponding z -average diffusion coefficient, D_M , was calculated.¹⁰⁹

10.4 Rayleigh Interferometry

Multicomponent diffusion coefficients were measured at 25.00 ± 0.01 °C with the Gosting diffusimeter operating in the Rayleigh interferometric optical mode.^{79, 149, 150} In brief, a typical diffusion experiment starts by preparing a sharp boundary between two uniform solutions of slightly different solute concentrations located inside a vertical channel with inside

width $a = 2.5$ cm (see Chapter 3, Section 3.4 for more description of the method). Rayleigh fringes shift horizontally as the refractive index inside the diffusion channel changes along the vertical position, x . This gives direct information about the refractive index, $n(x)$. The difference in refractive index, Δn , between the two solutions is obtained from the total number of fringes, J , using $\Delta n = J \lambda / a$. We obtain refractive-index profiles at fifty different values of time, t , during each experiment. The experimental refractive-index profile is then described by the normalized anti-symmetric function $f(y) \equiv 2[n(y) - \bar{n}] / \Delta n$, where \bar{n} is the average refractive index between the two solutions, $y \equiv x \cdot t^{-1/2} / 2$ and $0 \leq f \leq 1$.

Note that the precision of a diffusion coefficient increases with the number of fringes, J . In most of our experiments, differences in concentration between the bottom and top solutions were chosen such that $J \approx 50$.¹⁵⁰ A minimum of two experiments is required for determining the four diffusion coefficients at a given set of mean mass concentrations. These two experiments must have different combinations of solute concentration differences across the diffusion boundary. To verify reproducibility, two other duplicate experiments were performed at each set of mean concentrations (see appendix A for solution preparation data).

The four ternary diffusion coefficients in the volume-fixed reference frame, D_{ij} , were obtained by applying a method of the non-linear least squares.¹⁵¹ Due to tyloxapol molecular-weight polydispersity, a corrective procedure⁸⁰ was applied to our ternary experiments to remove the contribution of polydispersity from the measured refractive-index profiles. This procedure is based on the $n(y)$ profile determined by interfacing a bottom solution with tyloxapol concentration at 1.85 mM with a top solution at 0.15 mM in the absence of salt.

10.5 Cloud Point Measurements

All experiments were performed by incubating samples (≈ 10 g) in a well-regulated ($\pm 0.001^\circ\text{C}$) water bath at 25.0°C for about one hour. An exploratory set of tyloxapol-salt-water mixtures was initially prepared by weight, with tyloxapol and salt concentrations ranging from 0.1 to 2.0 mM and 0.05 to 1.00 M, respectively. By visual inspection, it was determined that the cloud points were within the salt concentration range of 0.60-0.70 M (Na_2SO_4) and 0.85-0.95 M (MgSO_4) at all surfactant concentrations.

To precisely determine the phase boundary, the second set of ternary mixtures was prepared with a salt concentration fixed at 0.70 M (Na_2SO_4) and 0.95 M (MgSO_4) and tyloxapol variable concentrations, again ranging from 0.1 to 2.0 mM. At this salt concentration, all mixtures were observed to be cloudy. Small amounts of water (≈ 0.02 g) were then added in series to each sample. A given water addition was followed by measurement of sample total weight, stirring, and incubation at 25.0°C . The minimum water amount yielding clear homogenous samples by visual inspection was used to identify the composition of the phase boundary. Note that after 24h of incubation Na_2SO_4 solutions remained clear (below the phase separation boundary composition). For MgSO_4 solutions, cloudy samples were observed as low as 0.75 M, after 24h. Hence all experiments are performed in freshly prepared solutions.

Cloudy samples were observed under a light microscope (Axioskop 40, Zeiss) using phase-contrast microscopy. Images were taken using a digital camera (AxioCam MRc, Zeiss) interfaced by a computer with software (Axiovision AC 4.5, Zeiss).

CHAPTER 11

RESULTS AND DISCUSSION

11.1 Isothermal Phase Diagram

As mentioned in Chapter 1, salts affect surfactant properties such as cmc and cloud point. In Part I of this dissertation, we showed the effect of salt on surfactant cmc. In this section, our experimental results on the phase diagram (cloud point) of tyloxapol aqueous solutions in the presence of Na₂SO₄ and MgSO₄ at 25 °C. This data allows us to identify the stability domain of one-phase ternary tyloxapol-salt-water liquid mixtures.

The phase boundary is shown in the (C_S , ϕ_P) phase diagram of Figure 18A, where C_S is salt molar concentration and ϕ_P is surfactant volume fraction. The latter is calculated by multiplying surfactant molar concentration, C_P (based on tyloxapol molar mass of 4.5 kg/mol), by the known^{80, 152} tyloxapol molar volume of $\bar{V}_P=3.98 \text{ dm}^3 \cdot \text{mol}^{-1}$ (also based on the molecular weight of 4.5 kg·mol⁻¹). Our experimental surfactant volume fractions range from 0.02% to 0.7% in this study.

Within our low volume fraction range (0.02% - 0.7%), clouding occurs at $C_S \approx 0.65 \text{ M}$ (Na₂SO₄) and $C_S \approx 0.90 \text{ M}$ (MgSO₄) and weakly depend on ϕ_P (Figure 18A). Our results are consistent with cloud points previously reported by Schott at relatively high tyloxapol concentrations.¹⁴⁰ As shown in Figure 18B, these two salt concentrations approximately correspond to osmolarities of $v_S C_S \approx 1.8 \text{ M}$ (MgSO₄) and $\approx 2.0 \text{ M}$ (Na₂SO₄). Thus, our cloud-point results indicate that MgSO₄ is a salting-out agent that is somewhat stronger than Na₂SO₄ when data are compared with respect to total ion concentrations.

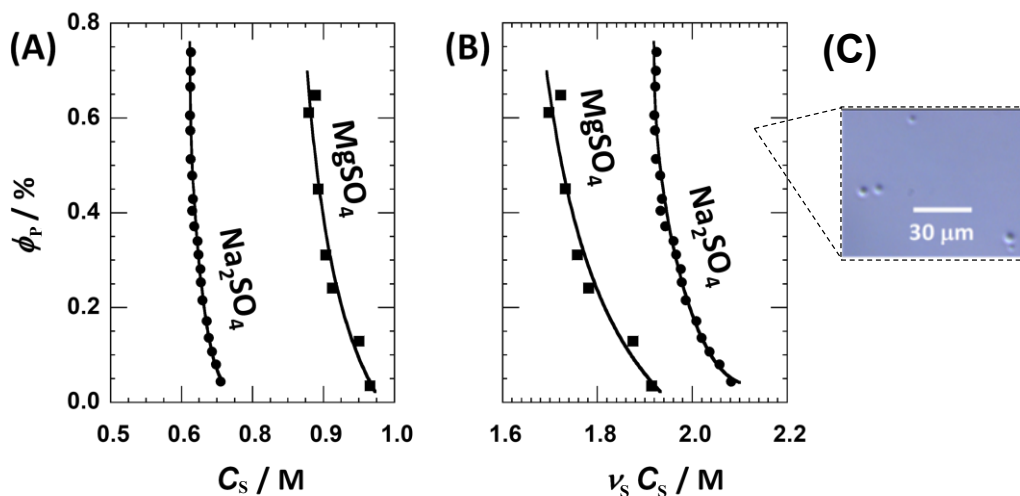


Figure 18. Isothermal phase diagram of tyloxapol volume fraction (ϕ_p) as a function of (A) salt concentration and (B) osmolarity, showing binodal phase boundary for MgSO_4 and Na_2SO_4 Cases. (C) Phase-contrast microscope image showing formation of surfactant-rich spherical microdroplets.

The surfactant concentration selected for the multicomponent-diffusion experiments is 1.00 mM (based on tyloxapol molecular weight) or $\phi_p = 0.4\%$. Note that the critical point for tyloxapol is estimated to be located at $\phi_p \approx 10\%$,¹³⁸ which is well above our experimental ϕ_p values. Thus, in our experimental conditions, sample scattering beyond the binodal curve is caused by a small amount of surfactant-rich phase. To confirm this description, a sample was prepared at $C_s = 0.7 \text{ M}$ (Na_2SO_4) and $\phi_p = 0.4\%$ and then observed by phase-contrast light microscopy.

As we can see in Figure 18C, this sample consists of spherical droplets with a diameter of $\approx 5 \mu\text{m}$, sparsely dispersed in the background liquid. The formation of surfactant-rich droplets is driven by salt-induced inter-micellar attractive interactions.^{111, 153} These interactions are responsible for strong thermodynamic non-ideality, which are expected to also affect multicomponent-diffusion properties of ternary surfactant-salt-water mixtures. From the

binodal curves, the maximum salt concentration in our diffusiophoresis experiments was selected to be ≈ 0.7 M. In sections 11.2 and 11.3, our experimental results on the effect of salt on micelle diffusion coefficient and related hydrodynamic (Stokes) radius was experimentally determined using DLS.

11.2 Effect of Na_2SO_4 concentration on Micelle Diffusion Coefficients and Hydrodynamic Radius

In Figure 19A, we plot the DLS diffusion coefficient, \mathcal{D}_P (experimental values are reported in Appendix A1), as a function of surfactant volume fraction, ϕ_P , ranging from 0.08% to 0.40%, at constant Na_2SO_4 concentrations, C_S , ranging from 0 to 0.65 M, near surfactant cloud point (see Figure 18A for comparison). At the highest surfactant volume fraction of $\phi_P=0.40\%$, we can see that increasing salt concentration from $C_S=0$ to 0.65 M makes the value of \mathcal{D}_P to dramatically reduces, becoming, at 0.65 M, only 18% of its value in water. The observed trends are qualitatively consistent with previous studies performed on different surfactants in the presence of electrolytes^{79, 110, 143}.

A decrease in \mathcal{D}_P is a consequence of Na_2SO_4 salting-out effect and it can be related to both a change in micelle size (aggregation number) and an increase in inter-micellar attractive interactions.^{110, 154} The effect of salt concentration on inter-micellar interactions can be determined by using the linear relation, $\mathcal{D}_P = D_p^0 (1 + K\phi_P)$, where the unitless normalized slope, $K(C_S)$, is known¹⁰⁹ to decrease as inter-micellar attractive interactions increase. To assess the effect of salt over micelle size, at any given C_S , $D_p^0(C_S)$ is converted into the corresponding

hydrodynamic radius, R_p , using the Stokes-Einstein relation (see chapter 7, section 6.1, eq. (7.10)) for spheres¹⁰⁹ and the known viscosity⁷⁴ of the binary Na_2SO_4 -water system.

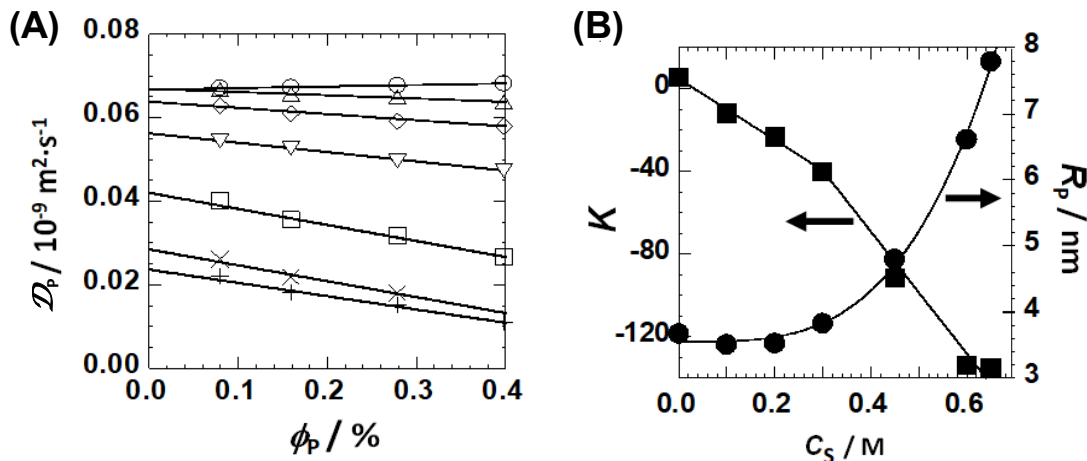


Figure 19. (A) DLS diffusion coefficient, \mathcal{D}_p , as a function of tyloxapol volume fraction, ϕ_p , at constant sodium sulfate concentration, $C_S / \text{M} = 0$ (\circ), 0.10 (Δ), 0.20 (\diamond), 0.30 (∇), 0.45 (\square), 0.60 (\times), 0.65 ($+$) at 25 °C. Solid lines are linear fits through the data. (B) Micelle hydrodynamic radius, R_p (\circ), and slope, K (\square), as a function of salt concentration. Curves are eye guides.

In Figure 19B, we plot R_p and K as a function of C_S . According to experimental results, we can identify two regions based on salt concentration. For Na_2SO_4 concentrations up to 0.3 M, we find that $R_p \approx 3.5$ nm is approximately constant. Correspondingly, the value of K is observed to linearly decrease from +6 at $C_S = 0$ to -40 at $C_S = 0.3$ M. The positive value of K at $C_S = 0$ is consistent with inter-micellar interactions being repulsive¹⁰⁹ in water. This is attributed to both steric interactions and hydrophilicity of PEG groups on the micelle surface. As C_S increases, K becomes negative consistent with inter-micellar interactions becoming more attractive in salting-out conditions.

At salt concentrations higher than 0.3 M, R_p starts to significantly rise, reaching the value of $R_p = 7.8$ nm at $C_S = 0.65$ M. According to geometric considerations based on surfactant

molecular structure,¹⁵⁴ large R_P values require an increase in micelle ellipticity. Thus, the observed increase in R_P may reflect micellar growth leading to the formation of relatively larger aggregates which is accompanied by a change in particle shape. In this salt concentration range, the value of K decreases more rapidly, becoming -135 at the highest salt concentration.

11.3 Effect of $MgSO_4$ concentration on Micelle Diffusion Coefficients and Hydrodynamic Radius

We also determined $D_P(\phi_P, C_S)$ in the $MgSO_4$ case (experimental values are reported in Appendix A2). The observed behavior of our experimental (see Figure 20A) data follows the same trend observed in the Na_2SO_4 case (see section 11.2).

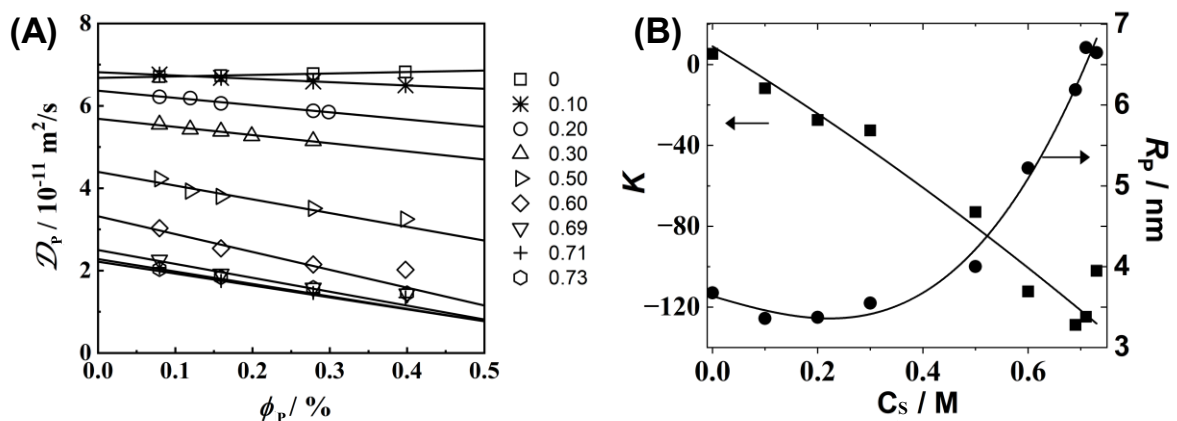


Figure 20. (A) DLS diffusion coefficient, D_P , as a function of tyloxapol volume fraction, ϕ_P , at constant magnesium sulfate concentration at 25 °C. Solid lines are linear fits through the data. (B) Micelle hydrodynamic radius, R_P (\circ), and slope, K (\square), as a function of salt concentration. Curves are eye guides.

In the case of $MgSO_4$, the calculated R_P from Stokes-Einstein equation (using known viscosity data¹⁵⁵ on the binary $MgSO_4$ -water system) is approximately constant when $C_S < 0.5$ M, with $R_P \approx 3.5$ nm. Correspondingly, the value of K is observed to linearly decrease from

+6 at $C_2=0$ to -76 at $C_S=0.5$ M. At salt concentrations higher than 0.5 M, R_p starts to significantly rise, reaching the value of $R_p=6.7$ nm at $C_S=0.70$ M. In this salt concentration range, the value of K further decreases, becoming approximately -128 in the salt range 0.69-0.7 M.

11.4 Ternary Diffusion Coefficients

In this section we report our experimental results on the ternary diffusion coefficients obtained from Rayleigh interferometry. Except for one composition, our data were obtained at the same tyloxapol concentration of $C_P=1.00$ mM ($\phi_P=0.4\%$), which is sufficiently high to achieve satisfactory precision in our diffusion measurements (error of $\approx 5\%$ or less). At this surfactant concentration, our mixtures are dilute micellar solutions ($\phi_P \ll 1$).

In Table 3 and Table 4 we report our ternary diffusion coefficient data in the volume-fixed reference frame for Na_2SO_4 and MgSO_4 , respectively. To alleviate notation, the subscripts “V” appended to diffusion coefficients (see Chapter 8) are omitted. At the highest Na_2SO_4 concentration ($C_S = 0.64$ M), the preparation of macroscopic salt concentration gradients required the use of slightly opaque samples. Nonetheless, the presence of a few dispersed micro-droplets did not significantly affect laser transmission through the diffusion cell and the precision of our interferometric measurements.

For both salts, their main-term diffusion coefficient, D_{SS} , is at least 10-fold larger than the surfactant main-term, D_{PP} . This is consistent with micelles being significantly larger than inorganic ions. The surfactant main-term diffusion coefficient, D_{PP} , significantly decreases as C_S increases, for both salts. This is consistent with what we observed for $D_p^0(C_S)$ in section 11.2 and 11.3.

Table 3. Ternary diffusion coefficients, D_{ij} , in the volume-fixed reference frame at for the tyloxapol(P)-Na₂SO₄(S) aqueous system at tyloxapol molar concentration of $C_P=1.00$ mM and 25 °C.

C_2/M	D_{PP} $10^{-11} \text{ m}^2 \cdot \text{s}^{-1}$	D_{SS} $10^{-11} \text{ m}^2 \cdot \text{s}^{-1}$	D_{PS}/C_P $10^{-11} \text{ m}^2 \cdot \text{s}^{-1} \cdot \text{M}^{-1}$	D_{SP}/D_{SS}
0	6.96±0.01	-	-	-
0.10	6.46±0.01	97.3±0.1	68±1	0.93±0.02
0.20	5.85±0.01	91.3±0.1	64±1	1.83±0.03
0.30	4.92±0.01	86.4±0.2	59±1	2.88±0.06
0.50	2.74±0.01	78.1±0.3	54±2	5.51±0.05
0.60	1.99±0.01	74.5±0.3	60±3	6.52±0.09
0.64	1.68±0.01	73.5±0.3	56±3	6.70±0.08
0.60 ^a	2.08±0.02	75.1±0.5	56±7	6.90±0.30

^a Tyloxapol concentration is 0.65 mM instead of 1.00 mM.

Table 4. Ternary diffusion coefficients, D_{ij} , in the volume-fixed reference frame at for the tyloxapol(P)-MgSO₄(S) aqueous system at tyloxapol molar concentration of $C_P=1.00$ mM and 25 °C.

C_S $/M$	D_{PP} $10^{-11} \text{ m}^2 \cdot \text{s}^{-1}$	D_{SS} $10^{-11} \text{ m}^2 \cdot \text{s}^{-1}$	D_{PS}/C_P $10^{-11} \text{ m}^2 \cdot \text{s}^{-1} \cdot \text{M}^{-1}$	D_{SP}/D_{SS}
0	6.96±0.01	-	-	-
0.10	6.33±0.02	58.5±0.1	59±1	1.18±0.15
0.30	5.14±0.03	48.9±0.1	50±1	3.09±0.06
0.50	3.51±0.02	44.2±0.2	54±3	5.57±0.06
0.65	2.33±0.01	42.2±0.2	39±4	7.08±0.05

At $C_S=0.65$ M, D_{PP} becomes only 24% and 33% of its value at $C_S=0$ for Na_2SO_4 and MgSO_4 , respectively. A significant decrease in $D_{PP}(C_S)$ can be related to a corresponding increase in osmotic compressibility as the surfactant cloud point is approached (see chapter 8, section 8.6).¹¹¹ In other words, micelle concentration gradients become less effective in dissipating surfactant-rich domains in the proximity of phase separation.

On the other hand, it is important to note that the values of D_{SS} are just slightly lower (Na_2SO_4 : 1.0-1.6%, MgSO_4 : 1.5-2.6%) than those measured in the binary salt-water system at the same salt concentrations (diffusion coefficients of binary salt-water systems are reported in Appendix B1). This slight difference, which can be attributed to a small obstruction effect¹⁵⁶ exerted by the micelles on the diffusion of salt ions, indicates that micelles have a negligible effect on salt thermodynamic non-ideality.

Based on eqs. (8.30) and (8.32) in chapter 8 (section 8.3), cross-term diffusion coefficients are reported as D_{PS}/C_P and D_{SP}/D_{SS} . Both coefficients, in all cases, are positive implying that micelle diffusiophoresis occurs from high to low salt concentration and salt osmotic diffusion occurs from high to low micelle concentration, respectively. At low surfactant concentration, D_{PS}/C_P and D_{SP}/D_{SS} can be assumed⁴ to be independent of C_P , within the experimental error. Thus, they are used to calculate \widehat{D}_{PS} and \widehat{D}_{SP} according to eqs. (8.30) and (8.34) (see section 8.3) and their behavior will be further discussed in section 11.5.

To rule out the presence of appreciable dependence of cross-terms on C_P , ternary diffusion coefficients were also determined at the lower tyloxapol concentration of $C_P=0.65$ mM and $C_S=0.60$ M (Na_2SO_4), where micellar osmotic compressibility is expected to significantly deviate from ideality even for dilute micellar solutions. Values of D_{PS}/C_P and D_{SP}/D_{SS} at $C_S=0.65$ mM (last row in Table 3) was found to be essentially the same as those at

1.00 mM and the same salt concentration within the experimental error. Hence, we assume that D_{PS}/C_P and D_{SP}/D_{SS} values are independent of C_P , consistent with previous studies.⁴

To further examine the behavior of D_{PP} and its connection to surfactant cloud point, we consider the determinant of chemical-potential derivatives: $\det(\mu) = \mu_{PP}\mu_{SS} - \mu_{PS}\mu_{SP}$ with $\mu_{ij} = (\partial\mu_i/\partial C_j)_{C_k}$ (with $i, j = P, S$ and $k \neq j$). The condition of $\det(\mu) = 0$ defines the locus of the spinodal curve (see eq. (6.63), Chapter 6, Section 6.3), which represents the boundary between metastable and unstable domains inside the mixture miscibility gap. Note that this condition is equivalent to stating that $(\partial\Pi/\partial C_M)_{\mu_S} = 0$, where Π is the micelle osmotic pressure (see eq. (6.64), Chapter 6, Section 6.3).¹¹¹ The condition, $\det(\mu) = 0$, implies that the lower eigenvalue of the 2×2 diffusion-coefficient matrix, \tilde{D}_P is also zero (see Chapter 8, Section 8.5).¹⁵⁷⁻¹⁶⁰ Thus, we include the plot \tilde{D}_P as a function of salt concentration in Figure 21.

In Figure 21, the behavior of \tilde{D}_P closely follows that of D_{PP} , with $D_{PP} = \tilde{D}_P$ for the binary tyloxapol-water system ($C_S = 0$). Their difference, $D_{PP} - \tilde{D}_P$, slightly increases with salt concentration. This is the mathematical consequence of $D_{PS}D_{SP} > 0$ (see Chapter 8, Section 8.5). At $C_S = 0.64$ M, near the cloud point, \tilde{D}_P becomes 76% of D_{PP} and only 18% of its value at $C_S = 0$. A simple linear extrapolation indicates that $\tilde{D}_P = 0$ corresponds to $C_S = 0.75$ M. This salt concentration, which is also included in the phase diagram (see Figure 18) estimates the position of the spinodal boundary at $\phi_P = 0.4\%$.

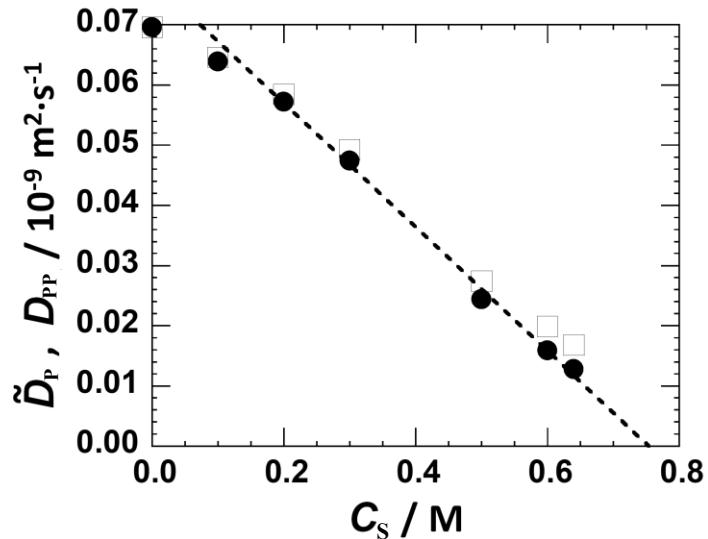


Figure 21. The main-term diffusion coefficient, D_{PP} (□), describing micelle diffusion due to its concentration gradient, and lower eigenvalue of the diffusion-coefficient matrix, \tilde{D}_P (●), as a function of sodium sulfate concentration, C_S . A solid line is a linear fit through \tilde{D}_P data at $C_S = 0.30$ M and higher salt concentrations.

11.5 Theoretical examination of Micelle Diffusiophoresis and Salt Osmotic Diffusion for micellar aqueous solutions.

In this section, we examine micelle diffusiophoresis and salt osmotic diffusion revisiting the formalism of non-equilibrium thermodynamics discussed in Chapter 8, Section 8.2. This is especially important to address the roles of micelle aggregation number and inter-micellar interactions in *dilute* micellar solutions near surfactant cloud point. It is important to remark that C_p is here defined as the surfactant molar concentration based on the molecular mass of surfactant unimer (4.5 kg/mol for tyloxapol). In other words, the actual molar concentration of micelles is C_p divided micelle aggregation number.

We start by first writing an expression for osmotic compressibility (see Section 6.3 in Chapter 6) that is relevant to micellar aqueous solutions:

$$\left(\frac{\partial C_p}{\partial \Pi} \right)_{\mu_s} = \frac{\tilde{m}}{RT} \quad (11.1)$$

where $\tilde{m}(C_p, \mu_s)$ can be interpreted as an *apparent micelle aggregation number*, generally a function of surfactant concentration, C_p , and salt chemical potential, μ_s . For example, \tilde{m} may increase with C_p due to inter-micellar interactions and with μ_s due to an increase in average micelle aggregation number with salt concentration, C_s .

If we use the Gibbs-Duhem equation at constant pressure and temperature, $-d\Pi + C_p d\mu_p + C_s d\mu_s = 0$, we can rewrite eq. (11.1) replacing the osmotic pressure, Π , with the surfactant chemical potential, μ_p (based on unimer molecular weight):

$$\frac{C_p}{RT} \left(\frac{\partial \mu_p}{\partial C_p} \right)_{\mu_s} = \tilde{m}^{-1} \quad (11.2)$$

The differential of $\mu_p(C_p, \mu_s)$ and eq. (11.2) can be then used to obtain the following expression for $\nabla \mu_p$, as:

$$\nabla \mu_p(C_p, \mu_s) = \frac{1}{\tilde{m}} \frac{RT}{C_p} \nabla C_p + \left(\frac{\partial \mu_p}{\partial \mu_s} \right)_{C_p} \nabla \mu_s \quad (11.3)$$

Substitution of eq. (11.3) into eq. (8.25) yields:

$$-\bar{v}_p = \frac{RT L_{pp}}{\tilde{m} C_p} \left\{ \nabla \ln C_p + \tilde{m} \left[\left(\frac{\partial \mu_p}{\partial \mu_s} \right)_C + \frac{L_{ps}}{L_{pp}} \right] \frac{\nabla \mu_s}{RT} \right\} \quad (11.4)$$

Equation (11.4) is a generalization of eq. (8.21), which applies at finite surfactant concentrations and includes apparent micelle aggregation number, \tilde{m} . For surfactants in which critical micelle concentration is very small compared to experimental concentrations, extrapolations of thermodynamic and transport quantities at $C_p \rightarrow 0$ will practically yield

infinite-dilution values of micellar particles. Thus, the apparent micelle aggregation number can be rewritten as

$$\tilde{m} = \frac{m(\mu_S)}{y_p(C_p, \mu_S)} \quad (11.5)$$

where $m(\mu_S) \equiv \tilde{m}(0, \mu_S)$ is the infinite-dilution average micelle aggregation number and $y_p(C_p, \mu_S)$ is a thermodynamic factor, essentially describing inter-micellar interactions, with $y_p(0, \mu_S) = 1$ and $y_p = 0$ on the spinodal boundary. We can then rewrite eq. (11.4) in the following way:

$$-\tilde{v}_p = \frac{RT L_{pp}}{m C_p} \left\{ y_p \nabla \ln C_p + m \left[\left(\frac{\partial \mu_p}{\partial \mu_S} \right)_{C_p} + \frac{L_{ps}}{L_{pp}} \right] \frac{\nabla \mu_S}{RT} \right\} \quad (11.6)$$

Note that the factor multiplying $\nabla \mu_S / RT$ in eq. (11.6) is related to micelle diffusiophoresis and is independent of y_p . In the limit of $C_p \rightarrow 0$, we know that $RT L_{pp} / m C_p \rightarrow D_p^0$. We then redefine:

$$\gamma \equiv m \lim_{C_p \rightarrow 0} \left(\frac{\partial \mu_p}{\partial \mu_S} \right)_{C_p} \quad (11.7)$$

$$\lambda \equiv -m \lim_{C_p \rightarrow 0} \frac{L_{ps}}{L_{pp}} \quad (11.8)$$

Substituting eqs. (8.39) and (8.40) in eq. (8.38) we recover our initial eq. (8.21). In this limit, we also note that eq. (8.35) becomes:

$$\frac{\nabla \mu_p}{RT} = \frac{1}{m} \nabla \ln C_p + \frac{\gamma}{m} \frac{\nabla \mu_S}{RT} \quad (11.9)$$

and eq. (8.26) can be rewritten as:

$$-\bar{v}_p = D_p^0 \left[m \frac{\nabla \mu_p}{RT} - \lambda \frac{\nabla \mu_s}{RT} \right] \quad (11.10)$$

A micellar colloidal solution may be sufficiently diluted such that $(RT/m)(L_{pp}/C) \cong D_p^0$, $\gamma \cong m(\partial\mu_p/\partial\mu_s)_{C_p}$ and $\lambda \cong -mL_{ps}/L_{pp}$ are good approximations. However, it may still exhibit large osmotic compressibility (e.g., near the cloud point). This implies the thermodynamic factor, y_p , is significantly smaller than one and cannot be omitted. In this case, eq. (8.26) should be replaced by:

$$-\bar{v}_p \cong D_p^0 \left[y_p \nabla \ln C_p + (\gamma - \lambda) \frac{\nabla \mu_s}{RT} \right] = D_p^0 \left[y_p \nabla \ln C_p + \hat{D}_{ps} \frac{\nabla \mu_s}{RT} \right] \quad (11.11)$$

In eq. (11.11), $y_p \nabla \ln C_p$ describes normal diffusion and $\hat{D}_{ps} \nabla \mu_s / RT$ diffusiophoresis. Since y_p decreases as spinodal boundary is approached ($y_p=0$) at high salt concentrations, the diffusiophoresis term in eq. (11.11) becomes relatively more important compared to normal diffusion in the proximity of cloud point.

For the salt osmotic coefficient, as in the case of diffusiophoresis, we need to address the roles of micelle aggregation number and inter-micellar interactions in dilute micellar solutions near surfactant cloud point. We, therefore, combine eq. (8.16) with $-(J_s)_w = (D_{sp})_w \nabla C + (D_{ss})_w \nabla C_s$ to obtain (see also Chapter 8):

$$\frac{(D_{sp})_w}{(D_{ss})_w} = \frac{L_{sp}\mu_{pp} + L_{ss}\mu_{sp}}{L_{sp}\mu_{ps} + L_{ss}\mu_{ss}} \quad (11.12)$$

We then rearrange eq. (11.12) in the following way:

$$\frac{(D_{sp})_w}{(D_{ss})_w} = \frac{\mu_{sp} + \frac{L_{ps}}{L_{pp}} \frac{L_{pp}\mu_{pp}}{L_{ss}\mu_{ss}}}{1 + \frac{L_{ps}}{L_{pp}} \frac{L_{pp}\mu_{ps}}{L_{ss}\mu_{ss}}} \quad (11.13)$$

where we have also replaced L_{SP} with L_{PS} (ORR). We then use the differential of $\mu_p(C_p, \mu_s)$ and eq. (11.2) to rewrite the thermodynamic factor, μ_{pp} , in the numerator of eq. (11.13) in the following way:

$$\mu_{pp} \equiv \left(\frac{\partial \mu_p}{\partial C_p} \right)_{C_s} = \left(\frac{\partial \mu_p}{\partial C_p} \right)_{\mu_s} + \left(\frac{\partial \mu_p}{\partial \mu_s} \right)_C \left(\frac{\partial \mu_s}{\partial C_p} \right)_{C_s} = \frac{RT}{C_p} \left(\frac{1}{\tilde{m}} + \frac{\mu_{MS}}{\mu_{SS}} \frac{\mu_{SP}}{RT} C_p \right) \quad (11.14)$$

For diluted surfactant solutions, the terms $L_{pp}\mu_{pp}$ and $L_{ss}\mu_{ss}$ can be rewritten as:

$$L_{pp}\mu_{pp} \cong (mC_p D_p^0) \frac{1}{C_p} \left(\frac{1}{\tilde{m}} + \frac{\mu_{PS}}{\mu_{SS}} \frac{\mu_{SP}}{RT} C_p \right) = D_p^0 \left(y_p + \frac{\mu_{PS}}{\mu_{SS}} \frac{\mu_{SP}}{RT} C_p \right) \cong D_p^0 y_p \quad (11.15)$$

$$L_{ss}\mu_{ss} \cong D_s \quad (11.16)$$

where D_s is the salt diffusion coefficient of the binary salt-water system in the solvent-fixed reference frame. Thus, we have:

$$\frac{L_{pp}\mu_{pp}}{L_{ss}\mu_{ss}} \cong \alpha y_p \quad (11.17)$$

where $\alpha \equiv D_p^0 / D_s$ is a mobility ratio. The denominator in eq. (11.13) reduces to:

$$1 + \frac{L_{PS}}{L_{PP}} \frac{L_{PP}\mu_{PS}}{L_{SS}\mu_{SS}} \cong 1 + \frac{L_{PS}}{L_{SS}} \frac{mC_p D_p^0}{D_s} \frac{\mu_{PS}}{RT} \cong 1 \quad (11.18)$$

Thus, eq. (11.13) can be rewritten as:

$$\frac{(D_{SP})_W}{(D_{SS})_W} \cong \frac{\mu_{SP}}{\mu_{SS}} + \frac{L_{PS}}{L_{PP}} \alpha y_p \quad (11.19)$$

If we use the definition given by eq. (11.8) and define the preferential-interaction coefficient as

$$C_{SP} \equiv -\lim_{C \rightarrow 0} \left(\frac{\partial C_S}{\partial C_P} \right)_{\mu_s} = \frac{\mu_{SP}}{\mu_{SS}} \quad (11.20)$$

We can then write:

$$\frac{(D_{SP})_W}{(D_{SS})_W} \cong C_{SP} - \alpha \frac{\lambda}{m} y_P \quad (11.21)$$

where the second term in eq. (11.21) is small compared to C_{SP} . Thus, $(D_{SP})_W / (D_{SS})_W \approx C_{SP}$ weakly depends on y_P .

Finally, in the limit of $C_P \rightarrow 0$, we can set $y_P = 1$ and write:

$$\hat{D}_{PS} = \gamma - \lambda \quad (11.22)$$

$$\hat{D}_{SP} = C_{SP} - \alpha \frac{\lambda}{m} \quad (11.23)$$

In Part II Chapter 6, the preferential-interaction coefficient C_{SP} was linked to γ by eq. (6.49)

. To consider micelle aggregation, number, we replace γ with γ/m and rewrite eq. (6.49) in the following way:

$$C_{SP} = (1 - C_S \bar{V}_S) \frac{\gamma}{m} + C_S \tilde{V}_P \quad (11.24)$$

where $\tilde{V}_P \equiv \bar{V}_P - (\nu_{SY})^{-1} \bar{V}_S / m \approx \bar{V}_P$ with \bar{V}_P being the surfactant molar volume based on surfactant molecular weight.

11.6 Effect of Na₂SO₄ and MgSO₄ concentration on Micelle Diffusiophoresis and Salt Osmotic Diffusion

The cross-diffusion parameters, D_{PS}/C_P in Table 5 (Na₂SO₄) and Table 6 (MgSO₄) were converted into the corresponding diffusiophoresis coefficient, \hat{D}_{PS} , eq. (8.32), by employing the mobility values, D_p^0 , extracted from DLS measurements and available^{108, 148} thermodynamic data on aqueous Na₂SO₄ (Appendix C1) and MgSO₄ (Appendix C2). On the

other hand, the salt osmotic diffusion coefficient, \hat{D}_{SP} , was directly taken as equal to the ratios D_{SP}/D_{SS} in Table 3 (Na_2SO_4) and Table 4 (MgSO_4). Values of \hat{D}_{PS} and \hat{D}_{SP} are reported in Table 5 for the Na_2SO_4 case and Table 6 for the MgSO_4 case. Extracted values of C_{SP} and γ/m are also included in Tables 5,6. The procedure to extract these thermodynamic parameters will be further discussed in the next section. Furthermore, values of γ/m will be used to determine water thermodynamic excess using the preferential hydration model (see Chapter 8 in Part II).

Table 5. Diffusiophoresis, salt osmotic diffusion and related parameters for the tyloxapol- Na_2SO_4 aqueous system.

C_S/M	\hat{D}_{PS}	\hat{D}_{SP}	D_P^0 $10^{-11} \text{ m}^2 \cdot \text{s}^{-1}$	α	C_{SP}	γ/m
0.10	0.46	0.96	6.92	0.0703	0.99	0.60
0.20	0.95	1.88	6.66	0.0712	1.96	1.17
0.30	1.56	2.96	5.82	0.0661	3.07	1.89
0.50	3.76	5.61	3.87	0.0482	5.77	3.83
0.60	6.72	6.61	2.94	0.0384	6.74	4.44
0.64	7.83	7.08	2.56	0.0337	7.20	4.76

Table 6. Diffusiophoresis, salt osmotic diffusion and related parameters for the tyloxapol- MgSO_4 aqueous system.

C_S/M	\hat{D}_{PS}	\hat{D}_{SP}/m	\hat{D}_P^0 $10^{-11} \text{ m}^2 \cdot \text{s}^{-1}$	α	C_{SP}/m	γ/m
0.10	0.52	1.23	7.04	0.1231	1.33	0.94
0.30	1.72	3.23	5.85	0.1178	3.47	2.28
0.50	4.02	5.76	4.53	0.0994	6.12	4.15
0.65	5.71	7.26	2.84	0.0658	7.56	5.00

11.6.1 Micelle diffusiophoresis at low salt concentration

We will first focus on the behavior of micelle diffusiophoresis and salt osmotic diffusion for Na_2SO_4 concentrations up to 0.3 M. Within this salt concentration range, micelle size can be assumed to be approximately constant (see section 11.2 and Fig. 19B for behavior of R_p). Correspondingly, we may assume that micelles are colloidal particles with a fixed aggregation number within this salt concentration range. In Figure 22, we plot \hat{D}_{PS} and \hat{D}_{SP} as a function of Na_2SO_4 concentration. Both coefficients linearly increase with C_S and approach zero at $C_S=0$ as expected⁶ for neutral colloidal particles (see Part II Chapter 8). Positive values of \hat{D}_{PS} and \hat{D}_{SP} imply that micelle diffusiophoresis occurs from high to low salt concentrations and salt osmotic diffusion occurs from high to low micelle concentration, respectively.

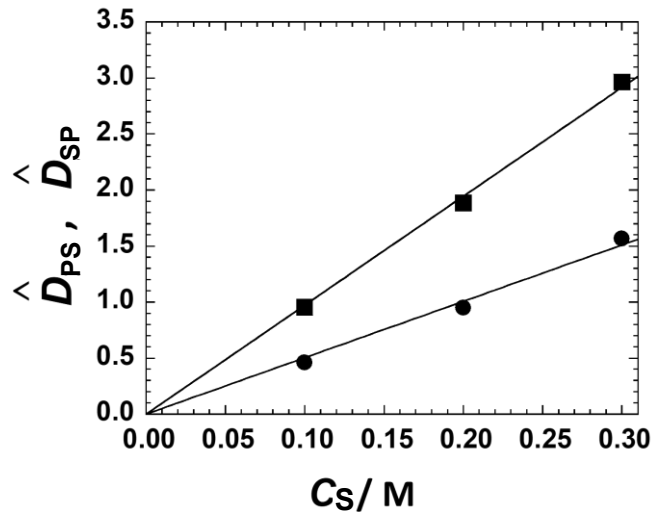


Figure 22. Micelle diffusiophoresis coefficient, \hat{D}_{PS} (\bullet), and salt osmotic diffusion coefficient, \hat{D}_{SP} (\blacksquare), as a function of Na_2SO_4 concentration, C_S . Solid lines are linear fits through the data with zero intercept.

The observed behavior of $\hat{D}_{\text{PS}}(C_{\text{S}})$ and $\hat{D}_{\text{SP}}(C_{\text{S}})$ requires that the thermodynamic and transport coefficients, $\gamma(C_{\text{S}})$ and $\lambda(C_{\text{S}})$, must also linearly increase with C_{S} with $\gamma(0) = \lambda(0) = 0$. To physically interpret this behavior, we will theoretically examine the behavior of $\hat{D}_{\text{PS}}(C_{\text{S}})$ and $\hat{D}_{\text{SP}}(C_{\text{S}})$ using eqs. (11.22) and (11.23) in section 11.4.

The coefficient, γ , can be then extracted from salt osmotic diffusion because \hat{D}_{SP} is related to the preferential-interaction coefficient, C_{PS} , (see eq. (11.20)), which is thermodynamically linked to γ by eq. (11.24). We can then interpret the behavior of $\gamma(C_{\text{S}})$ and $\lambda(C_{\text{S}})$ by considering a hydration model previously described in Chapter 8. This thermodynamic parameter, which can be regarded as a constant, represents the number of water molecules near the colloidal particle in excess with respect to bulk per surfactant unit (Section 8.4); it quantifies the cosolute salting-out strength. Satisfactory values of N_{W} can be directly obtained from \hat{D}_{SP} data using $\hat{D}_{\text{SP}} \approx C_{\text{SP}} \approx (\bar{V}_{\text{P}} + N_{\text{W}} \bar{V}_{\text{W}}) \cdot C_{\text{S}}$, making this parameter approximately independent of m .

The ratio λ/γ , is the second parameter that can be extracted from \hat{D}_{PS} and \hat{D}_{SP} data and can be regarded as a constant. Contrary to N_{W} , its value will appreciably depend on m . In our hydration model, eq. (8.77), represents the fraction of the inner local domain. The ratio of $N_{\text{W}}^{(\text{II})}(1 - K^{(\text{II})})$ to $N_{\text{W}}^{(\text{I})}(1 - K^{(\text{I})})$, which describes a reduction in water excess as we move from the inner to the outer local domain. It is expected to have a relatively weak dependence on cosolute chemical nature compared to N_{W} . Previous diffusiophoresis studies on PEG chains in water showed that N_{W} significantly depends on cosolute nature.^{6, 107} Specifically, the water excess per ethoxy group was found to be 7.8, 2.4, and 5.7 in the presence of Na_2SO_4 , NaCl ,

and TMAO, respectively.^{6, 107} On the other hand, the corresponding values of λ/γ were all similar to each other ($\lambda/\gamma=0.87-0.89$). These results represent an important reference point for our analysis.

To determine N_w and λ/γ from our data in Figure 22, we use the aggregation number value of $m=7$ based on previous light-scattering work from our research lab.¹⁵² Note that the value of m is somewhat small due to the oligomeric nature of tyloxapol. Indeed, this aggregation number corresponds to ≈ 50 Triton X-100 units. We obtain: $N_w = 332 \pm 13$ and $\lambda/\gamma = 0.885 \pm 0.004$ from our Na_2SO_4 data. If we assume that tyloxapol consists of ≈ 50 ethoxy groups based on its chemical structure,¹⁴² we determine that this N_w value corresponds to a thermodynamic excess of 6.6 water molecules per ethoxy group. For comparison, the value of 7.8 was extracted for PEG with the same salt.⁶ This reduction of 15% may be attributed to a somewhat reduced solvent-accessible area of micellar PEG chains compared to free PEG chains. In the case of λ/γ , we essentially find the same value obtained for PEG with Na_2SO_4 (0.884). This is consistent with this ratio being a weak function of particle chemical nature.

As previously mentioned, the calculated value of λ/γ depends on m . If we set: $m=6$ and $m=8$, we obtain: $\lambda/\gamma=0.866$ and 0.900 , respectively. If we set $m=1$ and ignore micelle formation altogether, we calculate $\lambda/\gamma=0.16 \pm 0.03$, which is considerably different from those previously reported. This analysis shows how the λ/γ value at $m=7$ reflects the correct colloidal osmolarity of tyloxapol solutions.

In the MgSO_4 case, micelle size is approximately constant for salt concentrations up to ≈ 0.5 M according to Figure 20B. We extract $N_w = 450 \pm 30$ from our C_{SP} data (Table 6). Correspondingly, we determined a thermodynamic excess of ≈ 9 water molecules per ethoxy

group in the presence of MgSO_4 , which is higher than that of ≈ 7 extracted in the Na_2SO_4 case. Note that our comparison considers the difference in number of salt ions ($\nu_S=2$ for MgSO_4 and $\nu_S=3$ for Na_2SO_4) because γ is defined with respect to μ_S , not C_S . This trend is qualitatively consistent with cloud-point results showing that MgSO_4 is a somewhat stronger salting-out agent than Na_2SO_4 (see Section 11.1). For tyloxapol in the presence of MgSO_4 , we determine $\lambda/\gamma=0.89\pm 0.03$ with $m=7$. This result is also consistent with this ratio being a weak function of particle chemical nature.

11.6.2 Diffusiophoresis and Salt Osmotic Diffusion near Surfactant Cloud Point

In Figure 23, we plot the micelle diffusiophoresis coefficient, \widehat{D}_{PS} , as a function of Na_2SO_4 concentration, C_S , up to 0.64 M, near surfactant cloud point. Here, we can see that the behavior of $\widehat{D}_{\text{PS}}(C_S)$ exhibits a significant deviation from linearity, with a marked upward curvature, as C_S approaches the binodal curve (see Figure 18).

This behavior is related to the significant decrease in micelle tracer-diffusion coefficient, $D_p^0(C_S)$, as C_S increases, which is a consequence of the increase in micelle radius illustrated in Figure 19B. To confirm this, we calculate $\widehat{D}_{\text{PS}}(C_S)$ by using the same value of $D_p^0(0)$ in water at all salt concentrations. As we can see in Figure 23, the recalculated values of $\widehat{D}_{\text{PS}}(C_S)$ linearly increases with C_S , consistent with the behavior discussed at low salt concentration. A comparison of the two sets of data in Figure 23 shows that the value of \widehat{D}_{PS} near the cloud point is 2.6-fold larger than that linearly extrapolated from \widehat{D}_{PS} data at low salt concentration.

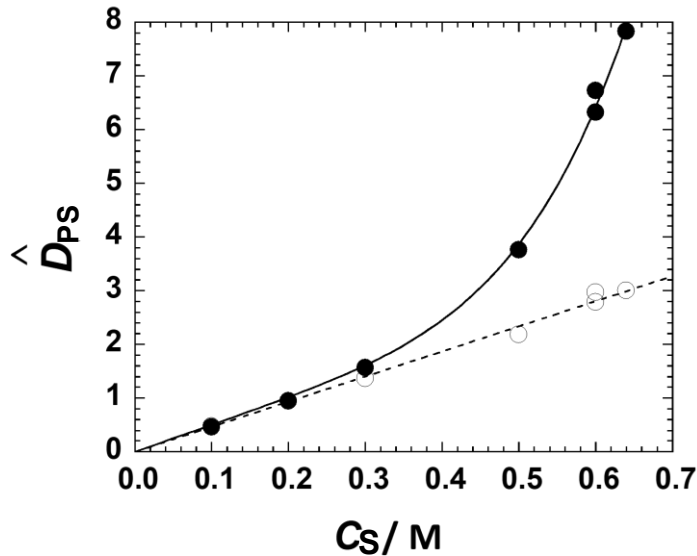


Figure 23. Micelle diffusiophoresis coefficient, \hat{D}_{PS} (●, solid curve) as a function of sodium sulfate concentration, C_S . Values of \hat{D}_{PS} (○, dashed curve) calculated using the same micelle mobility, $D_p^0(0)$, instead of $D_p(C_S)$ for all salt concentrations are included. Curves are fit through the experimental data.

In Figure 24, we plot salt osmotic diffusion coefficient, \hat{D}_{SP} , as a function of Na_2SO_4 concentration, up to 0.64 M. For comparison, we also show the corresponding values of salt partition coefficients, C_{SP} . These are just 2-4% larger than \hat{D}_{SP} , illustrating that this transport coefficient is essentially a thermodynamic quantity. Both quantities exhibit a slight upward curvature at high C_S , corresponding to a moderate increase of $\approx 20\%$ in the value C_{SP}/C_S near the cloud point.

The observed growth in micelle hydrodynamic radius, R_P , at high salt concentrations ($C_S > 0.3$ M) should reflect a corresponding increase in the aggregation number with salt concentration. Thus, the hydration model discussed in Section 8.4 may be potentially less accurate at high salt concentrations. Nonetheless, we tentatively use the value of

$\lambda/\gamma=0.885$ extracted at low C_S to gauge the values of m at high C_S . We find $m \approx 9$ at $C_S=0.5$ M and $m \approx 13$ at the highest salt concentrations, qualitatively consistent with micellar growth.

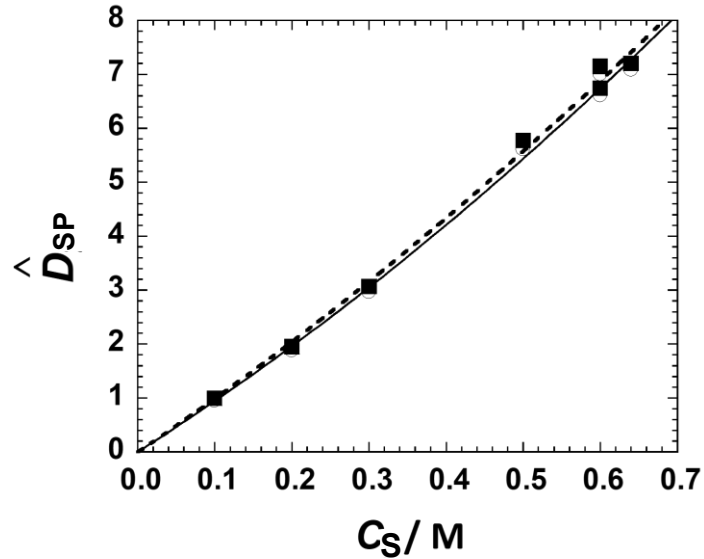


Figure 24. Salt osmotic diffusion, \hat{D}_{SP} (■, solid curve) as a function of sodium sulfate concentration, C_S . For comparison, values of C_{SP} (□, dashed curve) were calculated using eq. (11.24) are included. Solid curves fit through the data.

In Figure 25 we show $\hat{D}_{PS}(C_S)$ and $\hat{D}_{SP}(C_S)$ for the $MgSO_4$ case. As in the Na_2SO_4 case, the upward curvature in the behavior of $\hat{D}_{MS}(C_S)$ is mostly related to the significant decrease of micelle mobility $D_p^0(C_S)$ occurring at high salt concentrations as indicated by the behavior of $R_P(C_S)$ in Figure 20. We also include the values of C_{SP} using the aggregation number value of $m=7$.¹⁵² Values of C_{SP} are found to be just 3-8% larger than \hat{D}_{SP} , thereby showing again that \hat{D}_{SP} is approximately a thermodynamic quantity.

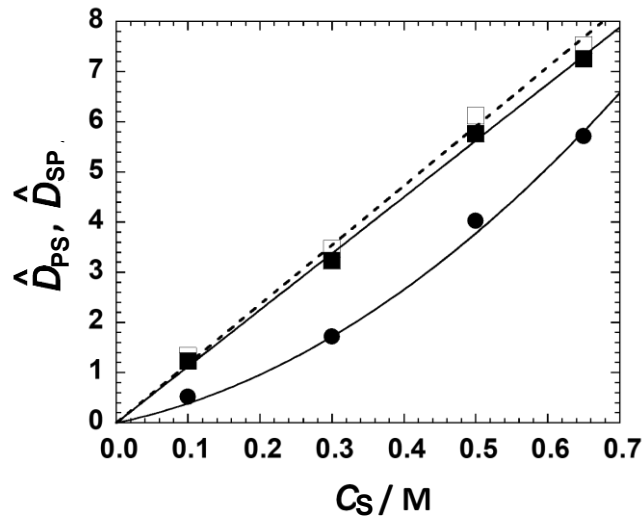


Figure 25. Micelle diffusio-phoresis coefficient, \widehat{D}_{PS} (●), salt osmotic diffusion coefficient, \widehat{D}_{SP} (■), and preferential-interaction coefficient, C_{SP} (□) as a function of magnesium sulfate concentration, C_S . Curves associated with \widehat{D}_{PS} (solid curve), \widehat{D}_{SP} (solid line) and C_{SP} (dashed line) are fits through the data.

For both salts, the observed increase in micelle hydrodynamic radius, R_P , at high salt concentrations describes a salt-induced change in the surfactant aggregation state, which may also affect interpretation of micelle diffusio-phoresis. In other words, micelle diffusio-phoresis may not only be caused by preferential hydration but also by another fundamental mechanism arising from salt-induced aggregation. The description of this newly identified mechanism and its contribution to micelle diffusio-phoresis will be further discussed in Section 11.7.

11.7 Effect of Salt-induced Surfactant Aggregation in Micelle Diffusio-phoresis

We have used the preferential-hydration model to describe micelle diffusio-phoresis in the presence of salt concentration gradients. However, this model, which assumes that micelles can be treated as fixed colloidal particles, is expected to be valid if micelle size is independent of salt concentration. As shown from our DLS results, we can identify a salt concentration range in which R_P is approximately constant and a relatively high salt concentration range in

which R_P significantly increases with C_S . The observed strong upward convexity of R_P / R_P^0 indicates that salt is not promoting a stepwise growth in aggregate size but a substantial cooperative change in surfactant aggregation state. We can approximately describe this self-assembly process by assuming that surfactant aggregation can occur in two distinct aggregation states in chemical equilibrium. At low salt concentrations, spherical micelles are more thermodynamically stable. As C_S increases, micelle thermodynamic stability decreases due to preferential hydration. As a critical salt concentration, C_S^* , is reached, a different aggregation state involving a relatively large number of surfactants unimers becomes thermodynamically more stable than the micelle.

In other words, relatively large aggregates can better sustain harsh salting-out conditions. For instance, these aggregates may optimize contacts between PEG chains and reduce their exposure to salt ions by having a relatively large curvature radius compared to micelles. Furthermore, according to geometric considerations based on surfactant molecular structure,¹⁵⁴ surfactant aggregates that are large compared to micelles cannot be spherical. Indeed, an increase in micelle ellipticity occurs, thereby leading to the formation of worm-like aggregates with a thickness comparable with micelle diameter. Micelle (M) and the proposed worm-like aggregate (A) are illustrated in Figure 27.

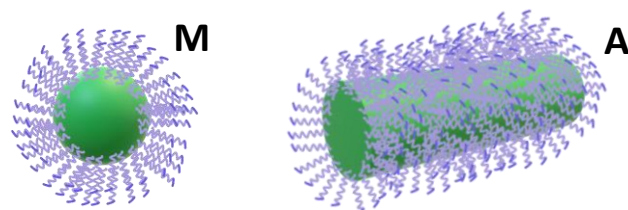


Figure 26. Spherical micelle (M) and worm-like aggregate (A).

From a qualitative point of view, an increase aggregate concentration with C_S should produce diffusiophoresis from low to high salt concentration. This corresponds to a negative contribution to the value of $\widehat{D}_{PS}(C_S)$. To explain this mechanism, we consider two aqueous solutions in contact with each other with the same surfactant concentration but at different salt concentrations, as schematized in Figure 28. Since the extent of aggregation is higher in the compartment at high salt concentration, there exists a difference in micelle concentration causing micelle diffusion from low to high salt concentration. Correspondingly, there is also a difference in aggregate concentration responsible for aggregate diffusion in the opposite direction. However, this is less important because the mobility of aggregates is low compared to that of relatively smaller spherical micelles. Thus, the net effect is surfactant diffusiophoresis from low to high salt concentration.

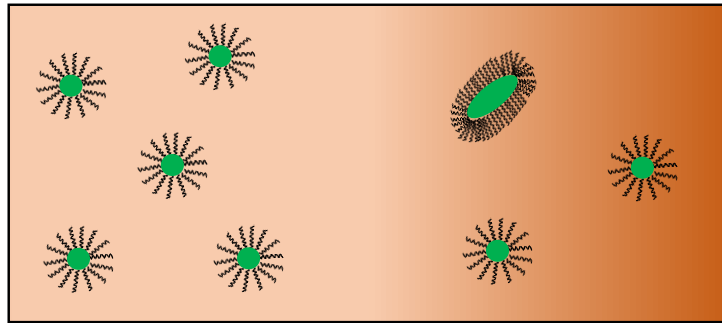


Figure 27. Aqueous surfactant solution at a low salt concentration (left side) in contact with a solution at a high salt concentration (right side). The salt gradient is portrayed as a color contrast for simplicity. Both solutions share the same surfactant concentration and the aggregate (elongated particle) on the right side corresponds to the mass of three micelles. The number of micelles on the left side is higher than that on the right side due to the aggregate formation.

Since it is not clear how salt-induced aggregation contributes to diffusiophoresis, this aspect will be further examined below quantitatively. Specifically, we have developed an aggregation model that properly describes the observed behavior of hydrodynamic radius.

11.7.1 Aggregation Model

In Chapter 2 (section 2.2), we described micellization as a chemical equilibrium between the surfactant unimers and the micelles. Here we introduce a mass-action model to include the contribution of large aggregates. Specifically, we assume that surfactant unimers (T) can reversibly make both spherical micelles (M) and larger aggregates (A) with well-defined aggregation numbers.

In our model, the micelle radius is a weighted average between micelle and aggregate radius. These equilibria can be described by considering the following reversible reactions: $mT \rightleftharpoons M$ and $amT \rightleftharpoons A$, where m is the micelle aggregation number and a is the ratio of aggregate-to-micelle aggregation numbers. The total surfactant concentration is:

$$C_P = C_1 + mC_M + amC_A \quad (11.25)$$

where C_1 , C_M , and C_A are the concentrations of free surfactant (T), micelles (M), and aggregates (A), respectively. In principle, the fraction of aggregates and micelles becomes zero in the limit of $C_P \rightarrow 0$ as all surfactants should occur as free unimers at infinite dilution. Furthermore, dilution also favors micelles with respect to aggregates because aggregate formation requires a larger number of unimers compared to micelles. However, the range of surfactant concentrations in which disaggregation becomes favored may be sufficiently low that cannot be accessed experimentally.

Using a surfactant with a sufficiently low cmc, such as tyloxapol, we can neglect C_1 in eq. (11.25) and assume that extrapolation to $C_p \rightarrow 0$ of experimental data yields physicochemical quantities that relate to micelles and larger aggregates but not to surfactant unimers. Thus, we approximate eq. (11.25) to:

$$C_p = mC_M + a mC_A \quad (11.26)$$

Correspondingly, the fraction of aggregated surfactant is:

$$X_A = \frac{a mC_A}{C_p} \cong \frac{a mC_A}{mC_M + a mC_A} \quad (11.27)$$

while the fraction of micellar surfactant is $1 - X_A$. In our model, the increase in micelle hydrodynamic radius, $R_p(C_s)$, is caused by an increase in X_A with salt concentration. Our goal is to determine a mathematical expression for X_A .

Micelle-aggregate chemical equilibrium can be described by:

$$\frac{C_A}{C_M^a} = \left(\frac{C_p^*}{m} \right)^{1-a} \quad (11.28)$$

where $(C_p^* / m)^{1-a}$ is the equilibrium constant, rewritten so that C_p^* is a critical surfactant concentration above which aggregates become favored with respect to micelles. We can then introduce the fraction of aggregated surfactant in eq. (11.28) and write:

$$\frac{X_A}{1 - X_A} = a \left(\frac{mC_M}{C_p^*} \right)^{a-1} \quad (11.29)$$

To introduce the effect of salt concentration on micelle-aggregate chemical equilibrium, we assume that C_p^* depends on salt concentration, C_s . Since salt promotes the formation of aggregates at high salt concentration, C_p^* must decrease as salt osmolarity

increases. This salting-out effect can be described by assuming that $\ln C^*$ linearly decreases as C_S increases:

$$\ln C_P^* = \ln C_P^{0*} - K_S' C_S \quad (11.30)$$

where C_P^{0*} is the value of C_P^* in the absence of salt and the slope, K_S' , is as a salting-out constant. Within the framework of preferential-hydration formalism, $K_S' / \nu_S \approx (N_W^{(M)} - N_W^{(A)}) V_W$, where $N_W^{(M)}$ and $N_W^{(A)}$ are water excesses in the micellar and aggregate state, respectively. The positive parameters, $N_W^{(M)}$ and $N_W^{(A)}$, characterize how surfactant chemical potential in micelle and aggregate states increases with salt concentration. If the surfactant chemical potential in the micelle state increases more rapidly than that in the aggregate state ($N_W^{(M)} > N_W^{(A)}$), then $K_S' > 0$. This implies that there exists a salt concentration above which aggregates become more stable than micelles.

Based on eq. (11.30), the ratio, mC_M / C_P^* in eq. (11.29), can be now rewritten in the following way:

$$\frac{mC_M}{C_P^*} = \frac{mC_M}{C_P} \frac{C_P}{C_P^*} = (1 - X_A) \frac{C_P}{C_P^{0*}} e^{K_S' C_S} \quad (11.31)$$

We are interested in the behavior of eq. (11.31) in the limit of $C_P \rightarrow 0$. To ensure that X_A and mC_M / C_P^* remain finite in this limit, we should interpret both C_P^* and C_P^{0*} as infinitely small with the ratio C_P / C_P^{0*} being a finite quantity. We expect that $C_P / C_P^{0*} \ll 1$ as aggregates are negligible compared to micelles in water. However, as salt concentration increases, the factor $(C_P / C_P^{0*}) e^{K_S' C_S}$ increases thereby making the fraction of aggregates no

longer negligible. It is convenient to introduce a salt concentration C_S^* such that $(C_P / C_P^{0*}) e^{K'_S C_S^*} = 1$. We can then rewrite eq. (11.31) in the following way:

$$\frac{mC_M}{C_P^*} = (1 - X_A) e^{K'_S (C_S - C_S^*)} \quad (11.32)$$

This expression mC_M / C^* is then inserted in eq. (11.29) to obtain:

$$X_A = a (1 - X_A)^a e^{K_S (C_S - C_S^*)} \quad (11.33)$$

with $K_S \equiv (a-1)K'_S$.

The chemical equilibrium condition between micelles and aggregates can be then written in the following way:

$$\ln \frac{X_A / a}{(1 - X_A)^a} = K_S (C_S - C_S^*) \quad (11.34)$$

If the parameters a , K_S and C_S^* are known, eq. (11.34) can be numerically solved by X_A using Newtown's method starting from $X_A = 0$.¹⁶¹ To establish that this model is consistent with the increase in the hydrodynamic radius, we need to have a mathematical expression for particle hydrodynamic radius, $R_p(C_S)$, together with one for the particle diffusiophoresis coefficient, $\hat{D}_{ps}(C_S)$, and their relation to X_A . This will be shown in the next section.

11.7.2 Effect of Aggregation on Particle Hydrodynamic Radius and Diffusiophoresis

To describe the effect of aggregation on surfactant diffusion, we assume simple Fick's first law for individual diffusion of micelle and aggregate:

$$J_M = -D_M \nabla C_M \quad (11.35)$$

$$J_A = -D_A \nabla C_A \quad (11.36)$$

where J_M and J_A are micelle and aggregate fluxes, and D_M and D_A the corresponding diffusion coefficients. According to mass balance (see eq. (11.26)) the total surfactant flux is given by:

$$\frac{J_P}{m} = J_M + aJ_A = -D_M \nabla C_M - aD_A \nabla C_A \quad (11.37)$$

Assuming rapid equilibrium, the concentration gradients ∇C_M and ∇C_A can be related to ∇C_P and ∇C_S by:

$$\nabla C_M = \left(\frac{\partial C_M}{\partial C_P} \right)_{C_S} \nabla C_P + \left(\frac{\partial C_M}{\partial C_S} \right)_{C_P} \nabla C_S \quad (11.38)$$

$$\nabla C_A = \left(\frac{\partial C_A}{\partial C_P} \right)_{C_S} \nabla C_P + \left(\frac{\partial C_A}{\partial C_S} \right)_{C_P} \nabla C_S \quad (11.39)$$

Accordingly, eq. (11.37) becomes:

$$J_P = -D_{PP} \nabla C_P - D_{PS} \nabla C_S \quad (11.40)$$

where:

$$D_{PP} = m \left(\frac{\partial C_M}{\partial C_P} \right)_{C_S} D_M + ma \left(\frac{\partial C_A}{\partial C_P} \right)_{C_S} D_A \quad (11.41)$$

$$D_{PS} = m \left(\frac{\partial C_M}{\partial C_S} \right)_{C_P} D_M + ma \left(\frac{\partial C_A}{\partial C_S} \right)_{C_P} D_A \quad (11.42)$$

The four partial derivatives that appear in eqs. (11.41)-(11.42) can be expressed as functions of X_A . Since $aC_A = (C_P / m) X_A$ and $C_M = (C_P / m)(1 - X_A)$, we can first write:

$$m \left(\frac{\partial C_M}{\partial C_P} \right)_{C_S} = (1 - X_A) - C_P \left(\frac{\partial X_A}{\partial C_P} \right)_{C_S} \quad (11.43)$$

$$ma \left(\frac{\partial C_A}{\partial C_P} \right)_{C_S} = X_A + C_P \left(\frac{\partial X_A}{\partial C_P} \right)_{C_S} \quad (11.44)$$

$$m \left(\frac{\partial C_M}{\partial C_S} \right)_{C_P} = -C_P \left(\frac{\partial X_A}{\partial C_S} \right)_{C_P} \quad (11.45)$$

$$ma \left(\frac{\partial C_A}{\partial C_S} \right)_{C_P} = C_P \left(\frac{\partial X_A}{\partial C_S} \right)_{C_P} \quad (11.46)$$

We can then deduce the expressions of $(\partial X_A / \partial C_P)_{C_S}$ and $(\partial X_A / \partial C_S)_{C_P}$ from eq. (11.33)

reported below:

$$\left(\frac{\partial X_A}{\partial C_P} \right)_{C_S} = -\frac{a X_A}{1 - X_A} \left(\frac{\partial X_A}{\partial C_P} \right)_{C_S} - K_S X_A \frac{dC_S^*}{dC_P} \quad (11.47)$$

$$\left(\frac{\partial X_A}{\partial C_S} \right)_{C_P} = -\frac{a X_A}{1 - \alpha_A} \left(\frac{\partial X_A}{\partial C_S} \right)_{C_P} + K_S X_A \quad (11.48)$$

To determine dC_S^* / dC_P in eq. (11.47), we observe that C_S^* is defined such that

$K_S C_S^* = -\ln(C_P / C_P^{0*})$. This implies that $K_S (dC_S^* / dC_P) = -(a-1)(1/C_P)$. Thus, the final

expressions of $(\partial X_A / \partial C_P)_{C_S}$ and $(\partial X_A / \partial C_S)_{C_P}$ are:

$$\left(\frac{\partial X_A}{\partial C_P} \right)_{C_S} = \frac{1}{C_P} \frac{(a-1)(1-X_A)X_A}{1+(a-1)X_A} \quad (11.49)$$

$$\left(\frac{\partial X_A}{\partial C_S} \right)_{C_P} = K_S \frac{(a-1)(1-X_A)X_A}{1+(a-1)X_A} \quad (11.50)$$

Substitution of eqs. (11.49)-(11.50) into eqs. (11.43)-(11.46) allows us to rewrite eqs. (11.41)

-(11.42) in the following way:

$$D_{PP} = \frac{(1 - X_A)D_M + aX_A D_A}{(1 - X_A) + aX_A} \quad (11.51)$$

$$D_{PS} = -C_P \frac{(a-1)K_S v_S (1 - X_A)X_A}{(1 - X_A) + aX_A} (D_M - D_A) \quad (11.52)$$

assuming that $X_A \ll 1$ when $C_S = 0$, we have $D_{PP} = D_M$ in the absence of salt. In eq. (11.51)

we can assume $D_{PP} \cong D_M$ if $X_A \ll 1$. This condition is approximately achieved in the absence of salt ($C_S = 0$).

Since the hydrodynamic radius $R_p(C_S)$ is inversely proportional to D_{PP} , we obtain:

$$\frac{R_p}{R_p^0} = \frac{1 - X_A + aX_A}{1 - X_A + aX_A \alpha_a} \quad (11.53)$$

where $R_p^0 \equiv R_p(0)$ and $\alpha_a \equiv D_A / D_M$ is a mobility ratio. According to eq. (11.53), R_p increases with X_A when $\alpha_a < 1$. It is interesting to observe that the same expression of R_p can be obtained in dynamic light scattering by assuming that micelles and aggregates are not in chemical equilibrium. Indeed, aX_A represents the light-scattering weight of the aggregates.

To obtain the expression of the diffusiophoresis coefficient, \hat{D}_{PS} , Equation (11.33) can be combined with eq. (11.53) as shown below:

$$\hat{D}_{PS} = \frac{D_{PS}C_S}{v_S D_{PP} C_P} = - \frac{(1 - X_A)X_A}{1 - X_A + aX_A \alpha_a} \frac{(1 - \alpha_A)K_S}{v_S} C_S \quad (11.54)$$

To calculate $\hat{D}_{PS}(C_S)$, we need to know the values of a , α_a , K_S and X_A , with X_A obtained from a , K_S and C_S^* using eq. (11.33). To reduce the number of parameters, we can set the value of a equal to a few representative values: $a = 10, 20$ and 100 and calculate α_a from a by assuming that micelles are spheres and aggregates are prolate ellipsoids with minor

semiaxis equal to micelle radius, R_M , and major semiaxis, $R_A > R_M$. The diffusion-coefficient ratio can then be written as:

$$\alpha_a = \frac{D_A}{D_M} = \frac{R_M}{(R_A R_M^2)^{1/3}} \varphi \quad (11.55)$$

where φ is the Perrin shape factor.^{162, 163} For a prolate ellipsoid, it is known that:

$$\varphi = \frac{(R_M / R_A)^{2/3}}{\sqrt{1 - (R_M / R_A)^2}} \ln \frac{1 + \sqrt{1 - (R_M / R_A)^2}}{(R_M / R_A)} \quad (11.56)$$

Assuming micelle and aggregate share the same density, the ratio of aggregate-to-micelle volume $R_A R_M^2 / R_M^3 = R_A / R_M$ is equal to the ratio of aggregate-to-micelle aggregation numbers, a . This leads to

$$\alpha_a = \frac{\ln(a + \sqrt{a^2 - 1})}{\sqrt{a^2 - 1}} \quad (11.57)$$

Thus, for a given value of a , α_a is directly obtained using eq. (11.57). We then can use experimental data of $R_p(C_S)$ to extract K_S and C_S^* . Specifically, we combine eqs. (11.33) and (11.53) to write:

$$\frac{R_p}{R_p^0} = \frac{1 + a(a-1)e^{K_S(C_S - C_S^*)}(1 - X_A)^a}{1 + a(\alpha_a - 1)e^{K_S(C_S - C_S^*)}(1 - X_A)^a} \quad (11.58)$$

According to eq. (11.58), R_p / R_p^0 depends on two variables, C_S and X_A , while K_S and C_S^* being the two parameters to be determined. However, the set of values of X_A to be used on the right side of eq. (11.33) is initially unknown as they depend on K_S and C_S^* . We therefore can choose two approximate values of K_S and C_S^* , and calculate X_A at each

experimental C_S from eq. (11.33). Specifically, we can numerically solve eq. (11.33) using Newton's method¹⁶¹ starting with $X_A^{(0)} = 0$:

$$X_A^{(i)} = X_A^{(i-1)} - \frac{X_A^{(i-1)} - a (1 - X_A^{(i-1)})^a e^{K_2(C_2 - C_2^*)}}{1 + a^2 (1 - X_A^{(i-1)})^{a-1} e^{K_2(C_2 - C_2^*)}} \text{ with } i=1,2,3,\dots \quad (11.59)$$

The method of least squares based on eq. (11.58) is then applied to $R_P(C_S, X_A)$ data and new values of K_S and C_S^* are extracted. These are then used to recalculate the set of values of X_A using eq. (11.59). This procedure is repeated until values of K_S and C_S^* remain the same within their statistical uncertainties.

11.7.3 Application of Aggregation Model to Experimental hydrodynamic Radius

In Figure 26, we show the normalized behavior of $R_P(C_S)$ experimentally obtained in both $MgSO_4$ and Na_2SO_4 cases, with R_P^0 being R_P at $C_S = 0$. We can use the two-state model discussed in the previous section together with the experimental behavior of R_P/R_P^0 shown in Figure 26 to quantitatively evaluate the role of salt-induced aggregation on diffusiophoresis. Since the formation of aggregates becomes appreciable only at high salt concentrations, we assume that $X_A \ll 1$ at $C_S = 0$. After numerically solving eq. (11.59) for the chemical-equilibrium condition between micelles and aggregates, we can obtain $X_A(C_S)$.

To establish that this model is consistent with the observed increase in hydrodynamic radius, we used the mathematical expression for R_P/R_P^0 , see eq. (11.58) with three representative values of aggregate size, corresponding to $a = 10, 20$ and 100 . We then apply the method of least squares to experimental R_P/R_P^0 in order to extract the values of salting-out constant, K_S , and critical salt concentration, C_S^* .

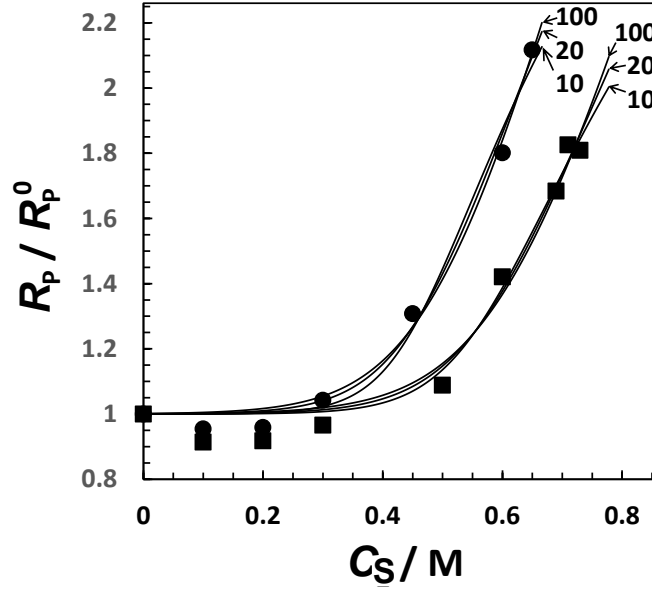


Figure 28. Normalized hydrodynamic radius, R_p / R_p^0 , as a function of salt concentration, C_s , with R_p^0 being R_p at $C_s = 0$ (Na_2SO_4 , \bullet ; MgSO_4 , \blacksquare). Curves are fit through the data based on Eqs. (11.57) and (11.58). Employed values of a are appended to each curve.

In Figure 29, we include the best fits based on eq. (11.54) with three mentioned values of a . As we can see from this figure, theoretical curves reasonably describe experimental behavior. Note that the observed two-fold increase in R_p / R_p^0 shown in Figure 27 will not be described well by eq. (11.58) if a is too small ($a < 10$). This is related to the dependence of α_a on a , which is in general weaker than $\alpha_a \sim a^{-1}$. The obtained values of K_S and C_S^* are reported in Table 7 below for both salt cases.

Table 7. Parameters extracted by applying the method least squares based on eq. (8.142).

a	α_a	$K_S / M^{-1} (\text{Na}_2\text{SO}_4)$	$C_S^* / M^{-1} (\text{Na}_2\text{SO}_4)$	$K_S / M^{-1} (\text{MgSO}_4)$	$C_S^* / M^{-1} (\text{MgSO}_4)$
10	0.3008	19 ± 3	0.72 ± 0.02	16 ± 3	0.89 ± 0.03
20	0.1846	15 ± 2	0.91 ± 0.03	13 ± 3	1.08 ± 0.08
100	0.0530	12 ± 2	1.3 ± 0.1	11 ± 3	1.5 ± 0.2

The values of K_S and C_S^* in Table 7 can be then used to calculate $\widehat{D}_{PS}(C_S)$ using eq. (11.54). As we can see from Fig. 29, calculated values of $\widehat{D}_{PS}(C_S)$ are small compared to the experimental values of \widehat{D}_{PS} . This analysis allows us to conclude that aggregation dynamics play a marginal role in surfactant diffusiophoresis compared to preferential hydration.

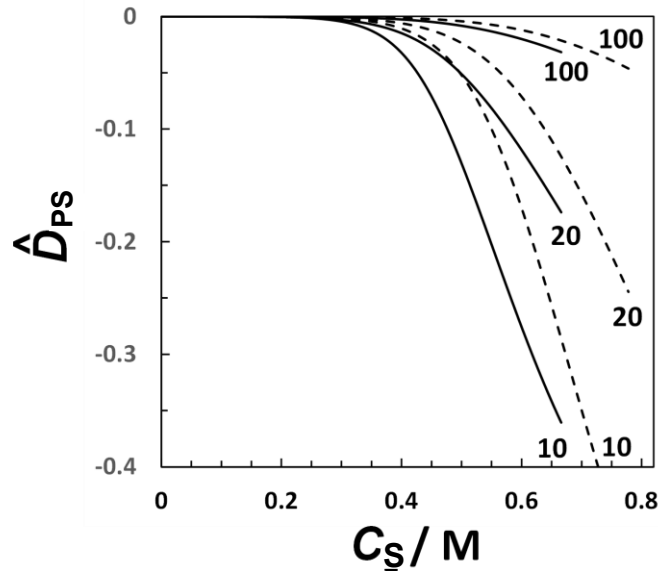


Figure 29. Reduced diffusiophoresis coefficients, \widehat{D}_{PS} , as a function of salt concentration, C_S , (Na_2SO_4 , solid curves; MgSO_4 , dashed curves). Employed values of a are appended to each curve.

11.8 Significance of Micelle Diffusiophoresis

Altogether our results show that diffusiophoresis becomes the dominant diffusion mechanism responsible for the transport of micelles near cloud point. To assess the significance of diffusiophoresis, numerical simulations are generally needed. Nonetheless, there is a simple case in which diffusiophoresis can be examined. Specifically, we may consider a steady-state diffusion process that is appropriate for colloidal particles in the

presence of salt.⁶ As illustrated in Figure 30A, a horizontal tube positioned between $x=0$ and $x=l$ is sandwiched between two reservoirs consisting of pure water ($C_S=0$, left compartment, $x \leq 0$) and a binary salt–water solution ($C_S=C_S^{(\max)}$, right compartment, $x \geq l$), respectively.

To cover our experimental salt concentration range, we set: $C_S^{(\max)}=0.65$ M. Two membranes, not permeable to colloidal particles, seal the two tube extremities. Hence, the condition, $\vec{V}_p=0$, must be respected throughout the tube in steady-state conditions. In this case, we write:

$$\frac{d \ln C_P}{dC_S} = -w \quad (11.60)$$

where $w \equiv v_{S,ys} \widehat{D}_{PS} / C_S$. In the absence of diffusiophoresis, $w=0$ and particle concentration, C_P , inside the tube is uniform at C_P^0 .

In the presence of diffusiophoresis, a particle concentration profile, $C_P^0(x)$, develops in steady-state conditions, with $C_P^0 = l^{-1} \int_0^l C_P dx$. We approximate our experimental data on micelle diffusiophoresis to the function: $w=w_0=10 \text{ M}^{-1}$ for $C_S \leq \hat{C} = 0.4 \text{ M}$ and $w=w_0+w' \cdot (C_S-\hat{C})$ with $w' = 50 \text{ M}^{-2}$ for $C_S \geq \hat{C}$. Since the salt concentration profile can be described by $C_S=C_S^{(\max)} \cdot (x/l)$, integration of $\ln C_P$ with respect to C_S , yields $C_P(x)$.

Our results, which are described in Figure 30B, show that micelle concentration is enhanced (6.5-fold larger than C_P^0) and depleted (0.2% of C_P^0) near the left and right membrane locations, respectively. Note that $\log C_P$ is also curving down towards the salt-water reservoir. This behavior is related to the upward curvature of $\widehat{D}_{PS}(C_S)$ as C_S approaches the cloud point. This analysis shows a nearly quantitative displacement of micelles from the region with salt concentrations near the surfactant cloud point.

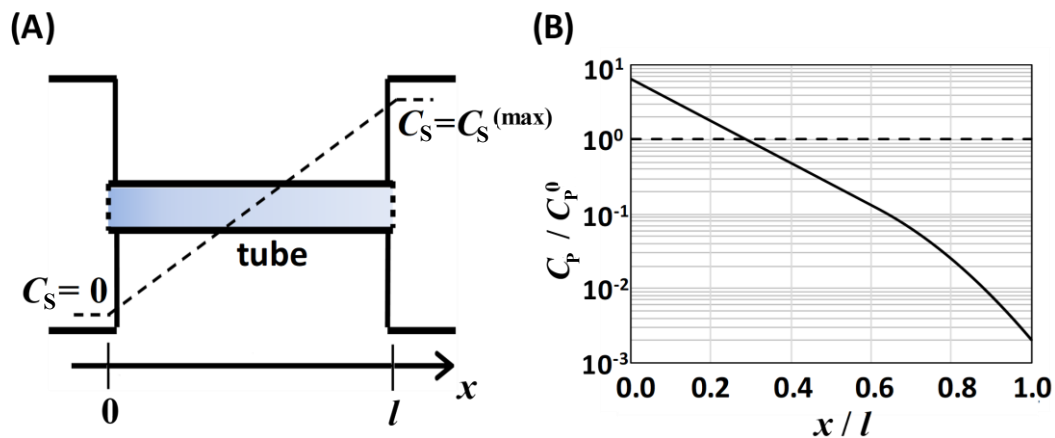


Figure 30. (A) The schematic diagram for examining particle diffusiophoresis in steady-state conditions. A tube of length l containing a micellar solution is connected to two salt reservoirs with salt concentrations $C_S=0$ and $C_S=C_S^{(\max)}=0.65$ M. The dashed line with a positive slope describes the salt concentration profile, $C_S= C_S^{(\max)} \cdot (x/l)$. Vertical dashed lines at the tube extremities denote two membranes not permeable to micelles. (B) Logarithmic diagram showing particle concentration profile (C_P/C_P^0 , solid curve) as a function of position (x/l) inside the tube calculated using the $w(C_S)$ function reported in the text. The dashed horizontal line corresponds to $w=0$.

CHAPTER 12

CONCLUSIONS

Electrophoretic diffusiophoresis has been widely studied for charged colloidal particles.^{5, 9, 13, 164, 165} However, there is no experimental studies regarding diffusiophoresis of non-charged particles.^{26, 28, 136} An important class of non-charged colloidal particles are those functionalized with hydrophilic PEG chains. For these particles, diffusiophoresis may be established based on PEG hydrophilicity not particle charge. Here we reported the first experimental study on diffusiophoresis of a neutral PEG-based globular particle. Specifically, we have successfully characterized diffusiophoresis of tyloxapol micelles in the presence of two sulfate salts (Na_2SO_4 , MgSO_4), known to be strong salting-out agents.

We examined this transport phenomenon within the framework of multicomponent diffusion. We found that micelle diffusiophoresis occurs from high to low salt concentrations due to PEG preferential hydration for both sulfate salts. Furthermore, the obtain multicomponent diffusion data allowed us to characterize the salt osmotic diffusion, which is usually ignore in colloidal science, and crucial for unraveling the thermodynamic and transport components of the diffusiophoresis coefficient.

We applied a preferential-hydration model to the data of diffusiophoresis coefficient and salt osmotic diffusion as a function of salt concentration. This allows us to determine the thermodynamic excess of water molecules in the micelle local domain ($\text{Na}_2\text{SO}_4 \sim 7 \text{ H}_2\text{O}/\text{ethoxy group}$, $\text{MgSO}_4 \sim 9 \text{ H}_2\text{O}/\text{ethoxy group}$) and the inner domain fraction ($\text{Na}_2\text{SO}_4 \lambda/\gamma = 0.884$, $\text{MgSO}_4 \lambda/\gamma = 0.89$). The latter parameter was found to be similar to values extracted for free PEG chains in previous work within our group.⁶ This suggests that

diffusiophoresis of PEG-based nanoparticles can be estimated from that of free PEG chains.

Near the surfactant cloud point we found that micelle diffusiophoresis becomes the dominant mechanism due to a two-fold increase in micelle size and a large osmotic compressibility. This motivates us to do more systematic diffusiophoresis studies on any other neutral and charged colloidal particles near binodal curves.

Dynamic light scattering results showed that micelle size significantly increases at high sulfate salts concentrations. A two-stage aggregation model was therefore developed to describe the effects of these salts concentrations on the Stokes' radius of tyloxapol micelles. Extracted parameters describing observed salt-induced surfactant aggregation were then used to theoretically calculate diffusiophoresis as a function of salt concentration, ignoring the contribution from preferential hydration. The magnitude of calculated negative values of diffusiophoresis were found to be small compared to the corresponding experimental values, indicating that preferential hydration is the main mechanism causing micelle diffusiophoresis.

Results showed that concentration gradients of salting-out agents such as MgSO_4 and Na_2SO_4 may be employed for achieving migration of PEG-based colloidal particles such as those utilized as drug carriers and extracting agents with applications in the fields of microfluidics,¹¹ particle insertion into dead-end pores for enhanced-oil recovery,¹⁹ soil remediation,¹⁶⁶ and diffusion-based controlled release technologies.^{22, 23}

Future work could include further study if the correlations observed between free PEG chains and PEGylated colloidal particles can be obtained for other types of polymers and their respective functionalized colloidal particles. Additionally, complementary studies of PEG-based colloidal particles in the presence of other salts such as MgCl_2 and CaCl_2 should also be included. Indeed, we have recently reported that gradients of MgCl_2 induce large

diffusiophoresis of proteins due the strong non-ideality thermodynamic factor of this salt.⁵ Furthermore, it has been reported that divalent cations such as Ca^{2+} can form complexes with the ether groups of PEG chains of non-ionic micelles promoting a salting-in effect.^{137, 167, 168} Studies on diffusiophoresis with this type of salts would allow us to examine the effect of cation adsorption on neutral PEG-based colloidal particles on diffusiophoresis. Since cation binding induced a positive charge on colloidal particles, the electrophoretic mechanism mentioned in Chapter 9 (see Figure 17) is also expected to contribute to overall diffusiophoresis. Finally, an ongoing direction in our research lab is the development of devices that can use steady-state salt concentration gradients to induce diffusiophoresis of colloidal particles, with application to the separation of different colloidal particles based on charge or hydrophilicity.

REFERENCES

1. Anderson, J. L., Colloid transport by interfacial forces. *Annu. Rev. Fluid Mech.* **1989**, *21* (1), 61-99.10.1146/annurev.fl.21.010189.000425.
2. Prieve, D. C., Migration of a colloidal particle in a gradient of electrolyte concentration. *Adv. Colloid Interface Sci.* **1982**, *16* (1), 321-335.10.1016/0001-8686(82)85022-7.
3. Abecassis, B.; Cottin-Bizonne, C.; Ybert, C.; Ajdari, A.; Bocquet, L., Boosting migration of large particles by solute contrasts. *Nat. Mater.* **2008**, *7* (10), 785-9.10.1038/nmat2254.
4. Annunziata, O.; Buzatu, D.; Albright, J. G., Protein diffusiophoresis and salt osmotic diffusion in aqueous solutions. *J. Phys. Chem. B* **2012**, *116* (42), 12694-705.10.1021/jp307625d.
5. Fahim, A.; Annunziata, O., Amplification of salt-induced protein diffusiophoresis by varying salt from potassium to sodium to magnesium chloride in water. *Langmuir* **2020**, *36* (10), 2635-2643.10.1021/acs.langmuir.9b03318.
6. McAfee, M. S.; Zhang, H.; Annunziata, O., Amplification of salt-induced polymer diffusiophoresis by increasing salting-out strength. *Langmuir* **2014**, *30* (41), 12210-9.10.1021/la503214b.
7. Velegol, D.; Garg, A.; Guha, R.; Kar, A.; Kumar, M., Origins of concentration gradients for diffusiophoresis. *Soft Matter* **2016**, *12* (21), 4686-703.10.1039/c6sm00052e.
8. Ha, D.; Seo, S.; Lee, K.; Kim, T., Dynamic transport control of colloidal particles by repeatable active switching of solute gradients. *ACS Nano* **2019**, *13* (11), 12939-12948.10.1021/acsnano.9b05507.
9. Shin, S., Diffusiophoretic separation of colloids in microfluidic flows. *Phys. Fluids* **2020**, *32* (10), 101302.10.1063/5.0023415.

10. Shin, S.; Um, E.; Sabass, B.; Ault, J. T.; Rahimi, M.; Warren, P. B.; Stone, H. A., Size-dependent control of colloid transport via solute gradients in dead-end channels. *Proc. Natl. Acad. Sci. U S A* **2016**, *113* (2), 257-261.10.1073/pnas.1511484112.
11. Shim, S., Diffusiophoresis, diffusioosmosis, and microfluidics: Surface-flow-driven phenomena in the presence of flow. *Chem. Rev.* **2022**, *122* (7), 6986-7009.10.1021/acs.chemrev.1c00571.
12. Dey, K. K.; Das, S.; Poyton, M. F.; Sengupta, S.; Butler, P. J.; Cremer, P. S.; Sen, A., Chemotactic separation of enzymes. *ACS Nano* **2014**, *8* (12), 11941-9.10.1021/nn504418u.
13. Shin, S.; Shardt, O.; Warren, P. B.; Stone, H. A., Membraneless water filtration using co₂. *Nat. Commun.* **2017**, *8*, 15181.10.1038/ncomms15181.
14. Guha, R.; Shang, X.; Zydney, A. L.; Velegol, D.; Kumar, M., Diffusiophoresis contributes significantly to colloidal fouling in low salinity reverse osmosis systems. *J. Membr.* **2015**, *479*, 67-76.10.1016/j.memsci.2015.01.024.
15. Kar, A.; Guha, R.; Dani, N.; Velegol, D.; Kumar, M., Particle deposition on microporous membranes can be enhanced or reduced by salt gradients. *Langmuir* **2014**, *30* (3), 793-9.10.1021/la4044107.
16. Sear, R. P.; Warren, P. B., Diffusiophoresis in nonadsorbing polymer solutions: The asakura-oosawa model and stratification in drying films. *Phys. Rev. E* **2017**, *96* (6-1), 062602.10.1103/PhysRevE.96.062602.
17. Larson, R. G., Transport and deposition patterns in drying sessile droplets. *AIChE Journal* **2014**, *60* (5), 1538-1571.10.1002/aic.14338.

18. Park, S. w.; Lee, J.; Yoon, H.; Shin, S., Microfluidic investigation of salinity-induced oil recovery in porous media during chemical flooding. *Energy Fuels* **2021**, *35* (6), 4885-4892.10.1021/acs.energyfuels.0c04320.
19. Liu, R.; Du, D.-j.; Pu, W.-f.; Zhang, J.; Fan, X.-b., Enhanced oil recovery potential of alkyl alcohol polyoxyethylene ether sulfonate surfactants in high-temperature and high-salinity reservoirs. *Energy Fuels* **2018**, *32* (12), 12128-12140.10.1021/acs.energyfuels.8b02653.
20. Sinz, D. K.; Hanyak, M.; Darhuber, A. A., Self-induced surfactant transport along discontinuous liquid-liquid interfaces. *J. Phys. Chem. Lett.* **2013**, *4* (6), 1039-43.10.1021/jz400287x.
21. Kar, A.; Chiang, T.-Y.; Ortiz Rivera, I.; Sen, A.; Velegol, D., Enhanced transport into and out of dead-end pores. *ACS Nano* **2015**, *9* (1), 746-753.10.1021/nn506216b.
22. Shin, S.; Doan, V. S.; Feng, J., Osmotic delivery and release of lipid-encapsulated molecules via sequential solution exchange. *Phys. Rev. Appl.* **2019**, *12* (2), 10.1103/PhysRevApplied.12.024014.
23. Wesselingh, J. A., Controlling diffusion. *J. Control. Release.* **1993**, *24* (1-3), 47-60.10.1016/0168-3659(93)90167-4.
24. Zhang, H.; Annunziata, O., Modulation of drug transport properties by multicomponent diffusion in surfactant aqueous solutions. *Langmuir* **2008**, *24* (19), 10680-7.10.1021/la801636u.
25. Shin, S.; Warren, P. B.; Stone, H. A., Cleaning by surfactant gradients: Particulate removal from porous materials and the significance of rinsing in laundry detergency. *Phys. Rev. Appl.* **2018**, *9* (3), 10.1103/PhysRevApplied.9.034012.

26. Liu, Z.; Robinson, J. T.; Sun, X.; Dai, H., Pegylated nanographene oxide for delivery of water-insoluble cancer drugs. *J. Am. Chem. Soc.* **2008**, *130* (33), 10876-7.10.1021/ja803688x.
27. Doane, T. L.; Cheng, Y.; Babar, A.; Hill, R. J.; Burda, C., Electrophoretic mobilities of pegylated gold nps. *J. Am. Chem. Soc.* **2010**, *132* (44), 15624-31.10.1021/ja1049093.
28. Kolate, A.; Baradia, D.; Patil, S.; Vhora, I.; Kore, G.; Misra, A., Peg - a versatile conjugating ligand for drugs and drug delivery systems. *J. Control. Release.* **2014**, *192*, 67-81.10.1016/j.jconrel.2014.06.046.
29. Patist, A.; Kanicky, J. R.; Shukla, P. K.; Shah, D. O., Importance of micellar kinetics in relation to technological processes. *J. Colloid Interface Sci.* **2002**, *245* (1), 1-15.10.1006/jcis.2001.7955.
30. Kulkarni, J. A.; Thomson, S. B.; Zaifman, J.; Leung, J.; Wagner, P. K.; Hill, A.; Tam, Y. Y. C.; Cullis, P. R.; Petkau, T. L.; Leavitt, B. R., Spontaneous, solvent-free entrapment of sirna within lipid nanoparticles. *Nanoscale* **2020**, *12* (47), 23959-23966.10.1039/d0nr06816k.
31. Uchegbu, I. F.; Vyas, S. P., Non-ionic surfactant based vesicles (niosomes) in drug delivery. *Int. J. Pharm.* **1998**, *172* (1-2), 33-70.10.1016/s0378-5173(98)00169-0.
32. Shah, P. R.; Tan, H.; Taylor, D.; Tang, X.; Shi, N.; Mashat, A.; Abdel-Fattah, A.; Squires, T. M., Temperature dependence of diffusiophoresis via a novel microfluidic approach. *Lab Chip* **2022**, *22* (10), 1980-1988.10.1039/d1lc00916h.
33. Lu, Y.; Zhang, E.; Yang, J.; Cao, Z., Strategies to improve micelle stability for drug delivery. *Nano Res.* **2018**, *11* (10), 4985-4998.10.1007/s12274-018-2152-3.
34. Mangiapia, G.; D'Errico, G.; Simeone, L.; Irace, C.; Radulescu, A.; Di Pascale, A.; Colonna, A.; Montesarchio, D.; Paduano, L., Ruthenium-based complex nanocarriers for cancer therapy. *Biomaterials* **2012**, *33* (14), 3770-82.10.1016/j.biomaterials.2012.01.057.

35. Cacace, M. G.; Landau, E. M.; Ramsden, J. J., The hofmeister series: Salt and solvent effects on interfacial phenomena. *Q. Rev. Biophys.* **1997**, *30* (3), 241-77.10.1017/s0033583597003363.
36. Goodwin, J., *Colloids and interfaces with surfactants and polymers*. 2nd ed.; John Wiley and Sons: UK, 2009; p 22-88.
37. Gulyakin, I. D.; Oborotova, N. A.; Pechennikov, V. M., Solubilization of hydrophobic antitumor drugs (review). *Pharm. Chem. J.* **2014**, *48* (3), 209-213.10.1007/s11094-014-1078-7.
38. Fuhrmann, K.; Schulz, J. D.; Gauthier, M. A.; Leroux, J. C., Peg nanocages as non-sheddable stabilizers for drug nanocrystals. *ACS Nano* **2012**, *6* (2), 1667-76.10.1021/nn2046554.
39. Johannessen, A. M.; Spildo, K., Enhanced oil recovery (eor) by combining surfactant with low salinity injection. *Energy Fuels* **2013**, *27* (10), 5738-5749.10.1021/ef400596b.
40. Kamal, M. S., A review of gemini surfactants: Potential application in enhanced oil recovery. *J. Surfactants Deterg.* **2016**, *19* (2), 223-236.10.1007/s11743-015-1776-5.
41. Yada, S.; Matsuoka, K.; Nagai Kanasaki, Y.; Gotoh, K.; Yoshimura, T., Emulsification, solubilization, and detergency behaviors of homogeneous polyoxypropylene-polyoxyethylene alkyl ether type nonionic surfactants. *Colloids Surf. A: Physicochem. Eng. Asp.* **2019**, *564*, 51-58.10.1016/j.colsurfa.2018.12.030.
42. Li, J.; Tang, Y.; Wang, Q.; Li, X.; Cun, L.; Zhang, X.; Zhu, J.; Li, L.; Deng, J., Chiral surfactant-type catalyst for asymmetric reduction of aliphatic ketones in water. *J. Am. Chem. Soc.* **2012**, *134* (45), 18522-5.10.1021/ja308357y.

43. Wang, M.; Zhang, B.; Li, G.; Wu, T.; Sun, D., Efficient remediation of crude oil-contaminated soil using a solvent/surfactant system. *RSC Adv.* **2019**, *9* (5), 2402-2411.10.1039/c8ra09964b.
44. Wong, F. W. F.; Ariff, A. B.; Stuckey, D. C., Downstream protein separation by surfactant precipitation: A review. *Crit. Rev. Biotechnol.* **2018**, *38* (1), 31-46.10.1080/07388551.2017.1312266.
45. Eastoe, J., Surfactant aggregation and adsorption at interfaces. In *Colloid science: Principles, methods and applications.*, 2nd ed.; Cosgrove, T., Ed. John Wiley and Sons: UK, 2010; pp 62-89.
46. Kronberg, B., The hydrophobic effect. *Curr. Opin. Colloid Interface Sci.* **2016**, *22*, 14-22.10.1016/j.cocis.2016.02.001.
47. Hiemenz, P. C., Rajagopalan, R., *Principles of colloid and surface chemistry.* 3rd ed.; Marcel Dekker, Inc.: USA, 1997; p 355-403.
48. Witten, T., Pincus, P., *Structured fluids: Polymer, colloids, surfactants.* 1st ed.; OXFORD: New York, 2004; p 173-212.
49. Shinoda, K.; Hutchinson, E., Pseudo-phase separation model for thermodynamic calculations on micellar solutions¹. *J. Phys. Chem.* **1962**, *66* (4), 577-582.10.1021/j100810a001.
50. Holmberg, K.; Jönsson, B.; Kronberg, B.; Lindman, B., *Surfactants and polymers in aqueous solution.* 2nd ed ed.; Wiley & Sons, Inc.: Hoboken, 2002.
51. Mukherjee, I.; Moulik, S. P.; Rakshit, A. K., Tensiometric determination of gibbs surface excess and micelle point: A critical revisit. *J. Colloid Interface Sci.* **2013**, *394*, 329-336.10.1016/j.jcis.2012.12.004.

52. Elworthy, P. H.; Mysels, K. J., The surface tension of sodium dodecylsulfate solutions and the phase separation model of micelle formation. *J. Colloid Interface Sci.* **1966**, *21* (3), 331-347.10.1016/0095-8522(66)90017-1.
53. Chatterjee, A.; Moulik, S. P.; Sanyal, S. K.; Mishra, B. K.; Puri, P. M., Thermodynamics of micelle formation of ionic surfactants: A critical assessment for sodium dodecyl sulfate, cetyl pyridinium chloride and dioctyl sulfosuccinate (na salt) by microcalorimetric, conductometric, and tensiometric measurements. *J. Phys. Chem. B* **2001**, *105* (51), 12823-12831.10.1021/jp0123029.
54. Garcia-Mateos, I.; Mercedes Velazquez, M.; Rodriguez, L. J., Critical micelle concentration determination in binary mixtures of ionic surfactants by deconvolution of conductivity/concentration curves. *Langmuir* **1990**, *6* (6), 1078-1083.10.1021/la00096a009.
55. Kjellin, U. R. M.; Reimer, J.; Hansson, P., An investigation of dynamic surface tension, critical micelle concentration, and aggregation number of three nonionic surfactants using nmr, time-resolved fluorescence quenching, and maximum bubble pressure tensiometry. *J. Colloid Interface Sci.* **2003**, *262* (2), 506-515.10.1016/S0021-9797(03)00168-1.
56. Söderman, O.; Stilbs, P.; Price, W. S., Nmr studies of surfactants. *Concepts Magn. Reson. Part A.* **2004**, *23A* (2), 121-135.10.1002/cmr.a.20022.
57. Vitiello, G.; Ciccarelli, D.; Ortona, O.; D'Errico, G., Microstructural characterization of lysophosphatidylcholine micellar aggregates: The structural basis for their use as biomembrane mimics. *J. Colloid Interface Sci.* **2009**, *336* (2), 827-33.10.1016/j.jcis.2009.04.008.
58. Tedeschi, A. M.; Busi, E.; Paduano, L.; Basosi, R.; D'Errico, G., Influence of the headgroup molecular structure on the anionic surfactant–pvp interaction studied by electron

paramagnetic resonance of a cationic nitroxide. *Phys. Chem. Chem. Phys.* **2003**, *5* (22), 5077-5083.10.1039/b305739a.

59. Mabrouk, M. M.; Hamed, N. A.; Mansour, F. R., Physicochemical and electrochemical methods for determination of critical micelle concentrations of surfactants: A comprehensive review. *Monatshefte für Chemie - Chemical Monthly* **2022**, *153* (2), 125-138.10.1007/s00706-022-02891-2.

60. Rosen, M. J., Surfactants and interfacial phenomena. *J. Wiley & Sons* **1989**, *New York*, .

61. Fu, J.; Cai, Z.; Gong, Y.; O'Reilly, S. E.; Hao, X.; Zhao, D., A new technique for determining critical micelle concentrations of surfactants and oil dispersants via uv absorbance of pyrene. *Colloids Surf. A: Physicochem. Eng. Asp.* **2015**, *484*, 1-8.10.1016/j.colsurfa.2015.07.039.

62. Li, N.; Luo, H.; Liu, S., A new method for the determination of the critical micelle concentration of triton x-100 in the absence and presence of beta-cyclodextrin by resonance rayleigh scattering technology. *Spectrochim Acta A Mol Biomol Spectrosc* **2004**, *60* (8-9), 1811-5.10.1016/j.saa.2003.09.018.

63. Lin, C.-E., Determination of critical micelle concentration of surfactants by capillary electrophoresis. *J. Chromatogr.* **2004**, *1037* (1-2), 467-478.10.1016/j.chroma.2003.11.059.

64. Ottaviani, G.; Wendelspiess, S.; Alvarez-Sanchez, R., Importance of critical micellar concentration for the prediction of solubility enhancement in biorelevant media. *Mol. Pharm.* **2015**, *12* (4), 1171-9.10.1021/mp5006992.

65. Zhu, Q.; Huang, L.; Su, J.; Liu, S., A sensitive and visible fluorescence-turn-on probe for the cmc determination of ionic surfactants. *Chem. Commun. (Camb)* **2014**, *50* (9), 1107-9.10.1039/c3cc45244a.

66. Cai, L.; Gochin, M.; Liu, K., A facile surfactant critical micelle concentration determination. *Chem. Commun. (Camb)* **2011**, 47 (19), 5527-9.10.1039/c1cc10605h.
67. Yu, D.; Huang, F.; Xu, H., Determination of critical concentrations by synchronous fluorescence spectrometry. *Anal. Methods* **2012**, 4 (1), 47-49.10.1039/c1ay05495c.
68. Cruz Barrios, E.; Annunziata, O., Determination of critical micelle concentration from the diffusion-driven dilution of micellar aqueous mixtures. *Langmuir* **2021**, 37 (8), 2855-2862.10.1021/acs.langmuir.1c00176.
69. Weinheimer, R. M.; Evans, D. F.; Cussler, E. L., Diffusion in surfactant solutions. *J. Colloid Interface Sci.* **1981**, 80 (2), 357-368.10.1016/0021-9797(81)90194-6.
70. Paduano, L.; Sartorio, R.; Vitagliano, V.; Costantino, L., Equilibrium and transport properties of aqueous pentaethyleneglycol-1-hexyl ether and sodium hexanesulfonate at 25°C. *J. Colloid Interface Sci.* **1997**, 189 (2), 189-198.10.1006/jcis.1997.4808.
71. Zhang, Y.; Furyk, S.; Bergbreiter, D. E.; Cremer, P. S., Specific ion effects on the water solubility of macromolecules: PnIPAM and the Hofmeister series. *J. Am. Chem. Soc.* **2005**, 127 (41), 14505-10.10.1021/ja0546424.
72. Shinoda, K.; Hutchinson, E., Pseudo-phase separation model for thermodynamic calculations on micellar solutions. *J. Phys. Chem.* **2002**, 66 (4), 577-582.10.1021/j100810a001.
73. Annunziata, O.; Costantino, L.; D'Errico, G.; Paduano, L.; Vitagliano, V. V., Transport properties for aqueous solution of sodium sulfonate surfactants. *J. Colloid Interface Sci.* **1999**, 216 (1), 8-15.10.1006/jcis.1999.6268.

74. Abdulagatov, I. M.; Zeinalova, A.; Azizov, N. D., Viscosity of aqueous Na_2SO_4 solutions at temperatures from 298 to 573K and at pressures up to 40MPa. *Fluid Phase Equilib.* **2005**, 227 (1), 57-70.10.1016/j.fluid.2004.10.028.
75. Crank, J., *The mathematics of diffusion*. 2nd ed ed.; Oxford University Press: Oxford, 1975.
76. Miller, D. G.; Albright, J. G., *Optical methods. In measurement of the transport properties of fluids: Experimental thermodynamics*. Blackwell Scientific Publications:: Oxford, 1991; Vol. III, p 272–294.
77. Cussler, E. L., *Diffusion: Mass transfer in fluid systems*. Cambridge University Press: Cambridge, 1997.
78. Rard, J. A.; Albright, J. G.; Miller, D. G.; Zeidler, M. E., Ternary mutual diffusion coefficients and densities of the system $\{\text{ZnCl}_2 + (1 - z_1)\text{Na}_2\text{SO}_4\}$ (aq) at 298.15 K and a total molarity of 0.5000 mol dm⁻³. *J. Chem. Soc., Faraday Trans.* **1996**, 92 (21), 4187-4197.10.1039/ft9969204187.
79. Annunziata, O.; Buzatu, D.; Albright, J. G., Protein diffusion coefficients determined by macroscopic-gradient rayleigh interferometry and dynamic light scattering. *Langmuir* **2005**, 21 (26), 12085-9.10.1021/la052147f.
80. Zhang, H. X.; Annunziata, O., Modulation of drug transport properties by multicomponent diffusion in surfactant aqueous solutions. *Langmuir* **2008**, 24 (19), 10680-10687.10.1021/la801636u.
81. Zhang, H.; Annunziata, O., Effect of macromolecular polydispersity on diffusion coefficients measured by rayleigh interferometry. *J. Phys, Chem. B* **2008**, 112 (12), 3633-43.10.1021/jp7104456.

82. Rusanov, A. I., The mass-action-law theory of micellization revisited. *Langmuir* **2014**, *30* (48), 14443-51.10.1021/la503770a.
83. Hao, L.-S.; Yang, N.; Xu, G.-Y.; Jia, Y.-F.; Liu, Q.; Nan, Y.-Q., Specific ion effects on the micellization of aqueous mixed cationic/anionic surfactant systems with various counterions. *Colloids Surf. A: Physicochem. Eng. Asp.* **2016**, *504*, 161-173.10.1016/j.colsurfa.2016.05.073.
84. Leaist, D. O., Binary diffusion of micellar electrolytes. *J. Colloid Interface Sci.* **1986**, *111* (1), 230-239.10.1016/0021-9797(86)90022-6.
85. Tiller, G. E.; Mueller, T. J.; Dockter, M. E.; Struve, W. G., Hydrogenation of triton x-100 eliminates its fluorescence and ultraviolet light absorption while preserving its detergent properties. *Anal. Biochem.* **1984**, *141* (1), 262-266.10.1016/0003-2697(84)90455-x.
86. Owoyomi, O.; Jide, I.; Akanni, M. S.; Soriyan, O. O.; Morakinyo, M. K., Interactions between sodium dodecylsulphate and triton x-100: Molecular properties and kinetics investigations. *J. Appl. Sci.* **2005**, *5* (4), 729-734.10.3923/jas.2005.729.734.
87. Cifuentes, A.; Bernal, J. L.; Diez-Masa, J. C., Determination of critical micelle concentration values using capillary electrophoresis instrumentation. *Anal. Chem.* **1997**, *69* (20), 4271-4274.10.1021/ac970696n.
88. Bandyopadhyay, P.; Ghosh, A. K.; Bandyopadhyay, S., Brij-micelle and polyacrylic acid interaction investigated by cu²⁺-induced pyrene fluorescence: Effect of brij-micelle structure. *Chem. Phys. Lett.* **2009**, *476* (4-6), 244-248.10.1016/j.cplett.2009.06.023.
89. Tripathi, S.; Brown, D. G., Effects of linear alkylbenzene sulfonate on the sorption of brij 30 and brij 35 onto aquifer sand. *Environ. Sci. amp; Technol.* **2008**, *42* (5), 1492-8.10.1021/es0720964.

90. Ray, A.; Nemethy, G., Effects of ionic protein denaturants on micelle formation by nonionic detergents. *J. Am. Chem. Soc.* **1971**, *93* (25), 6787-93.10.1021/ja00754a014.
91. Song, J.; Franck, J.; Pincus, P.; Kim, M. W.; Han, S., Specific ions modulate diffusion dynamics of hydration water on lipid membrane surfaces. *J. Am. Chem. Soc.* **2014**, *136* (6), 2642-9.10.1021/ja4121692.
92. McAfee, M. S.; Annunziata, O., Effects of salting-in interactions on macromolecule diffusiophoresis and salt osmotic diffusion. *Langmuir* **2015**, *31* (4), 1353-61.10.1021/la5046223.
93. Anderson, C. F.; Courtenay, E. S.; Record, M. T., Thermodynamic expressions relating different types of preferential interaction coefficients in solutions containing two solute components. *J. Phys. Chem. B* **2002**, *106* (2), 418-433.
94. Record, M. T.; Anderson, C. F., Interpretation of preferential interaction coefficients of nonelectrolytes and of electrolyte ions in terms of a two-domain model. *Biophys. J.* **1995**, *68* (3), 786-794.10.1016/s0006-3495(95)80254-7.
95. Timasheff, S. N., Protein-solvent preferential interactions, protein hydration, and the modulation of biochemical reactions by solvent components. *Proceedings of the National Academy of Sciences of the United States of America* **2002**, *99* (15), 9721-9726.10.1073/pnas.122225399.
96. Arakawa, T.; Timasheff, S. N., Preferential interactions of proteins with salts in concentrated solutions. *Biochemistry* **1982**, *21* (25), 6545-52.10.1021/bi00268a034.
97. Vitagliano, V.; Sartorio, R.; Scala, S.; Spaduzzi, D., Diffusion in a ternary system and the critical mixing point. *J. Solution Chem.* **1978**, *7* (8), 605-622.10.1007/bf00646038.

98. Lomakin, A.; Asherie, N.; Benedek, G. B., Monte carlo study of phase separation in aqueous protein solutions. *J. Chem. Phys* **1996**, *104* (4), 1646-1656.10.1063/1.470751.
99. Shaw, D. J., Kinetic properties. In *Introduction to colloids and surface science*, 4th ed.; Elsevier Science Ltd: 1992; pp 23-30.
100. Mörters, P.; Peres, Y., *Brownian motion*. Cambridge University Press: 2010.
101. Miller, D. G.; Vitagliano, V.; Sartorio, R., Some comments on multicomponent diffusion - negative main term diffusion-coefficients, 2nd law constraints, solvent choices, and reference frame transformations. *Journal of Physical Chemistry* **1986**, *90* (8), 1509-1519.10.1021/j100399a010.
102. Miller, D. G., Thermodynamics of irreversible processes. The experimental verification of the onsager reciprocal relations. *Chem. Rev.* **1960**, *60* (1), 15-37.10.1021/cr60203a003.
103. Tyrrell, H. J. V.; Harris, K. R., *Diffusion in liquids*. Butterworths: London, 1984.
104. Miller, D. G., The onsager relations; experimental evidence. In *Foundations of continuum thermodynamics*, Domingos, J. J. D.; Nina, M. N. R.; Whitelaw, J. H., Eds. Macmillan Education UK: London, 1973; pp 185-214.
105. Miller, D. G., Ternary isothermal diffusion and the validity of the onsager reciprocity relations. *J. Phys. Chem.* **1959**, *63* (4), 570-578.10.1021/j150574a030.
106. Annunziata, O.; Fahim, A., A unified description of macroion diffusiophoresis, salt osmotic diffusion and collective diffusion coefficient. *Int. J. Heat Mass Transf.* **2020**, *163*, 11.10.1016/j.ijheatmasstransfer.2020.120436.
107. Lechlitner, L. R.; Annunziata, O., Macromolecule diffusiophoresis induced by concentration gradients of aqueous osmolytes. *Langmuir* **2018**, *34* (32), 9525-9531.10.1021/acs.langmuir.8b02065.

108. Rard, J. A.; Clegg, S. L.; Palmer, D. A., Isopiestic determination of the osmotic coefficients of $\text{Na}_2\text{SO}_4(\text{aq})$ at 25 and 50°C, and representation with ion-interaction (Pitzer) and mole fraction thermodynamic models. *J. Solution Chem.* **2000**, *29* (1), 1-49.10.1023/a:1005182316790.
109. Pusey, P. N.; Tough, R. J. A., *Particle interactions, in dynamic light scattering. Applications of photon correlation spectroscopy*. Plenum Press: New York, 1985.
110. Molina-Bolívar, J. A.; Aguiar, J.; Ruiz, C. C., Growth and hydration of Triton X-100 micelles in monovalent alkali salts: A light scattering study. *J. Phys. Chem. B* **2002**, *106* (4), 870-877.10.1021/jp0119936.
111. Corti, M.; Degiorgio, V., Micellar properties and critical fluctuations in aqueous solutions of nonionic amphiphiles. *J. Phys. Chem.* **1981**, *85* (10), 1442-1445.10.1021/j150610a033.
112. Derjaguin, B. V.; Sidorenkov, G.; Zubashchenko, E.; Kiseleva, E., Kinetic phenomena in the boundary layers of liquids 1. The capillary osmosis. *Prog. Surf. Sci.* **1993**, *43* (1-4), 138-152.10.1016/0079-6816(93)90023-o.
113. Cruz Barrios, E.; Krause, T. C.; Annunziata, O., Salt-induced diffusiophoresis of a nonionic micelle: Roles of salting out and proximity to surfactant cloud point. *J. Mol. Liq.* **2022**, *359*, 10.1016/j.molliq.2022.119271.
114. Abecassis, B.; Cottin-Bizonne, C.; Ybert, C.; Ajdari, A.; Bocquet, L., Boosting migration of large particles by solute contrasts. *Nat. Mater.* **2008**, *7* (10), 785-9.10.1038/nmat2254.
115. Prieve, D. C.; Malone, S. M.; Khair, A. S.; Stout, R. F.; Kanj, M. Y., Diffusiophoresis of charged colloidal particles in the limit of very high salinity. *Proc. Natl. Acad. Sci. U. S. A.* **2019**, *116* (37), 18257-18262.10.1073/pnas.1701391115.

116. Shin, S., Diffusiophoretic separation of colloids in microfluidic flows. *Phys. Fluids* **2020**, *32* (10), 15.10.1063/5.0023415.
117. Fan, L.; Lee, E., Diffusiophoresis of a highly charged conducting fluid droplet. *Phys. Fluids* **2022**, *34* (6), 10.1063/5.0098144.
118. Fan, L.; Wu, Y.; Jian, E.; Tseng, J.; Wan, R.; Tseng, A.; Lin, J.; Lee, E., Diffusiophoresis of a highly charged dielectric fluid droplet induced by diffusion potential. *Phys. Fluids* **2022**, *34* (4), 042003.10.1063/5.0086282.
119. Fan, L.; Jian, E.; Chang, W. C.; Wu, Y.; Lin, J.; Tseng, A.; Tseng, J.; Wan, R.; Yu, A.; Lee, E., Diffusiophoresis in suspensions of highly charged soft particles. *Electrophoresis* **2022**, 10.1002/elps.202100380.
120. Tsai, M. Y.; Wu, Y.; Fan, L.; Jian, E.; Lin, J.; Tseng, J.; Tseng, A.; Wan, R.; Lee, E., Analytical solution to dielectric droplet diffusiophoresis under debye-huckel approximation. *Electrophoresis* **2022**, *43* (3), 495-500.10.1002/elps.202100264.
121. Alessio, B. M.; Shim, S.; Gupta, A.; Stone, H. A., Diffusioosmosis-driven dispersion of colloids: A Taylor dispersion analysis with experimental validation. *J. Fluid. Mech.* **2022**, *942*, 10.1017/jfm.2022.321.
122. Shi, N.; Abdel-Fattah, A., Droplet migration into dead-end channels at high salinity enhanced by micelle gradients of a zwitterionic surfactant. *Phys. Rev. Fluids* **2021**, *6* (5), 053103.10.1103/PhysRevFluids.6.053103.
123. Jotkar, M.; Cueto-Felgueroso, L., Particle separation through diverging nanochannels via diffusiophoresis and diffusioosmosis. *Phys. Rev. Appl.* **2021**, *16* (6), 10.1103/PhysRevApplied.16.064067.

124. Seo, M.; Park, S.; Lee, D.; Lee, H.; Kim, S. J., Continuous and spontaneous nanoparticle separation by diffusiophoresis. *Lab Chip* **2020**, *20* (22), 4118-4127.10.1039/d0lc00593b.
125. Lei, L.; Wang, S.; Zhou, X.; Ghellab, S. E.; Lin, G.; Gao, Y., Self-organization of binary colloidal mixtures via diffusiophoresis. *Front. Chem.* **2022**, *10*, 803906.10.3389/fchem.2022.803906.
126. Rees-Zimmerman, C. R.; Routh, A. F., Stratification in drying films: A diffusion–diffusiophoresis model. *J. Fluid. Mech.* **2021**, *928*, 10.1017/jfm.2021.800.
127. Tinkler, J. D.; Scacchi, A.; Kothari, H. R.; Tulliver, H.; Argai, M.; Archer, A. J.; Martin-Fabiani, I., Evaporation-driven self-assembly of binary and ternary colloidal polymer nanocomposites for abrasion resistant applications. *J. Colloid Interface Sci.* **2021**, *581* (Pt B), 729-740.10.1016/j.jcis.2020.08.001.
128. Zhou, X.; Wang, S.; Xian, L.; Shah, Z. H.; Li, Y.; Lin, G.; Gao, Y., Ionic effects in ionic diffusiophoresis in chemically driven active colloids. *Phys. Rev. Lett.* **2021**, *127* (16), 168001.10.1103/PhysRevLett.127.168001.
129. Daddi-Moussa-Ider, A.; Vilfan, A.; Golestanian, R., Diffusiophoretic propulsion of an isotropic active colloidal particle near a finite-sized disk embedded in a planar fluid–fluid interface. *J. Fluid. Mech.* **2022**, *940*, 10.1017/jfm.2022.232.
130. Zhang, J.; Chen, Z.; Kankala, R. K.; Wang, S. B.; Chen, A. Z., Self-propelling micro-/nano-motors: Mechanisms, applications, and challenges in drug delivery. *Int. J. Pharm.* **2021**, *596*, 120275.10.1016/j.ijpharm.2021.120275.
131. McAfee, M. S.; Annunziata, O., Effect of particle size on salt-induced diffusiophoresis compared to brownian mobility. *Langmuir* **2014**, *30* (17), 4916-4923.10.1021/la500982u.

132. Jungwirth, P.; Cremer, P. S., Beyond hofmeister. *Nat. Chem.* **2014**, *6* (4), 261-3.10.1038/nchem.1899.
133. Lightfoot, E. N.; Cussler, E. L.; Rettig, R. L., Applicability of the stefan-maxwell equations to multicomponent diffusion in liquids. *AIChE Journal* **1962**, *8* (5), 708-710.10.1002/aic.690080530.
134. Gosting, L. J., Measurement and interpretation of diffusion coefficients of proteins. *Adv. Protein Chem.* **1956**, *11*, 429-554.10.1016/s0065-3233(08)60425-8.
135. Krishna, R., Diffusing uphill with james clerk maxwell and josef stefan. *Chem. Eng. Sci.* **2019**, *195*, 851-880.10.1016/j.ces.2018.10.032.
136. Dong, R. H.; Hao, J. C., Complex fluids of poly(oxyethylene) monoalkyl ether nonionic surfactants. *Chem. Rev.* **2010**, *110* (9), 4978-5022.10.1021/cr9003743.
137. Na, G. C.; Yuan, B. O.; Stevens, H. J., Jr.; Weekley, B. S.; Rajagopalan, N., Cloud point of nonionic surfactants: Modulation with pharmaceutical excipients. *Pham. Res.* **1999**, *16* (4), 562-8.10.1023/a:1018831415131.
138. Weckstrom, K.; Papageorgiou, A. C., Lower consolute boundaries of the nonionic surfactant c8e5 in aqueous alkali halide solutions: An approach to reproduce the effects of alkali halides on the cloud-point temperature. *J. Colloid Interface Sci.* **2007**, *310* (1), 151-62.10.1016/j.jcis.2007.01.045.
139. Santos-Ebinuma, V. C.; Lopes, A. M.; Converti, A.; Pessoa, A.; Rangel-Yagui, C. d. O., Behavior of triton x-114 cloud point in the presence of inorganic electrolytes. *Fluid Phase Equilib.* **2013**, *360*, 435-438.10.1016/j.fluid.2013.09.053.
140. Schott, H., Comparing the surface chemical properties and the effect of salts on the cloud point of a conventional nonionic surfactant, octoxynol 9 (triton x-100), and of its oligomer,

tyloxapol (triton wr-1339). *J. Colloid Interface Sci.* **1998**, *205* (2), 496-502.10.1006/jcis.1998.5721.

141. Dharaiya, N.; Aswal, V. K.; Bahadur, P., Characterization of triton x-100 and its oligomer (tyloxapol) micelles vis-à-vis solubilization of bisphenol a by spectral and scattering techniques. *Colloids Surf. A: Physicochem. Eng. Asp.* **2015**, *470*, 230-239.10.1016/j.colsurfa.2015.01.053.

142. Regev, O.; Zana, R., Aggregation behavior of tyloxapol, a nonionic surfactant oligomer, in aqueous solution. *J. Colloid Interface Sci.* **1999**, *210* (1), 8-17.10.1006/jcis.1998.5776.

143. Leaist, D. G.; Hao, L., Comparison of diffusion-coefficients of multicomponent solutions from light-scattering and macroscopic gradient techniques - sodium dodecyl-sulfate micelles in aqueous salt-solutions. *J. Phys. Chem.* **1993**, *97* (29), 7763-7768.10.1021/j100131a054.

144. Aniansson, E. A. G.; Wall, S. N.; Almgren, M.; Hoffmann, H.; Kielmann, I.; Ulbricht, W.; Zana, R.; Lang, J.; Tondre, C., Theory of kinetics of micellar equilibria and quantitative interpretation of chemical relaxation studies of micellar solutions of ionic surfactants. *J. Phys. Chem.* **1976**, *80* (9), 905-922.10.1021/j100550a001.

145. Leaist, D. G., Relating multicomponent mutual diffusion and intradiffusion for associating solutes. Application to coupled diffusion in water-in-oil microemulsions. *Phys. Chem. Chem. Phys.* **2002**, *4* (19), 4732-4739.10.1039/b205281b.

146. Leaist, D. G.; MacEwan, K., Coupled diffusion of mixed ionic micelles in aqueous sodium dodecyl sulfate + sodium octanoate solutions. *J. Phys. Chem. B* **2001**, *105* (3), 690-695.10.1021/jp003131v.

147. Jungwirth, P.; Cremer, P. S., Beyond hofmeister. *Nat. Chem.* **2014**, *6* (4), 261-3.10.1038/nchem.1899.

148. Rard, J. A.; Miller, D. G., The mutual diffusion coefficients of $\text{Na}_2\text{SO}_4\cdot\text{H}_2\text{O}$ and $\text{MgSO}_4\cdot\text{H}_2\text{O}$ at 25°C from Rayleigh interferometry. *J. Solution Chem.* **1979**, 8 (10), 755-766.10.1007/bf00648779.
149. Miller, D. G.; Albright, J. G., Optical methods. In *Measurement of the transport properties of fluids: Experimental thermodynamics*, Wakeham, W. A.; Nagashima, A.; Sengers, J. V., Eds. Blackwell Scientific Publications: Oxford, U.K., 1991; Vol. III, pp 272-294.
150. Albright, J. G.; Annunziata, O.; Miller, D. G.; Paduano, L.; Pearlstein, A. J., Precision measurements of binary and multicomponent diffusion coefficients in protein solutions relevant to crystal growth: Lysozyme chloride in water and aqueous NaCl at pH 4.5 and 25 °C. *J. Am. Chem. Soc.* **1999**, 121 (14), 3256-3266.10.1021/ja9834834.
151. Miller, D. G., A method for obtaining multicomponent diffusion coefficients directly from Rayleigh and Gouy fringe position data. *J. Phys. Chem.* **1988**, 92 (14), 4222-4226.10.1021/j100325a045.
152. McAfee, M. S.; Annunziata, O., Cross-diffusion in a colloid–polymer aqueous system. *Fluid Phase Equilib.* **2013**, 356, 46-55.10.1016/j.fluid.2013.07.014.
153. Javadian, S.; Kakemam, J., Intermicellar interaction in surfactant solutions; a review study. *J. Mol. Liq.* **2017**, 242, 115-128.10.1016/j.molliq.2017.06.117.
154. Robson, R. J.; Dennis, E. A., The size, shape, and hydration of nonionic surfactant micelles. Triton X-100. *J. Phys. Chem.* **1976**, 81 (11), 1075-1078.10.1021/j100526a010.
155. Abdulagatov, I. M.; Azizov, N. D.; Zeinalova, A. B., Viscosities, densities, apparent and partial molar volumes of concentrated aqueous MgSO_4 solutions at high temperatures and high pressures. *Phys. Chem. Liquids* **2007**, 45 (2), 127-148.10.1080/00319100601089802.

156. Annunziata, O.; Buzatu, D.; Albright, J. G., Effect of lysozyme proteins on the mutual-diffusion coefficient of sodium chloride in water. *Journal of Chemical and Engineering Data* **2011**, *56* (12), 4849-4852.10.1021/je200807y.
157. Moulins, J. R.; MacNeil, J. A.; Leaist, D. G., Thermodynamic stability and the origins of incongruent and strongly coupled diffusion in solutions of micelles, solubilizates, and microemulsions. *J. Chem. Eng. Data* **2009**, *54* (9), 2371-2380.10.1021/je800767e.
158. Janzen, T.; Vrabec, J., Diffusion coefficients of a highly nonideal ternary liquid mixture: Cyclohexane–toluene–methanol. *Ind. Eng. Chem. Res.* **2018**, *57* (48), 16508-16517.10.1021/acs.iecr.8b04385.
159. Lo, P. Y.; Myerson, A. S., Ternary diffusion coefficients in metastable solutions of glycine-valine-h₂o. *AIChE Journal* **1989**, *35* (4), 676-678.10.1002/aic.690350422.
160. Buzatu, F. D.; Lungu, R. P.; Buzatu, D.; Sartorio, R.; Paduano, L., Spinodal composition of the system water + chloroform + acetic acid at 25 °c. *J. Solution Chem.* **2009**, *38* (4), 403-415.10.1007/s10953-009-9384-5.
161. Kelley, C. T., *Solving nonlineat equations with newton's method*. 1st ed.; SIAM: Philadelphia, PA, 2003; p 2-25.
162. Perrin, F., Mouvement brownien d'un ellipsoide (ii). Rotation libre et dépolariation des fluorescences. Translation et diffusion de molécules ellipsoidales. *J. Phys. Radium* **1936**, *7* (1), 1-11..
163. Neurath, H., The apparent shape of protein molecules. *J. Am. Chem. Soc.* **2002**, *61* (7), 1841-1844.10.1021/ja01876a060.
164. Velegol, D.; Garg, A.; Guha, R.; Kar, A.; Kumar, M., Origins of concentration gradients for diffusiophoresis. *Soft Matter* **2016**, *12* (21), 4686-4703.10.1039/c6sm00052e.

165. Prieve, D. C.; Malone, S. M.; Khair, A. S.; Stout, R. F.; Kanj, M. Y., Diffusiophoresis of charged colloidal particles in the limit of very high salinity. *Proceedings of the National Academy of Sciences* **2019**, *116* (37), 18257-18262.10.1073/pnas.1701391115.
166. Shah, A.; Shahzad, S.; Munir, A.; Nadagouda, M. N.; Khan, G. S.; Shams, D. F.; Dionysiou, D. D.; Rana, U. A., Micelles as soil and water decontamination agents. *Chem. Rev.* **2016**, *116* (10), 6042-6074.10.1021/acs.chemrev.6b00132.
167. Schott, H.; Han, S. K., Effect of inorganic additives on solutions of nonionic surfactants ii. *J. Pharm. Sci.* **1975**, *64* (4), 658-64.10.1002/jps.2600640419.
168. Schott, H., Effect of inorganic additives on solutions of nonionic surfactants. *J. Colloid Interface Sci.* **1997**, *189* (1), 117-122.10.1006/jcis.1997.4822.

APPENDIX A

Table A1. DLS diffusion coefficients of tyloxapol in aqueous solutions of Na₂SO₄ at 25 °C

	$C_s = 0 \text{ M}$	$C_s = 0.10 \text{ M}$	$C_s = 0.20 \text{ M}$	$C_s = 0.30 \text{ M}$	$C_s = 0.45 \text{ M}$	$C_s = 0.60 \text{ M}$	$C_s = 0.65 \text{ M}$
C_M / M	$\mathcal{D}_M / 10^{-11} \text{ m}^2 \cdot \text{s}^{-1}$	$\mathcal{D}_M / 10^{-11} \text{ m}^2 \cdot \text{s}^{-1}$	$\mathcal{D}_M / 10^{-11} \text{ m}^2 \cdot \text{s}^{-1}$	$\mathcal{D}_M / 10^{-11} \text{ m}^2 \cdot \text{s}^{-1}$	$\mathcal{D}_M / 10^{-11} \text{ m}^2 \cdot \text{s}^{-1}$	$\mathcal{D}_M / 10^{-11} \text{ m}^2 \cdot \text{s}^{-1}$	$\mathcal{D}_M / 10^{-11} \text{ m}^2 \cdot \text{s}^{-1}$
0.20	6.71±0.09	6.66±0.06	6.09±0.05	5.45±0.04	4.02±0.03	2.62±0.02	2.19±0.02
0.40	6.73±0.04	6.57±0.02	6.10±0.08	5.27±0.01	3.56±0.01	2.19±0.01	1.81±0.01
0.70	6.78±0.03	6.49±0.05	5.92±0.07	4.97±0.04	3.17±0.02	1.80±0.01	1.52±0.04
1.00	6.82±0.02	6.39±0.03	5.80±0.02	4.74±0.02	2.67±0.01	-	1.11±0.01

Table A2. DLS diffusion coefficients of tyloxapol in aqueous solutions of MgSO₄ at 25 °C

	$C_s = 0 \text{ M}$	$C_s = 0.10 \text{ M}$	$C_s = 0.20 \text{ M}$	$C_s = 0.30 \text{ M}$	$C_s = 0.50 \text{ M}$	$C_s = 0.60 \text{ M}$	$C_s = 0.69 \text{ M}$
C_M / M	$\mathcal{D}_M / 10^{-11} \text{ m}^2 \cdot \text{s}^{-1}$	$\mathcal{D}_M / 10^{-11} \text{ m}^2 \cdot \text{s}^{-1}$	$\mathcal{D}_M / 10^{-11} \text{ m}^2 \cdot \text{s}^{-1}$	$\mathcal{D}_M / 10^{-11} \text{ m}^2 \cdot \text{s}^{-1}$	$\mathcal{D}_M / 10^{-11} \text{ m}^2 \cdot \text{s}^{-1}$	$\mathcal{D}_M / 10^{-11} \text{ m}^2 \cdot \text{s}^{-1}$	$\mathcal{D}_M / 10^{-11} \text{ m}^2 \cdot \text{s}^{-1}$
0.20	6.71±0.09	6.76±0.05	6.22±0.05	5.55±0.03	4.23±0.03	3.03±0.02	2.26±0.02
0.3	-	-	6.19±0.05	5.43±0.01	3.93±0.03	-	-
0.40	6.73±0.04	6.68±0.05	6.06±0.05	5.38±0.01	3.80±0.03	2.54±0.01	1.92±0.01
0.5	-	-	-	5.24±0.02	-	-	-
0.70	6.78±0.03	6.59±0.02	5.88±0.02	5.15±0.02	3.51±0.02	2.15±0.01	1.58±0.01
0.75	-	-	5.85±0.02	-	-	-	-
1.00	6.82±0.02	6.50±0.03	5.80±0.02	-	3.25±0.01	2.02±0.01	1.44±0.01

	$C_s = 0.71 \text{ M}$	$C_s = 0.73 \text{ M}$
C_M / M	$\mathcal{D}_M / 10^{-11} \text{ m}^2 \cdot \text{s}^{-1}$	$\mathcal{D}_M / 10^{-11} \text{ m}^2 \cdot \text{s}^{-1}$
0.20	2.07±0.02	2.04±0.02
0.40	1.75±0.01	1.84±0.01
0.70	1.46±0.01	1.58±0.01
1.00	1.35±0.02	1.45±0.01

APPENDIX B

Table B1. Solution preparation data for the binary systems Na₂SO₄-water at 25 °C.

Na ₂ SO ₄	0.1 M	0.2 M	0.3 M	0.5 M	0.6 M	0.64 M
$\rho_0(\text{dm}^3\text{mol}^{-1})$	1.00955	1.02209	1.03426	1.05831	1.07023	1.07443
\bar{C}_s/M	0.1000	0.1999	0.3000	0.4993	0.5982	0.6161
$\Delta C_s / \text{M}$	0.057919	0.057740	0.057719	0.059629	0.056468	0.057567
$\rho_{\text{top}} / \text{g dm}^{-3}$	1.006017	1.018489	1.030754	1.053179	1.068858	1.030741
$\rho_{\text{bot}} / \text{g dm}^{-3}$	1.013362	1.025543	1.037829	1.060303	1.075370	1.037832

Table B2. Solution preparation data for the binary systems MgSO₄-water at 25 °C.

MgSO ₄	0.1 M	0.3 M	0.5 M	0.65 M
$\rho_0(\text{dm}^3\text{mol}^{-1})$	1.00912	1.03245	1.05569	1.07238
\bar{C}_s/M	0.1000	0.3001	0.5000	0.6499
$\Delta C_s / \text{M}$	0.048222	0.047481	0.048152	0.048075
$\rho_{\text{top}} / \text{g dm}^{-3}$	1.006239	1.030009	1.053157	1.069629
$\rho_{\text{bot}} / \text{g dm}^{-3}$	1.012034	1.035528	1.058459	1.074799

Table B3. Solution preparation data for the binary systems tyloxapol-water at 25 °C.

Tyloxapol	1.0 mM
ρ_0 (dm ³ mol ⁻¹)	0.99772
\bar{C}_M /M	0.1000
ΔC_M / mM	1.5396
ρ_{top} / g dm ⁻³	0.997126
ρ_{bot} / g dm ⁻³	0.997868

Table B4. Solution preparation data for the ternary system tyloxapol-Na₂SO₄-water at C_s=0.1 M and 25 °C.

Exp N⁰	$\alpha_0(1)$	$\alpha_0(2)$	$\alpha_1(1)$	$\alpha_1(2)$
\bar{C}_M /mM	0.9999	0.9999	0.9999	0.9999
\bar{C}_S /M	0.09997	0.09999	0.09988	0.1000
ΔC_M / mM	-0.000245	-0.000169	1.692282	1.692243
ΔC_S / M	0.057858	0.057879	0.000246	-0.000021
ρ_{top} / g dm ⁻³	1.006514	1.006472	1.009754	1.009743
ρ_{bot} / g dm ⁻³	1.013788	1.013803	1.010685	1.010669

Table B5. Solution preparation data for the ternary system tyloxapol-Na₂SO₄-water at C_s=0.2 M and 25 °C.

Exp N ⁰	$\alpha_0(1)$	$\alpha_0(2)$	$\alpha_1(1)$	$\alpha_1(2)$
\bar{C}_M / mM	0.1000	0.9999	0.9999	0.9999
\bar{C}_S / M	0.2000	0.1999	0.1999	0.1999
$\Delta C_M / \text{mM}$	-0.000420	-0.000387	1.692240	1.692262
$\Delta C_S / \text{M}$	0.057817	0.057816	0.000019	0.000006
$\rho_{\text{top}} / \text{g dm}^{-3}$	1.019025	1.019056	1.022142	1.022140
$\rho_{\text{bot}} / \text{g dm}^{-3}$	1.026126	1.026178	1.023056	1.023056

Table B6. Solution preparation data for the ternary system tyloxapol-Na₂SO₄-water at C_s=0.3 M and 25 °C.

Exp N ⁰	$\alpha_0(1)$	$\alpha_0(2)$	$\alpha_1(1)$	$\alpha_1(2)$
\bar{C}_M / mM	0.1000	0.1000	0.9999	0.9999
\bar{C}_S / M	0.3000	0.3000	0.3000	0.3000
$\Delta C_M / \text{mM}$	-0.000525	-0.000498	1.692275	1.692272
$\Delta C_S / \text{M}$	0.057742	0.057754	-0.000016	-0.000013
$\rho_{\text{top}} / \text{g dm}^{-3}$	1.031341	1.031395	1.034395	1.034395
$\rho_{\text{bot}} / \text{g dm}^{-3}$	1.038313	1.038395	1.035248	1.035248

Table B7. Solution preparation data for the ternary system tyloxapol-Na₂SO₄-water at C_s=0.5 M and 25 °C.

Exp N ⁰	$\alpha_0(1)$	$\alpha_0(2)$	$\alpha_1(1)$	$\alpha_1(2)$
\bar{C}_M / mM	0.9996	0.9996	0.9995	0.9997
\bar{C}_S / M	0.4998	0.4999	0.4998	0.4999
$\Delta C_M / \text{mM}$	0.000249	0.000206	1.691382	1.691774
$\Delta C_S / \text{M}$	0.059630	0.059610	-0.010095	-0.010004
$\rho_{\text{top}} / \text{g dm}^{-3}$	1.054975	1.055051	1.058699	1.058735
$\rho_{\text{bot}} / \text{g dm}^{-3}$	1.061963	1.061994	1.058231	1.058467

Table B8. Solution preparation data for the ternary system tyloxapol-Na₂SO₄-water at C_s=0.60 M and 25 °C.

Exp N ⁰	$\alpha_0(1)$	$\alpha_0(2)$	$\alpha_1(1)$	$\alpha_1(2)$
\bar{C}_M / mM	0.9998	1.0000	1.0000	1.0000
\bar{C}_S / M	0.5999	0.6000	0.6000	0.6000
$\Delta C_M / \text{mM}$	0.000166	0.000204	1.692421	1.692417
$\Delta C_S / \text{M}$	0.052725	0.052761	-0.00998	-0.010006
$\rho_{\text{top}} / \text{g dm}^{-3}$	1.067034	1.067257	1.070496	1.058735
$\rho_{\text{bot}} / \text{g dm}^{-3}$	1.073159	1.073424	1.070246	1.058467

Table B9. Solution preparation data for the ternary system tyloxapol-Na₂SO₄-water at C_s=0.64 M and 25 °C.

Exp N ⁰	$\alpha_0(1)$	$\alpha_0(2)$	$\alpha_1(1)$	$\alpha_1(2)$
\bar{C}_M/mM	0.9998	0.9998	0.9999	0.9999
\bar{C}_S/M	0.6399	0.6399	0.6399	0.6399
$\Delta C_M / \text{mM}$	-0.000008	0.000038	1.692098	1.692090
$\Delta C_S / M$	0.059514	0.059541	-0.010002	-0.010002
$\rho_{\text{top}} / \text{g dm}^{-3}$	1.071424	1.071362	1.075066	1.075065
$\rho_{\text{bot}} / \text{g dm}^{-3}$	1.078311	1.078301	1.074781	1.074781

Table B10. Solution preparation data for the ternary system tyloxapol-MgSO₄-water at C_s=0.10 M and 25 °C.

Exp N ⁰	$\alpha_0(1)$	$\alpha_0(2)$	$\alpha_1(1)$	$\alpha_1(2)$
\bar{C}_M/mM	1.0000	1.0000	1.0000	1.0000
\bar{C}_S/M	0.1000	0.1000	0.1000	0.1000
$\Delta C_M / \text{mM}$	-0.000190	0.000220	1.539943	1.539726
$\Delta C_S / M$	0.048215	0.048215	0.000078	0.000068
$\rho_{\text{top}} / \text{g dm}^{-3}$	1.006811	1.006811	1.009232	1.009224
$\rho_{\text{bot}} / \text{g dm}^{-3}$	1.012368	1.012368	1.010199	1.010097

Table B11. Solution preparation data for the ternary system tyloxapol-MgSO₄-water at C_s=0.30 M and 25 °C.

Exp N ⁰	$\alpha_0(1)$	$\alpha_0(2)$	$\alpha_1(1)$	$\alpha_1(2)$
\bar{C}_M/mM	0.9996	0.9995	0.9998	0.9998
\bar{C}_S/M	0.2999	0.2999	0.2999	0.2999
$\Delta C_M/\text{mM}$	0.000009	-0.000055	1.538380	1.538389
$\Delta C_S/\text{M}$	0.0482007	0.048178	0.000188	0.000185
$\rho_{\text{top}}/\text{g dm}^{-3}$	1.030484	1.030429	1.032832	1.032855
$\rho_{\text{bot}}/\text{g dm}^{-3}$	1.036078	1.035955	1.033637	1.033646

Table B12. Solution preparation data for the ternary system tyloxapol-MgSO₄-water at C_s=0.50 M and 25 °C.

Exp N ⁰	$\alpha_0(1)$	$\alpha_0(2)$	$\alpha_1(1)$	$\alpha_1(2)$
\bar{C}_M/mM	1.0000	1.0000	1.0000	1.0000
\bar{C}_S/M	0.5002	0.50023	0.5001	0.5001
$\Delta C_M/\text{mM}$	-0.000181	-0.000077	1.954776	1.954810
$\Delta C_S/\text{M}$	0.048148	0.048183	-0.012624	-0.012621
$\rho_{\text{top}}/\text{g dm}^{-3}$	1.053405	1.053425	1.055975	1.055974
$\rho_{\text{bot}}/\text{g dm}^{-3}$	1.058683	1.058781	1.055554	1.055554

Table B13. Solution preparation data for the ternary system tyloxapol-MgSO₄-water at C_s=0.65 M and 25 °C.

Exp N ⁰	$\alpha_0(1)$	$\alpha_0(2)$	$\alpha_1(1)$	$\alpha_1(2)$
\bar{C}_M / mM	1.0000	1.0000	1.0000	1.0000
\bar{C}_S / M	0.6503	0.6503	0.6503	0.650255
$\Delta C_M / \text{mM}$	-0.000011	-0.000006	1.955217	1.955258
$\Delta C_S / \text{M}$	0.048241	0.048238	-0.012523	-0.012527
$\rho_{\text{top}} / \text{g dm}^{-3}$	1.070247	1.070247	1.073123	1.073123
$\rho_{\text{bot}} / \text{g dm}^{-3}$	1.075637	1.075638	1.072707	1.072708

APPENDIX C

Table C1. Thermodynamic and transport properties of aqueous Na₂SO₄ at 25 °C.

C_s / M	$\bar{V}_s / \text{cm}^3 \cdot \text{mol}^{-1}$	y_s	$D_{s,v} / 10^{-11} \text{m}^2 \cdot \text{s}^{-1}$	$r / \%$	η_r
0.10	17.1	0.735	983	-1.0	1.045
0.20	19.6	0.696	923	-1.1	1.090
0.30	21.5	0.671	874	-1.1	1.138
0.45	-	-	-	-	1.216
0.50	24.5	0.636	794	-1.6	1.244
0.60	25.7	0.623	754	-1.2	1.301
0.64	26.2	0.619	747	-1.6	1.325
0.65	-	-	-	-	1.331

Table C2. Thermodynamic and transport properties of aqueous MgSO₄ at 25 °C.

C_s / M	$\bar{V}_s / \text{cm}^3 \cdot \text{mol}^{-1}$	y_s	$D_{s,v} / 10^{-11} \text{m}^2 \cdot \text{s}^{-1}$	$r / \%$	η_r
0.10	1.17	0.538	572	-1.5	1.072
0.30	4.65	0.498	496	-1.5	1.221
0.50	7.14	0.500	454	-2.6	1.399
0.65	8.73	0.518	429	-1.6	1.568

VITA

Eliandreina Cruz Barrios was born February 10, 1986, in Valencia, Venezuela. She is the daughter of Susana Beatriz and Jorge Luis. She received her Bachelor of Science degree with major in Chemistry from University of Carabobo, Venezuela, in 2008.

In 2014 she received her Master of Science degree in Chemistry from the Venezuelan Institute of Scientific Research (IVIC) in 2014. She joined IVIC as a research associate for 5 years until her enrollment as a graduate student at Texas Christian University in July 2017, where she received her Doctor of Philosophy degree in December 2022. While working on her doctorate in Chemistry, she held a Teaching Assistantship 2017-2020 and a Research Assistantship 2020-2022. She was awarded a SERC graduate research grant in 2021 and two simultaneous Outstanding Teaching Awards for her contributions in the Laboratory of General Chemistry and the Laboratory of Physical Chemistry I. Starting February 2023, she will be working as a Postdoc in the Department of Materials Science and Engineering at Texas A&M, College Station, TX. She is a member of the American Chemical Society.

ABSTRACT

SALT-INDUCED DIFFUSIOPHORESIS OF A NON-IONIC MICELLE IN WATER

by Eliandreina Cruz Barrios, Ph.D., 2022

Department of Chemistry and Biochemistry

Texas Christian University

Dissertation Advisor: Onofrio Annunziata, Professor of Chemistry

Salt-induced diffusiophoresis is the migration of a colloidal particle caused by salt concentration gradients in water. A common example of colloidal particles is represented by those with interfacial properties governed by polyethylene glycol (PEG) functionalities. This dissertation provides the first report showing salt-induced diffusiophoresis of a neutral PEG-based colloidal particle. The nonionic micelle of tyloxapol, a commercially available polyoxyethylene surfactant that is an oligomer of Triton X-100, was chosen in this investigation. This dissertation also includes the development of a new single-sample method for the determination of surfactant critical micelle concentration (cmc) based on the diffusion-driven dilution of a micellar solution. This method was sufficiently precise to show that the cmc of non-ionic surfactant Triton X-100 decreases as concentration of salting-out salt Na_2SO_4 increases.

Salt-induced diffusiophoresis of Tyloxapol micelles in water was experimentally characterized for two salt cases, Na_2SO_4 and MgSO_4 . Specifically, multicomponent-diffusion coefficients were measured at 25 °C for the ternary tyloxapol-salt-water system using Rayleigh interferometry. Measurements of cloud points allowed us to establish the experimental

conditions for our diffusiophoresis studies. Dynamic-light-scattering diffusion coefficients were used to determine the effect of salt concentration on micelle mobility and size, salt-induced micelle diffusiophoresis and salt osmotic diffusion induced by micelle concentration gradients. In both salt cases, micelle diffusiophoresis was found to occur from high to low salt concentration (positive diffusiophoresis). Interestingly, diffusiophoresis becomes the dominant mechanism responsible for micelle transport near surfactant cloud point. This is related to an increase in both micelle size and osmotic compressibility with salt concentration. A preferential-hydration model was employed to theoretically describe the effect of salt salting-out on micelle diffusiophoresis and salt osmotic diffusion. Although micelle diffusiophoresis can be attributed to preferential hydration of PEG surface groups, salting-out salts also promote an increase in the size of micellar aggregates. This complicates diffusiophoresis description because it is not clear how surfactant aggregation contributes to micelle diffusiophoresis. We therefore developed a two-state aggregation model describing the observed salt concentration effect on the size of tyloxapol micelles and theoretically evaluated the contribution to diffusiophoresis. Our analysis shows that aggregation promotes micelle diffusiophoresis from low to high salt concentration (negative diffusiophoresis). However, we also find that this mechanism marginally contributes to overall diffusiophoresis, indicating that preferential hydration is the main mechanism causing micelle diffusiophoresis. We believe that concentration gradients of salting-out agents such as MgSO_4 and Na_2SO_4 may be employed for achieving migration of PEG-based colloidal particles such as those utilized as drug carriers and extracting agents with applications in the fields of microfluidics, enhanced-oil recovery, soil remediation, and controlled release technologies.